UNIVERSIDADE D
COIMBRA

Margarida Nunes Simões

MONTE CARLO SIMULATION OF AN IN-BEAM TOF-PET SYSTEM FOR RANGE MONITORING IN PROTON THERAPY

Dissertation for the degree of Master in Medical Physics supervised by Professor Doctor Paulo Alexandre Vieira Crespo and Professor Doctor Andrey Morozov and presented to the Department of Physics of the Faculty of Sciences and Technology of the University of Coimbra.

September 2022

• U C •

FCTUC FACULDADE DE CIÊNCIAS
E TECNOLOGIA
UNIVERSIDADE DE COIMBRA

Margarida Nunes Simões

Monte Carlo simulation of an in-beam TOF-PET system for range monitoring in proton therapy

Dissertation submitted to the
University of Coimbra for the degree of
Master in Medical Physics

Supervisors:
Professor Doctor Paulo Alexandre Vieira Crespo
Professor Doctor Andrey Morozov

Coimbra, September 2022

This work was developed in collaboration with:

LIP - Laboratório de Instrumentação e Física Experimental de Partículas

Resumo

A prototerapia permite fornecer uma dose significativa e conformada aos tumores, possibilitando a minimização da dose nos tecidos saudáveis circundantes. No entanto, a prototerapia é extremamente sensível a incertezas relacionadas com o alcance dos protões, que podem resultar numa sobre-irradiação dos tecidos normais e numa sob-irradiação do tumor. A monitorização do alcance dos protões é, por isso, crucial para garantir que o tratamento é administrado de acordo com o planeado.

A tomografia por emissão de positrões (PET, do inglês *positron emission tomography*) pode ser empregue na monitorização do alcance de protões. A irradiação de um doente com um feixe de protões induz a produção de espécies emissoras de positrões. O decaimento destas espécies conduz à emissão de raios gama, emitidos em direções muito aproximadamente opostas, que podem ser detetados por detetores de PET e permitir a reconstrução da distribuição da atividade resultante no corpo.

Não existe uma relação linear entre a atividade medida com a PET e a dose depositada durante a irradiação. Atualmente, a monitorização do alcance de protões através da PET é realizada comparando as distribuições da atividade medidas com distribuições de atividade previstas por simulações de Monte Carlo (MC). Qualquer desvio observado entre estas distribuições permite ajustar o plano de tratamento, uma vez que este não está a ser administrado de acordo com o planeado. Adicionalmente, a PET permite a comparação da distribuição da atividade medida numa determinada fração com distribuições medidas em frações anteriores, de forma a detetar desvios indesejados no tratamento.

O consórcio da TOF-PET para Prototerapia (TPPT, do inglês *TOF-PET for Proton Therapy*), uma associação entre diversas instituições de Portugal e dos Estados Unidos da América, encontra-se atualmente a desenvolver uma PET com informação do tempo de voo (TOF, do inglês *time-of-flight*) para monitorização do alcance de protões durante o tratamento de prototerapia em cancros da cabeça e do pescoço. A estrutura para simulações de MC da operação do protótipo TOF-

PET projetado foi desenvolvida em Geant4 por um grupo do Laboratório de Instrumentação e Física Experimental de Partículas (LIP). O trabalho desenvolvido no âmbito deste projeto de Mestrado desenrolou-se nas três contribuições abaixo apresentadas.

Primeiramente, os materiais do detetor da PET foram definidos no Geant4 e a sua geometria foi definida com os sólidos do Geant4 (abordagem G4VSolid). O detetor desenvolvido nesta abordagem foi posteriormente comparado em termos da sua eficácia de deteção com o detetor desenvolvido por um grupo distinto, numa abordagem obtida diretamente da geometria CAD (do inglês *Computer-Aided Design*) do protótipo (abordagem GDML, do inglês *Geometry Description Markup Language*). Para além disso, o efeito dos diferentes componentes do detetor definido na abordagem G4VSolid na eficácia de deteção foi analisado.

De seguida, os cortes de produção da simulação foram otimizados, de forma a minimizar o tempo da simulação e maximizar a sua exatidão.

Por fim, tendo em conta que a simulação desenvolvida pelo consórcio é um código aberto, informação acerca da produção de espécies emissoras de positrões resultantes da irradiação com protões (secção eficaz em função da energia dos protões) foi extraída de uma investigação publicada pelo *Heidelberg Ion-Beam Therapy Center* (HIT), na Alemanha, e do repositório de *Experimental Nuclear Reaction Data* (EXFOR). As distribuições de atividade resultantes dos dados extraídos e dos dados fornecidos confidencialmente pelo grupo do HIT foram comparados, de forma a validar os dados extraídos.

Os resultados obtidos demonstram que: (1) o efeito dos componentes do detetor na eficácia de deteção é mínimo, independentemente da abordagem adotada; o único efeito perceptível surge da face do invólucro que reveste o detetor voltada para o doente, que causa uma diminuição de aproximadamente 3% no número total de coincidências detetadas; (2) os cortes de produção ótimos foram alterados para 0,1 mm para todas as partículas secundárias; (3) as diferenças entre as distribuições de atividade resultantes dos dados das secções eficazes extraídos e dos dados providenciados confidencialmente pelo grupo do HIT foram insignificantes, validando, assim, os dados extraídos.

Palavras-chave: Prototerapia, monitorização do alcance de protões, tomografia por emissão de positrões, tempo de voo, simulação de Monte Carlo.

Abstract

Proton therapy allows to deliver a significant conformal dose to tumors while minimizing the dose in the surrounding healthy tissues. However, proton therapy is extremely sensitive to uncertainties related to the proton range, that can result in the over-irradiation of normal tissues and under-irradiation of the tumor. Proton range verification is, therefore, crucial to ensure the treatment is delivered as planned.

Positron emission tomography (PET) can be used for proton range verification. The irradiation of a patient with a proton beam induces the production of positron-emitting species. The decay of these species leads to the emission of approximately back-to-back gamma rays that can be detected by PET detectors, and allow the reconstruction of the distribution of the resulting activity in the body.

There is no straightforward relation between the activity measured with PET and the dose delivered during irradiation. Currently, proton range verification by means of PET is done by comparing the measured activity with activity distributions predicted by Monte Carlo (MC) simulations. Any mismatch between these distributions provides feedback to adjust the treatment planning, as the treatment is not being delivered as planned. Additionally, PET allows the comparison of the measured activity distribution from one delivered fraction with distributions from previous fractions, in order to detect whether unwanted deviations in the treatment are occurring.

The TOF-PET for Proton Therapy (TPPT) consortium, an association between several Portuguese and American institutions, is developing a PET with time-of-flight (TOF) information for range verification during the delivery of proton therapy to head and neck tumors. A framework for MC simulations of the operation of the designed TOF-PET prototype was developed in Geant4 by a group from the Laboratory of Instrumentation and Experimental Particles Physics (LIP). The work carried out under this Master's project was developed along the following three contributions.

Firstly, the PET detector materials were defined in Geant4 and its geometry was defined with Geant4's solids (G4VSolid approach). The detector defined in this approach was then compared in terms of its detection efficiency with the detector defined by another group in an approach directly obtained from the prototype's Computer-Aided Design (CAD) geometry (GDML, Geometry Description Markup Language, approach). Furthermore, the effect of the detector components defined in the G4VSolid approach on the detection efficiency was analyzed.

Secondly, the simulation production cuts were optimized to minimize the simulation run time while maximizing its accuracy.

Thirdly, given that the simulation developed for the TPPT consortium is an open-source code, proton-induced positron-emitting species production information (cross-sections versus proton energy) was extracted from a published work by the Heidelberg Ion-Beam Therapy Center (HIT), in Germany, and from the EXFOR (Experimental Nuclear Reaction Data) library. The activity distributions resulting from the extracted data and from the data provided privately by the HIT group were compared for validation.

The achieved results demonstrate that: (1) the effect of the detector components on the detection efficiency is small, no matter the approach; the only noticeable difference arises from the element of the detector enclosure facing the patient, that causes a decrease of approximately 3% in the total number of detected coincidences; (2) the optimal production cuts were set to 0.1 mm for all secondary particles; (3) the differences between the activity profiles resulting from the extracted cross-sectional information and from the data provided privately by the HIT group were negligible, hence validating the extracted data set.

Keywords: Proton therapy, proton range monitoring, positron emission tomography, time of flight, Monte Carlo simulation.

List of Abbreviations

EBRT	external-beam radiation therapy
SOBP	spread-out Bragg peak
PET	positron emission tomography
MC	Monte Carlo
TOF	time-of-flight
TPPT	TOF-PET for Proton Therapy
PTCOG	Particle Therapy Co-Operative Group
EC	electron capture
LOR	line of response
FOV	field of view
FWHM	full width at half maximum
SiPMs	silicon photomultipliers
TOF-PET	time of flight PET
CTR	coincidence time resolution
CT	computed tomography
HUs	Hounsfield Units
PG	prompt gamma
PMTs	photomultiplier tubes
PMMA	polymethyl methacrylate
DICOM	Digital Imaging and Communications in Medicine

ABS	acrylonitrile butadiene styrene
PCBs	printed circuit boards
GDML	Geometry Description Markup Language
CAD	Computer-Aided Design
GUI	Graphical User Interface
HIT	Heidelberg Ion-Beam Therapy Center
EXFOR	Experimental Nuclear Reaction Data
PWB	printed wire board

List of Figures

List of Tables

Contents

1

Introduction

1.1 Overview and motivation

Malignant tumors – also referred to as cancer – are the result of abnormal cell proliferation and, contrary to benign tumors, can spread to nearby tissues and even reach distant tissues through the circulatory or lymphatic systems, named as the ability to metastasize. Given that any cell of the body can start this abnormal proliferation, there are more than a hundred types of cancer and its behavior and response to therapy differs accordingly to the cells of origin [1].

Several factors can increase the probability of developing cancer. One of those factors is unmodifiable and consists in mutations caused by random errors in DNA replication. But other risk factors, the major contributors to develop the disease, are modifiable and their modification plays an important role in cancer prevention. External factors, like the exposition to radiation, chemical carcinogens, viruses and xenobiotics, and lifestyle factors (smoking, use of hormonal therapies, nutrient imbalance and lack of physical activity) are risk factors that can be modified. Other factors related to each individual, such as the metabolism, inflammation and hormone levels, can be partially modified [2].

The growth and aging of population, along with an increase of the main risk factors prevalence – highly correlated with the socioeconomic development of countries – is increasing the cancer incidence worldwide, turning it into a leading cause of mortality. It is estimated that there were approximately 19 million new cases of cancer and nearly 10 million deaths from cancer in 2020 worldwide [3].

Cancer treatments are based on several strategies which effect allows to obtain different rates of control of the disease. The most common strategies to treat cancer are systemic therapies (such as chemotherapy and immunotherapy), surgery and radiation therapy [4].

Radiation therapy, or radiotherapy, is used in the management of approximately 50% of cancer cases, either prescribed alone or together with chemotherapy or surgery, and it can be used as a radical (for curative purposes) or palliative (for symptom control) treatment [5]. It involves the use of high-energy particles or electromagnetic waves and aims to deliver radiation to tumors with the purpose of killing or damaging the cancer cells [6].

Ionizing radiation can damage cells both by direct or indirect action: in case of direct action, radiation interacts directly with the cell DNA or with regulatory proteins; in case of indirect action, there is an interaction with other cellular molecules and atoms (mainly water, the major cellular component) that results in the production of free radicals – highly reactive molecules that have an unpaired valence electron – that react with DNA, proteins and lipids. The damages provoked by direct and indirect actions are accumulated until the repair mechanisms are lost and either the cell becomes tumorigenic, i.e., unable to regulate its proliferation, or cell death occurs. Fractionated radiotherapy is based on the ability of the cells to repair its DNA when submitted to sublethal damages by radiation and on the fact that healthy cells present a higher repair capacity than tumor cells [7, 8].

The dose that can be directed to a tumor in radiotherapy is limited by the sensitivity of the surrounding normal tissues. Over the last decades, the improvements in the field have allowed to optimize the precision of the dose deposition in cancer cells while minimizing the unwanted dose on normal tissues [9].

The therapeutical use of radiation can involve the delivery of radiation from outside the patient's body – external-beam radiation therapy (EBRT) –, the implant of radioactive sources in the body – brachytherapy –, or the systemic administration of radiopharmaceuticals [10]. EBRT is the most common radiotherapy technique, and it implies the delivery of electromagnetic radiation (e.g., X-ray or gamma ray photons) or particles (e.g., electrons, protons, or other heavier particles such as carbon ions) to the patient [11].

Currently, most EBRT is based on X-ray beams of energies of about 4 to 18 megavolt and, although proton therapy is a very precise EBRT modality [12], only a small percentage of patients is yet treated with it, when compared to photon therapy. This fact is mainly due to the high costs associated with establishing and operating a proton therapy center; nevertheless, the percentage of patients submitted to proton therapy tends to increase as new proton therapy facilities are being established worldwide: by 2022, there are 103 proton therapy facilities in clinical operation, and 30 under construction, according to the Particle Therapy

Co-Operative Group (PTCOG) [13, 14].

Proton therapy is considered advantageous when compared to photon therapy due to how protons interact with tissues and deposit the radiation dose (depth-dose distribution), which allows a higher escalation of the dose directed at a tumor without compromising the normal tissues around it [13].

On one hand, X-ray beams, used in conventional photon therapy and in more modern techniques, such as intensity modulated radiation therapy (IMRT) or intensity modulated arc therapy (VMAT), present a maximum dose deposition at the entrance of the body, in the subcutaneous tissues, that gradually decreases as it crosses through it, and until it exits the body [15].

On the other hand, protons present a lower entrance dose and no exit dose beyond the tumor (the beam stops inside the body), thus affecting less the normal tissues around it, and it occurs an abrupt loss of energy at the maximum penetration depth, called the Bragg peak [15].

A monoenergetic proton beam is not adequate to treat cancer due to the narrowness of the Bragg peak; instead, a spread-out Bragg peak (SOBP), which is obtained by the superimposition of proton beams of closely spaced energies [15], is used to deliver a uniform dose within the target volume region [16].

Figure 1.1 presents the typical depth-dose distributions for a single Bragg peak, a SOBP, and an X-Ray beam of 10 MV.

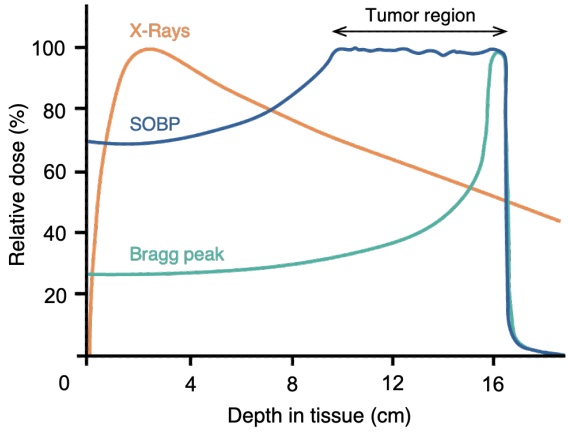

Figure 1.1: Typical depth-dose curves distributions for a single Bragg peak, for a spread-out Bragg peak, and for a 10 MV X-ray beam, used in conventional radiotherapy. Adapted from [15].

Because of the depth-dose distribution of protons, proton therapy is advantageous for the treatment of tumors with irregular shapes and/or located around critical tissues, and for pediatric patients, due to the lower integral dose, i.e., the total

energy deposited in the patient's body. However, proton therapy is more sensitive to uncertainties related to the treatment planning and delivery. In particular, because of the Bragg peak, uncertainties related to the proton range are critical, since it can result in normal tissues receiving the highest dose deposition (over-irradiation) and the tumors not receiving the planned dose (under-irradiation). Due to these uncertainties, proton therapy verification is crucial to ensure treatment planning and delivery systems are performing as expected [12, 17].

Positron emission tomography (PET) was proposed back in the 1970s for proton range verification. The irradiation of patients with proton beams induces the production of positron-emitting species (as carbon-11, ^{11}C, and oxygen-15, ^{15}O) that undergo β^+ decay. Back-to-back gamma rays (γ-rays) - that result from the annihilation of the positrons emitted as a product of the decay of those species with electrons of the tissue - can be detected by PET detectors. This detection allows the reconstruction of a three dimensional distribution of the positron emitters in the body [18].

Despite the evidence that PET can successfully be used for proton therapy treatment verification, it is not widely used in proton therapy sites yet. One of the reasons is the complexity involved in establishing a relation between the measured activity and the delivered dose: at the moment, proton therapy treatment verification by means of PET is performed by comparing the activity measured with PET to activity distributions predicted by Monte Carlo (MC) simulations. Another reason is the integration of an in-beam PET scanner at a proton therapy site, which faces certain geometrical constraints. This limitation arises from the fact that the optimal usage of PET for proton therapy verification implies the acquisition of ^{15}O activity *in situ*, due to its high relative abundance in biological tissues, demanding scans compatible with its relatively short half-life ($\approx$ 2 minutes) and, consequently, less prone to the biological distortion of the induced activity due to physiologic processes, such as washout mechanisms [19].

A viable solution to surpass this limitation consists in using a partial ring tomograph with an opening angle compatible with the treatment beam and with the patient positioning. This solution presents a lower detection efficiency (due to the solid angle) and originates the presence of artifacts in reconstruction. However, by including information of the time-of-flight (TOF) in the reconstruction, it is possible to significantly reduce the image artifacts, thus increasing the quality of the PET images acquired [19].

Nevertheless, offline PET, performed after the proton therapy treatment and

outside the treatment site (with a 5 to 10 minutes delay), has already been implemented for proton therapy range verification, using commercial full-ring PET systems. This verification method has, however, limited clinical applicability (due to the biological washout processes) and a high impact on the patient workflow [19].

1.2 Objectives

The TOF-PET for Proton Therapy (TPPT) consortium, an association between PETsys Electronics S.A. (Portugal), LIP – Laboratory of Instrumentation and Experimental Particles Physics (Portugal), ICNAS – Institute of Nuclear Sciences Applied to Health (Portugal), C2TN – Center for Nuclear Sciences and Technologies (Portugal), University of Texas at Austin (USA), and University of Texas MD Anderson Proton Therapy Center (USA), designed a PET scanner for range verification during the delivery of proton therapy to head and neck tumors.

The goal of the TPPT consortium is to develop a prototype of a positron emission tomography with time of-flight information (TOF-PET) for proton therapy range verification to be applied for small animal studies, with the purpose of later being reproduced in clinical sites.

The goal of LIP's group is to develop a framework for Monte Carlo (MC) simulations of the operation of the TOF-PET prototype designed by the TPPT consortium, to be used for image reconstruction and for proton range verification purposes. The software chosen to develop said simulation is Geant4, a toolkit that simulates the passage of particles through matter [20]. Based on the production of positron-emitting species during proton therapy irradiation, the aim of the MC simulations is to predict the distribution of the positron annihilation events that should be observed; any mismatch with the experimental observation provides feedback to adjust the treatment planning, as the treatment is not being delivered as planned [21].

The objectives of this Master's dissertation work consist in contributing to the framework developed by LIP's group, namely to complete the PET system detector geometry, and to optimize the simulation in terms of accuracy and simulation run time.

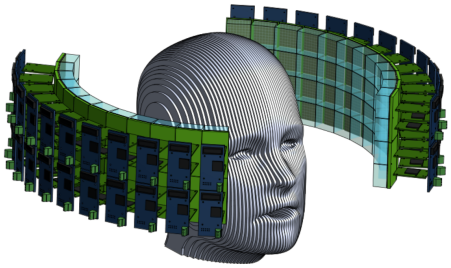

Figure 1.2: TOF-PET prototype designed and developed by the TPPT consortium.

1.3 Contributions for the project

The work developed during this Master's dissertation project consisted in the:

- Development of the PET prototype geometry (excluding the scintillators) and definition of its materials in Geant4;
- Comparison of the PET system response in terms of detected hits, number of coincidences, energy deposition, and simulation run time for the geometry defined by two approaches (Geant4 solids and GDML);
- Search for the cross-sections data for long-lived positron-emitting species (carbon -11, ^{11}C, oxygen-15, ^{15}O, nitrogen-13, ^{13}N, potassium-38, ^{38}K, and phosphorus -30, ^{30}P), and its validation for the simulation;
- Optimization of the production cuts parameters to minimize the simulation run time.

1.4 Dissertation outline

This document is structured into 6 other chapters. Chapter 2, Theoretical Background, provides the theoretical background needed to understand the physics concepts on which the developed work is based on. Chapter 3, Range Verification in Proton Therapy, summarizes the current main methods for range monitoring in proton therapy, focusing mainly on positron emission tomography. In chapter 4, Simulation Framework, the approach selected by the TPPT consortium and the simulation framework overview are presented. In chapter 5, Development of the PET System Simulation Model, and chapter 6, Simulation Customization, the work developed for this dissertation and the results obtained are presented and discussed. Finally, chapter 6, Conclusion, highlights the main conclusions and presents an outlook for future work.

2

Theoretical Background

This chapter presents a summary of the main interactions of charged particles and photons with matter, as well as it provides a brief introduction on the radioactive decay of radionuclides.

2.1 Interaction of charged particles with matter

Charged particles can be divided into electrons, positrons, and heavier particles, such as protons and heavier nuclei [22].

When charged particles pass through matter, mainly three processes of interaction can occur: inelastic collisions with the atomic electrons, elastic scattering from nuclei, and nuclear reactions (less often). The main results of these processes are, respectively, the loss of energy by the charged particle, a deflection from its incident direction, and the emission of electrons, neutrons, gamma rays, and other small nuclei from the target atoms and nuclei [22]. Nuclear reactions are the basis of non-invasive approaches to measure the proton therapy beam range [23].

2.1.1 Energy loss rate of heavy charged particles

The inelastic collisions are the main responsible for the energy loss that occurs when heavy particles interact with matter: the particle transfers energy to the atom, causing its excitation or ionization. Sometimes, the amount of energy transferred is not only enough to ionize the atom, but also to make the removed electron cause substantial secondary ionization itself (these electrons are referred to as δ-rays) [22].

Elastic scattering from nuclei, although not as frequent as inelastic collisions, can also occur. Given that the mass of the nuclei are often larger than the mass of the incident particle, a small amount of energy is transferred in these collisions [22].

In each inelastic collision, the amount of energy transferred usually consists in

a very small fraction of the charged particle's total kinetic energy; nonetheless, in dense materials, the number of collisions per unit path is large enough so that a considerable cumulative energy loss is observed, even in thin layers of material [22]. As a consequence of the number of inelastic collisions per pathlength being usually large, the energy loss rate can be considered as the average energy loss per unit path length – a quantity defined as the stopping power, or dE/dx (the minus sign for the expression of the stopping power indicates that the energy is lost by the particle) [22, 24]:

$$S = -\frac{dE}{dx} \qquad [\mathrm{MeV\,cm^{-1}}] \quad (2.1)$$

A realistic formula for energy loss calculations was developed by Bethe, Bloch and other authors, and it is known as the Bethe-Bloch formula [22]:

$$-\frac{dE}{dx} = 2\pi N_A r_e^2 m_e c^2 \rho \frac{Z}{A}\frac{z^2}{\beta^2}\left[\ln\left(\frac{2m_e\gamma^2 v^2 W_{max}}{I^2}\right) - 2\beta^2 - \delta - 2\frac{C}{Z}\right] \quad (2.2)$$

where N_A is the Avogadro's number, r_e is the classical electron radius, m_e is the electron mass, c is the speed of light, ρ, Z and A are, respectively, the density, the atomic number, and the atomic weight of the absorbing material, z is the charge of the incident particle, β is v/c of the incident particle, γ is $1/\sqrt{1-\beta^2}$, v is the velocity of the incident particle, W_{max} is the maximum energy transfer in a single collision produced by a head-on collision ($W_{max} \approx 2m_e c^2 \eta^2$ for protons, with $\eta = \beta\gamma$), I is the mean excitation potential, given by the average orbital frequency times the Planck's constant ($h\overline{v}$), δ is the density correction and C is the shell correction [22, 25].

The parameters δ and C were introduced as corrections to the formula, important at high and low energies, respectively. The density correction is needed to consider the polarization of the atoms along the particle's path due to its electric field, since electrons far from the particle will be shielded from the full electric field intensity and collisions with these outer electrons will contribute less to the total energy loss than initially predicted by the formula. This effect depends on the density of the material, as the induced polarization will be greater in condensed materials. The shell correction is relevant when the velocity of the incident particle is close or smaller than the orbital velocity of the bound electrons, so that the electron cannot be assumed to be stationary with respect to the incident particle, which is an assumption of the formula [22].

The stopping power can also be expressed in units of mass thickness [22]:

$$-\frac{1}{\rho}\frac{dE}{dx} = 2\pi N_A r_e^2 m_e c^2 \frac{Z}{A}\frac{z^2}{\beta^2}\left[\ln\left(\frac{2m_e\gamma^2 v^2 W_{max}}{I^2}\right) - 2\beta^2 - \delta - 2\frac{C}{Z}\right] \tag{2.3}$$

The energy loss suffered by the incident particle is directly proportional to the square of its charge (for protons, z is equal to 1), to the inverse square of its velocity, and it does not depend on its mass. Additionally, it is also directly proportional to the density of the absorbing material [23].

The ratio Z/A varies little for elements with not too different Z: specifically, Z/A varies only about 16%, from 0.5 for biologic elements, as oxygen and carbon, to 0.42 for elements of higher atomic number, such as lead, a beamline component; an exception is hydrogen (the ratio Z/A is equal to 1), however, its concentration in the human body is low (just about 10%) and uniform throughout the body. The dependence on I, that varies with Z, is also diminished, since it appears in a logarithm in the expression of the stopping power [22, 23].

Considering these relations, the energy loss suffered by protons in the human body depends mostly on their velocity, that can make the stopping power vary about a factor of 60 for protons of energies between 1 to 250 MeV in water, and on the material density, which can vary almost three orders of magnitude, from the air in the lung to cortical bone [23].

2.1.1.1 The Bragg curve

The rate of energy loss of a heavy particle changes as its kinetic energy changes and the particle slows down in matter: more energy is deposited per unit length at the end of the path, rather than at the beginning, i.e., the number of ionizations per penetration depth rises to a maximum when the particle has lost almost all its energy [22, 24]. This change of the stopping power as a function of the penetration depth in matter is known as the Bragg curve (figure 2.1) [22].

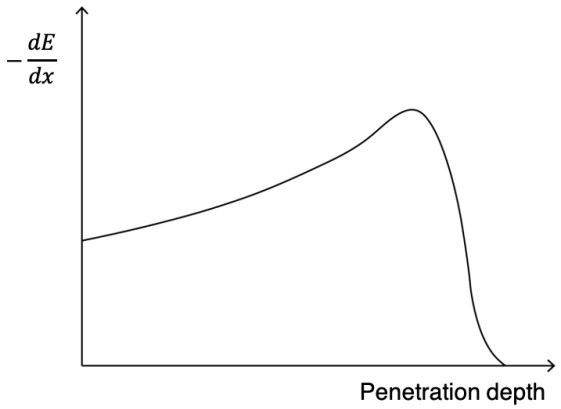

Figure 2.1: Typical Bragg curve. More energy is deposited towards the end of the particle's path (which means the particle is more ionizing at the end of its path). At the very end, though, it begins to pick up electrons, and the stopping power drops abruptly. Adapted from [22].

2.1.1.2 Range of heavy charged particles

The range of a charged particle indicates how far the particle can penetrate in matter before losing all its energy, and it depends on the type of material, the particle type (mass and charge) and the particle energy. The range is experimentally determined by making a beam of particles pass through different thicknesses of a material and by measuring the proportion of transmitted to incident particles, being possible to obtain a curve, named as a range number-distance curve, of said ratio as a function of the thickness of the material (figure 2.2) [22].

However, identical particles with exactly the same energy usually do not suffer the exact amount of collisions and, consequently, the same energy loss. The distribution of the ranges of identical particles is a Gaussian centered on a mean range, that corresponds to the thickness of the absorber material that reduces the particle count to half of its initial value. Such phenomenon is known as range straggling. The material thickness at which all particles are considered to be absorbed is found by taking the tangent to the curve at the midpoint and extrapolating to the zero-level, called the extrapolated or practical range [22].

The effect of multiple Coulomb scattering (explained with further detail in section 2.1.3) – that makes the particle follow a zigzag path through the absorber – is small for heavy charged particles, which makes the total path length essentially a straight-line range, that can be given by the mean range of a particle of a certain kinetic energy (T_0), by integrating the stopping power formula [22]:

$$R = \int_0^{T_0} \left(\frac{dE}{dx}\right)^{-1} dE \tag{2.4}$$

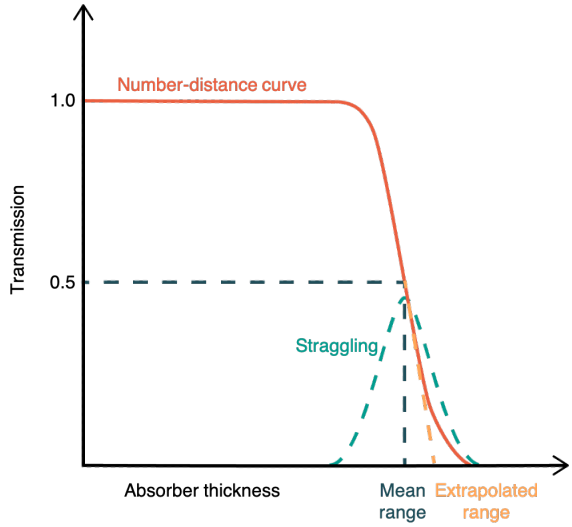

Figure 2.2: Typical range number-distance curve. Adapted from [22].

2.1.1.3 Energy and range straggling

As previously discussed, the energy loss suffered by charged particles is considered as the mean energy loss. Nevertheless, the amount of energy lost by each individual particle is not equal to this exact mean value, due to statistical fluctuations in the number of collisions and in the amount of energy transferred in each collision [22].

Energy and range straggling are actually the same problem viewed from a different perspective: instead of observing the fluctuations in energy loss for a fixed thickness of absorber, the fluctuations in thickness of absorber for a fixed loss in energy are observed [22].

That way, the same stochastic factors that lead to energy straggling at a certain penetration length, will also result in slightly different total path lengths for each particle. For heavy charged particles, such as protons, the straggling amounts to a few percent of the mean range and the degree of straggling is evidenced by the sharpness of the cut-off at the end of the Bragg curve [25].

2.1.1.4 Nuclear reactions

Besides the mechanisms described above, if charged particles have enough energy to penetrate the Coulomb barrier of the nucleus, they can also interact with the atomic nucleus via inelastic nuclear reactions. In these reactions, the nuclei undergo a transformation that may imply the absorption of the particle by the nucleus and the consequent emission of electrons, neutrons, gamma rays, or other nuclei from

the target, such as radionuclides [23, 26].

2.1.2 Energy loss of electrons and positrons

When passing through matter, electrons and positrons suffer, similarly to heavy charged particles, collisional energy losses. Additionally, because of their small mass, there is also emission of electromagnetic radiation due to scattering in the electric field of nucleus (*bremsstrahlung*). For energies smaller than a few MeV, the radiation losses are still a small factor, but as energy increases, the energy lost by radiation is comparable or even greater than the collision losses and, for energies above this critical energy, radiation losses completely dominate. The total energy loss of electrons and positrons is given by [22]:

$$\left(\frac{dE}{dx}\right)_{tot} = \left(\frac{dE}{dx}\right)_{coll} + \left(\frac{dE}{dx}\right)_{rad} \tag{2.5}$$

2.1.3 Multiple Coulomb scattering

As already referred to, besides the inelastic collisions with atomic electrons, charged particles also suffer elastic Coulomb scatterings from nuclei, even if with a smaller probability. The nuclei may be massive when compared to the incident particle and, therefore, the energy transferred to the nucleus is negligible. The incident particle follows a random zigzag path through the material and the cumulative result of the small angle scatterings is a net deflection from the original direction [22].

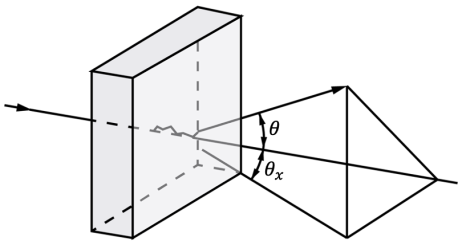

Figure 2.3: Multiple Coulomb scattering of a charged particle. Adapted from [22].

2.2 Interaction of photons with matter

Photons with energies above 10 eV are considered secondary ionizing radiation, since the interaction of photons with matter does not cause ionization directly, but

some of the interactions can eject orbital electrons from the atom or create electron-positron pairs that cause, in turn, ionization, making the detection of such high energy photons possible [27].

There are four main interactions between photons and matter [27]:

1. Photoelectric effect;
2. Compton scattering;
3. Pair production;
4. Rayleigh scattering.

2.2.1 Photoelectric effect

The photoelectric effect implies the absorption of a photon by an atom and the subsequent ejection of the electron from the atom (called a photoelectron) [27]. The kinetic energy of the ejected electron is given by the difference between the energy of the incident photon, hv, and the binding energy of the shell from which the photoelectron was ejected, B_e [25]:

$$E_{e^-} = hv - B_e \tag{2.6}$$

The photoelectron carries most of the incident photon energy, for gamma ray energies above a few hundred keV [25].

This interaction creates an ionized atom, leaving a vacancy in one of its bound shells, which is quickly filled by capture of a free electron of the medium or by rearrangement of the electrons from other shells of the atom. Because of this, one or several characteristic X-rays can also be generated, or, more rarely, the emission of an Auger electron can occur (when the energy released is transferred to another orbital electron), rather than being the characteristic X-ray to carry the atomic excitation energy away [25, 27].

2.2.2 Compton scattering

In Compton scattering, because the energy of the incident photon is considerably higher than the binding energy of the electron to the atom, the electron can be considered as free [27].

The incident photon is deflected through a scattering angle θ, and part of its

energy is transferred to the electron, which is then designated as a recoil electron. The energy of the scattered photon, hv', is given by [25, 27]:

$$hv' = \frac{hv}{1 + \gamma(1 - cos\theta)} \tag{2.7}$$

with $\gamma = hv/m_e c^2$ [22] and hv being the energy of the incident photon.

The energy of the recoil electron is given by [27]:

$$E_{re} = hv - hv' \tag{2.8}$$

2.2.3 Pair production

Pair production consists in the transformation of a photon into a positron-electron pair. It occurs when a photon interacts with the electric field of a charged particle; therefore, for pair production to occur, a presence of a third body (often a nucleus, but occasionally an electron) is required, to conserve momentum. Besides that, the photon must have an energy of at least 1.022 MeV to be able to create the electron-positron pair, i.e., twice the rest-mass of both the positron and electron (0.511 MeV) [22, 27].

The difference between the energy of the incident photon, E_0, and the 1.022 MeV necessary to create the electron pair is transferred as kinetic energy to the positron, E_{e^+}, and the electron, E_{e^-} [27].

$$E_{e^+} + E_{e^-} = E_0 - 1.022 \tag{2.9}$$

The positron produced will eventually annihilate after slowing down in the medium and, consequently, two annihilation photons are usually produced as secondary products of this type of interaction [25].

2.2.4 Rayleigh scattering

Rayleigh (or coherent) scattering consists in the scattering of photons by bound electrons; the photon is deflected without barely suffering a loss of energy because of the great mass of the atom. Despite remaining with essentially the same energy, the photon is scattered, but the average scattering angle decreases with increasing

energy. For this reasons, this scattering process is only relevant at low energies ($\ll$ 50 keV) [25, 27].

2.2.5 Interaction probability

Figure 2.4 depicts the most probable photon interaction considering the photon energy, E, and the atomic number of the absorber, Z. The photoelectric effect interaction probability decreases quickly with increasing photon energy and increases quickly with increasing absorber atomic number, thus dominates in heavy elements at low photon energies. The Compton scattering interaction probability decreases slowly with increasing photon energy and with increasing absorber atomic number, thus dominates for intermediate values of Z and E. The pair production interaction probability is zero for photons with energies less than 1.022 MeV, and then increases logarithmically with increasing photon energy and absorber atomic number, thus being the dominating process at higher photon energies in absorbers of high atomic number [27].

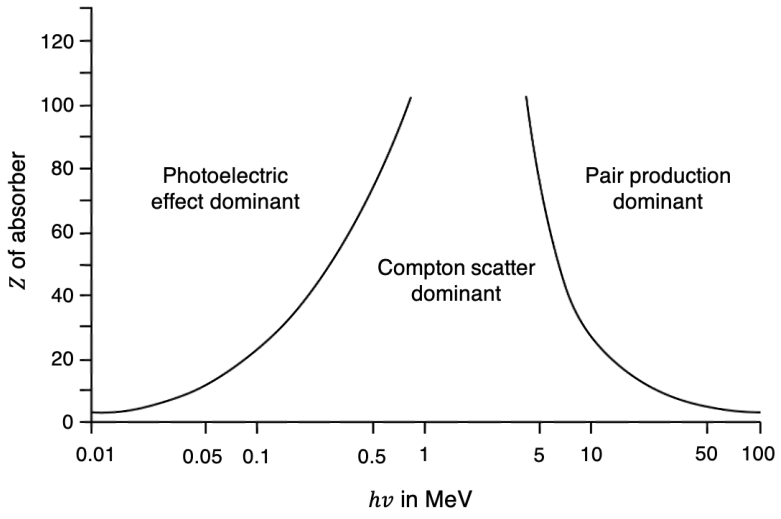

Figure 2.4: Dominating interaction versus photon energy for absorbers with different atomic numbers. The line at the left depicts the photon energy at which photoelectric absorption and Compton scattering are equally probable, and the line at the right depicts the photon energy at which Compton scattering and pair production are equally probable as a function of the absorber atomic number [25]. Adapted from [25].

Table 2.1 summarizes the products (secondary photons and electrons) of the main interactions of photons with matter [27].

Interaction	Secondary photon	Secondary electron
Photoelectric effect	Characteristic X-ray	Photoelectron
	-	Photoelectron, Auger electron
Compton scattering	Scattered photon	Recoil electron
Pair production	Annihilation photon	Electron-positron pair

Table 2.1: Summary of the main photon interactions with matter.

2.3 Radioactive decay

2.3.1 Decay of radionuclides

Nuclides are species of atoms characterized by the number of nucleons (protons and neutrons) and by the energy of the atomic nuclei. Unstable nuclides, called radionuclides, have an unstable combination of nucleons (neutron excess or deficiency) and, for that reason, have an excess of internal energy compared to stable combinations, and decay to more stable nuclei by a transformation process named radioactive decay (or radioactive disintegration) [28, 29].

Unstable nucleus (the parent) decays to a more stable product (the daughter) by emitting particles, photons, or both, and releasing energy during the transformation process. The radioactive decay can lead to the creation of a stable nuclide or of a radionuclide, that undergoes further radioactive decay [27].

The radioactive decay is a random process, which implies that it is not possible to determine which particular atom from a group of atoms will decay at a certain time, hence it only makes sense to consider the average number of unstable nuclides disintegrating during a period of time: the disintegration rate of a radionuclide, i.e., the number of disintegrations per unit time, $-dN/dt$, called the radioactivity or simply the activity of a radionuclide, A [30]:

$$A = -\frac{dN}{dt} \qquad \text{[Bq]} \quad (2.10)$$

The disintegration rate is, at any time, proportional to the total number of radioactive atoms present at that time [30]:

$$-\frac{dN}{dt} = \lambda N \qquad (2.11)$$

where N is the number of radioactive atoms, and λ is the decay constant, given by the probability of disintegration of the radioactive atom per unit time.

The solution of the differential equation in 2.11 represents the exponential decay of a radionuclide and is given by:

$$N_t = N_0 e^{-\lambda t} \tag{2.12}$$

where N_t and N_0 represent the number of atoms present at time t and time = 0, respectively [30].

Or, in terms of radioactivity:

$$A_t = A_0 e^{-\lambda t} \tag{2.13}$$

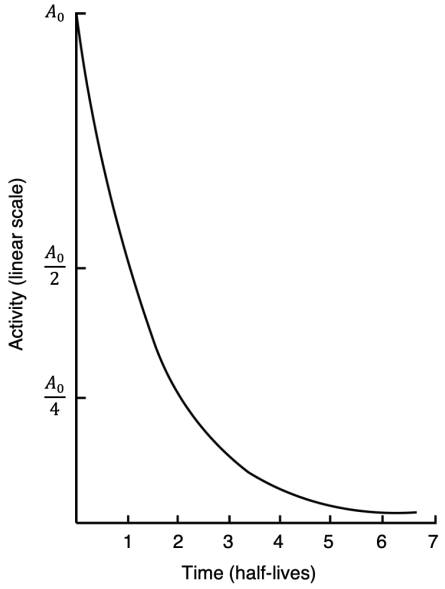

Figure 2.5: Plot of radioactivity versus time (in units of half-life). The graph depicts an exponential decay of radioactivity with time. Adapted from [30].

2.3.1.1 Half-life and mean lifetime

The half-life, $t_{\frac{1}{2}}$, unique for each radionuclide, is the time required to reduce its initial activity to one half, and is related to the decay constant by [30]:

$$\lambda = \frac{ln(2)}{t_{\frac{1}{2}}} \approx \frac{0.693}{t_{\frac{1}{2}}} \tag{2.14}$$

The radioactivity is, by the definition of half-life, reduced to $A_0/2^n$ in n half-lives of decay; therefore, the radioactivity at time t, A_t, can be calculated from the

initial radioactivity, A_0, by [30]:

$$A_t = \frac{A_0}{2^n} = \frac{A_0}{2^{t/t_{1/2}}} \tag{2.15}$$

where t is the decay time.

The mean lifetime, τ, is another quantity that characterizes a radionuclide, and is given by the time that it is required for the sample to decay to 1/e of its initial activity [22]. It is related to the decay constant and to the half-life by [30]:

$$\tau = \frac{1}{\lambda} = \frac{t_{\frac{1}{2}}}{\ln(2)} \approx 1.44 t_{\frac{1}{2}} \tag{2.16}$$

2.3.2 Types of radioactive decay

Most radionuclides decay by one or by a combination of the following processes: α decay, nuclear fission, β^- emission, β^+ (positron) emission, electron capture (EC), or isomeric transition [27, 28, 30].

Unstable heavy elements usually decay by α particle emission or by nuclear fission. In α decay, the nucleus ejects an α particle, ${}^4_2\mathrm{He}$. Nuclear fission consists in the spontaneous fragmentation of a very heavy nucleus into two lighter nuclei, with two or three fission neutrons being ejected [27].

In radioactive decay by β^- emission, a neutron is transformed into a proton and an electron. The energy released in this type of decay is shared as kinetic energy by the β^- particle and an antineutrino (that has no electrical charge and a very small mass, thus interacting only weakly with matter), and both are ejected from the nucleus: $n \rightarrow p^+ + e^- + \overline{\nu}$ [24, 27, 30].

In radioactive decay by β^+ emission, a proton is transformed into a neutron and a positron (β^+ particle). The positron and a neutrino are ejected from the nucleus: $p^+ \rightarrow n + e^+ + \nu$ [27].

In electron capture, an orbital electron is captured by the nucleus and combines with a proton to form a neutron: $p^+ + e^- \rightarrow n + \nu$ [27].

Sometimes, the nucleus produced in a radioactive decay can remain in an excited state for a certain amount of time (isomeric state), and when it decays by isomeric transition to the ground state, which can take from fractions of a second to many years, it occurs γ ray emission. A long-lived isomeric state is called a metastable

state [29].

Internal conversion occurs during γ ray emission, when the photon emitted from the nucleus interacts with an orbital electron, which is ejected (conversion electron) [27, 29]. The vacancy resulting from the ejection of the conversion electron is filled with electrons from outer shells, leading to the emission of characteristic X-rays. Moreover, those characteristic X-rays can, in turn, interact and eject other outer orbital electrons (the ejected electron is referred to as an Auger electron). The vacancy originated by the Auger electron is filled by electrons from outer shells, leading to further characteristic X-rays emission [29].

Radionuclides that present a proton deficiency usually decay by β^- emission, to transform a neutron into a proton; radionuclides that present a neutron deficiency usually decay by β^+ emission or EC, to transform a proton into a neutron; heavy nuclides usually decay by α emission or by nuclear fission, to reduce the mass number and acquire nuclear stability [27].

3

Range Verification in Proton Therapy

3.1 State of the art

As already mentioned, proton range uncertainties are a major concern due to the large gradient of dose delivered near the Bragg peak, especially when a critical structure (as the spinal cord) is located near the target volume [31].

Uncertainties in dose delivery in proton therapy arise from different sources, such as organ motion, errors in patient positioning or beam delivery, anatomic changes relatively to previous fractions in situations of fractionated dose delivery (as shrinkage of tumors and body weight change), and treatment planning errors [12, 31]. A computed tomography (CT) image of the patient is used to perform the treatment planning, and errors in this phase emerge from inaccuracies in the conversion of the Hounsfield Units (HUs) of the CT image to proton-stopping power maps that allow dose calculations, and from CT artifacts, CT noise and CT resolution [12, 32].

The reduction of proton range uncertainties potentially allows to improve the precision of proton therapy and to reduce the toxicity to healthy tissues, since these uncertainties require larger safety margins in the treatment planning that result in a less conformal dose distribution, and, consequently, limit the potential benefits of proton therapy over conventional therapies [32, 33].

Several methods have been investigated to monitor the particle range *in situ*, i.e., directly during dose delivery. There are, however, many constraints imposed by the clinical site that restrain the instrumentation design: it must not interfere with the proton beam nor with the patient, who is generally positioned on a robotic couch; its size and weight must be compatible with the treatment gantry; it must not extend

the period of time that patients are in the treatment room, mainly due to economic reasons, since proton therapy facilities are a considerable investment and several treatments are delivered per day; it must be compatible with the irradiation time – irradiation times are as short as possible to, among others, reduce the probability of positioning errors, and cannot be lengthened to facilitate the instrumentation performance [33].

Imaging methods are a promising approach for range monitoring in proton therapy, as they are already routinely used in photon therapy, where the beam completely crosses the patient's body, to imaging the photons that exit the body [18, 34]. In proton therapy, however, given that the proton beam stops inside the patient, imaging methods for range monitoring must be based on signals from secondary radiation produced by the interaction of the proton beam with tissues that escape the body and bear information about the proton beam range [33, 34].

The two main – and the most promising – methods to perform range verification *in vivo* are prompt gamma (PG) and positron emission tomography (PET) imaging, both based on the fact that when protons pass through tissues, some of the nuclear reactions result in the emission of gammas [26, 35].

Treatment monitoring is based, in case of PG, on the detection of prompt gammas resulting from the excitation of the target nuclei [25]. When a tissue is irradiated with a proton beam, some nuclei can be excited due to nuclear reactions with the incident protons and can emit characteristic photons – prompt gammas – when returning to the ground state. The energy of the emitted prompt gammas depends on the elemental nuclei excited. Prompt gammas are emitted almost immediately (within nanoseconds) after a collision between the proton and the nucleus occurs, and initial measurements of this emission have shown to correlate well with the depth-dose profile of proton beams [36].

There are two main prompt gamma imaging (PGI) systems that can be used for proton therapy range verification purposes [33]: a detection system that combines a collimator (a pin-hole, a knife-edge shaped slit, a single slit, or multiple collimator) with a gamma ray detector or array of detectors, and a collimator-less detection system based on Compton cameras [37].

The Knife-Edge Slit Camera, developed by IBA, a company that commercializes proton therapy equipment, is the only prompt gamma imaging system ever used for range monitoring in clinical environment. However, the integration of such an enormous and heavy collimator system in a proton therapy facility is an expensive

challenge [33].

As a consequence, several efforts have been made to develop a Compton imaging system for proton therapy range verification purposes. Nevertheless, the complexity from the technical point of view, the costs associated to the electronics needed, the huge size of the detector that needs to be manipulated during the treatment, and the small fraction between valid events and background compromise the applicability of Compton cameras for the proton therapy context [33].

Treatment monitoring based on PET imaging relies on the detection of back-to-back gammas resulting from the production of positron-emitting species. When a tissue is irradiated with a proton beam, a small fraction of protons produce positron-emitting species through nuclear reactions [26]. These positron emitters can be imaged with PET during (online) or after (if shortly after: in-room; if with a greater delay: offline) the proton therapy treatment, reflecting the resultant spatial β^+ activity distribution [38, 39].

3.2 Positron Emission Tomography

Positron emission tomography (PET) is an imaging technique with relevant oncological, neurological and cardiovascular applications. It is capable of providing physiological information regarding the function of tissues and organs through the administration of radioactive compounds, and can be used for detection, screening, classification, staging, prognosis, treatment planning, assessing response to therapy, and surveillance of diseases. Additionally, it is also used for preclinical studies, as in the investigation of small-animal models of disease [40].

The radioactive compounds used in PET, named radiopharmaceuticals or radiotracers, are composed by a radionuclide and a pharmaceutical. The pharmacologic effect is, however, negligible, since radiopharmaceuticals are injected in small quantities, only for tracing purposes. The pharmaceutical is chosen based on its preferential localization in a particular organ or its participation in a physiologic function, and it is labelled with a suitable radionuclide, i.e., that emits radiation that can be detected by a radiation detector after the administration of the radiopharmaceutical [30].

Specifically, PET allows to obtain images representative of the distribution of positron-emitting radioactive nuclides in patients. Therefore, it requires the use of β^+ emitting radionuclides, which is the case of fluorine-18 (^{18}F), nitrogen-13 (^{13}N), carbon-11 (^{11}C), oxygen-15 (^{15}O) and gallium-68 (^{68}Ga) [28, 30].

PET imaging can also be, as mentioned above, applied to range monitoring in proton therapy. In this application, no radioactive tracers are administered to patients; instead, it is based on the detection of positron emitters produced as a result of the irradiation of patients with a proton beam [41].

3.2.1 PET principles

As already referred to, nuclei that have a deficiency in neutrons (or an excess of protons) can decay by positron (β^+) emission [30]. The positrons are emitted with a range of energies that depend on the positron-emitting species; depending on its energy, a positron travels between a fraction of a millimetre to several millimetres from its point of production and, at the end of its path, interacts with a nearby electron of the tissue. The two particles annihilate and the mass of both the positron and electron is converted into energy in the form of two gamma rays of 511 keV each. Due to energy and momentum conservation, the two photons are emitted in opposite directions, at approximately 180^{o} to each other [29].

The annihilation photons are frequently not emitted at exactly 180^{o} apart. This is due to the fact that the positron and electron often possess a residual momentum before annihilation. Conservation of momentum results in a noncolinearity between the emitted photons. This noncolinearity is not drastic (it is of about $180^{\text{o}} \pm 0.5^{\text{o}}$), and its blurring effect is not clinically significant for the typical PET systems [28]. A small percentage of positron-electron annihilation (only about 2% of these interactions) can occur before the positron loses all of its kinetic energy, in a process referred to as in-flight annihilation. In this case, the two resulting gammas do not have identical energies and are emitted with different emission angles with respect to the incident positron [7, 42].

A PET scanner, composed by radiation detectors, is capable of detecting such photon pairs. When both gamma rays are detected by two detectors on the scanner within a short period of time of one another (usually, within 10 ns), it is assumed that the annihilation took place somewhere along a straight line that connects those two detection points, called the line of response (LOR). After a large number of annihilation photon pairs are detected, that information is used to compute the three-dimensional distribution of the radionuclide using a reconstruction algorithm, resulting in a set of tomographic emission images [28, 29].

3.2.1.1 Types of coincidence events

There are three types of coincidence events (figure 3.1):

1. True - when the annihilation point is situated along or closely to the LOR, which happens when there is a simultaneous interaction of the gamma rays resultant from the same annihilation with the detectors;

2. Scatter - when one or both photons from the same annihilation were scattered before both being detected;

3. Random (also known as accidental or chance coincidence) - when the photons detected were originated from different annihilations, but interact nearly simultaneously with the detectors [28, 29].

A scatter coincidence is, in reality, a true coincidence, given that the interactions with the two detectors result from the same annihilation, but the spatial information on the original annihilation location is lost, and a random coincidence mimics a true coincidence. Scattered and random events result, therefore, in misleading coincidences, since they are associated with LORs that do not cross the real annihilation positions. These coincidences can compose more than approximately 75% of the total number of coincidences recorded in clinical PET, degrading the image contrast and increasing the statistical noise. Therefore, minimising the number of these events is one priority in designing PET scanners [28, 29]. PET scanners are configured to accept only events which energy lies in an energy window around 511 keV (photopeak) - typically, 511±10% - to reduce the contribution from scatter and random coincidences [42].

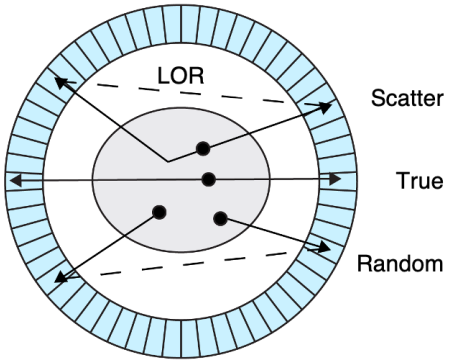

Figure 3.1: Types of coincidence events: true, scatter and random. The line-of-response (LOR) connects both detection points of a coincidence event pair. Adapted from [29].

3.2.1.2 Sensitivity

The sensitivity of a PET scanner is given by the fraction of the total number of pairs of annihilation photons that are collected and contribute to the formation of the obtained image, and it depends on the angle subtended by the scanner at the

center of the field of view (FOV), named the solid angle, Ω, and on the square of the efficiency of the individual detector, ε, since both photons must be detected to be considered a coincidence. The sensitivity is around 0.5% to 5% for modern cameras [29].

3.2.1.3 Spatial resolution

The spatial resolution consists in a metric that quantifies the ability of an imaging system to distinguish two individual objects closely separated in space [43]. In PET, the spatial resolution is measured by the image acquisition of a line source. A cross-sectional profile of the source image is obtained and the resolution is specified as the full width at half maximum (FWHM) of the source response [28, 44].

PET spatial resolution is influenced by the positron range, i.e., the distance traveled by the positron before annihilation, the acollinearity of the gamma pairs, and the PET detector width [28, 29, 45].

The spatial resolution is better at the center of the PET scanner and slightly decreases off-center, which is due to the fact that photons emitted from the center of the scanner reach the detectors "head-on", but photons emitted away from the center can reach the detectors from oblique angles, causing an uncertainty regarding the depth of interaction and, therefore, in the LOR (figure 3.2). This occurs due to the significant thickness of the detectors, and choosing thinner crystals would reduce this effect, but would also end up reducing the detection efficiency and, consequently, the number of detected coincidences [28].

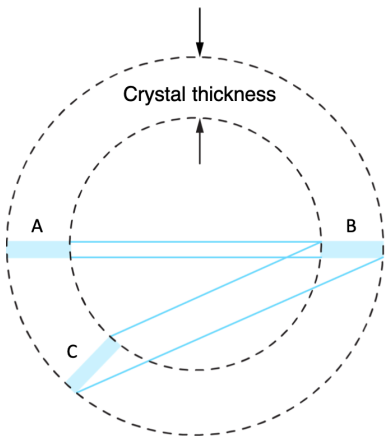

Figure 3.2: Cause of the reduced PET spatial resolution off-center. For a coincidence detected by detectors A and B, there is little uncertainty in the LOR; for a coincidence detected by detectors B and C, there is a greater uncertainty in the LOR. Adapted from [28].

Positron range distribution in tissue depends on the maximum positron energy

for the radionuclide, and on the tissue density [28, 29]. Radionuclides that emit lower energy positrons provide better resolution; activity in denser tissues also provide a higher resolution than in less dense tissue (as lung) [28].

Acollinearity of gamma pairs, as mentioned, consists in the emission of photons in not exactly opposite directions, which causes a small loss in the spatial resolution, that increases with the scanner's diameter [28].

3.2.2 PET detectors

The detectors used in commercial PET scanners consist of scintillation crystals coupled to photodetectors (e.g., photomultiplier tubes (PMTs) or silicon photomultipliers (SiPMs)) [28]. When hit by radiation, the atoms of a scintillator material are excited and the scintillator emits light that can be converted into electrical pulses by amplifying devices, usually PMTs, and, when analyzed by an electronics system, provide information about the incident radiation [22].

An adequate PET detector must have:

1. a high detection efficiency (ε) for 511 keV photons, i.e., a high probability that 511 keV photons will be absorbed by the detector, which can be obtained by a material with a high density (that favors the interaction of the photon in the crystal) and atomic number (that increases the number of photoelectric absorption occurrences with respect to Compton scattering) [29, 46];

2. a high spatial resolution, which requires a high light yield (number of optical photons produced by energy deposited) to locate the interaction position, since the scintillation light is often divided between several PMTs [29, 47];

3. a very good temporal resolution to reduce the random coincidence rate, that depends on the light yield and on the scintillation dead time, which is the time required by the detector to process an event [22, 29]. A short scintillation decay time also reduces the detector dead time, allowing data to be acquired at high rates [29];

4. a good energy resolution, i.e., the ability to distinguish gamma rays of different energies, to optimize the rejection of scatter and random events, that depends mainly on the light yield of the scintillator [29, 42, 48].

3.2.2.1 Scintillators

The annihilation photons can interact with the scintillators through the interactions previously described in chapter 2. However, in PET, only Compton scattering and photoelectric effect contribute to the energy deposition within a crystal, allowing the detection of photons; Rayleigh scattering is disregarded at typical PET energies, and pair production is also negligible due to the required energies (the photon energies would need to exceed a lot the 1.022 MeV threshold so that pair production would become significant) [28, 48].

Gamma rays can deposit a fraction or all of their energy in one crystal, and the energy can be deposited in one point of the crystal by photoelectric effect, in several points within the same crystal by successive Compton interactions, or in different crystals (usually adjacent) of the scintillator's block [28, 48].

Inorganic scintillators – solids that scintillate in their crystalline form – are the most frequently used crystals for PET detectors [27, 48]. One common inorganic scintillator used in PET is lutetium yttrium oxyorthosilicate (LYSO) activated with cerium, $Lu_{2(1-x)}Y_{2x}SiO_5$:Ce [49], that presents a fast light emission that ensures a good performance at high interaction rates, more precisely, reducing the dead time effects and discriminating true from random coincidences [28].

An inconvenience of LYSO is that it contains about 2.6% of lutetium-176 (^{176}Lu), a radioactive nuclide with a half-life of 3.8 $\times 10^{10}$ years, that decays by β^- emission (with mean and maximum energy of 182 keV and 593 keV, respectively) to excited states of ^{176}Hf, followed by the emission of gamma rays (with energies of 307 keV, 202 keV and 88 keV, respectively), which produces a constant background signal [28, 50, 51].

This intrinsic radioactivity accounts for about 300 Bq/cm^3, and when self-detected, can misleadingly increase the number of coincidences detected. This inconvenience can be minimized by narrowing the PET system energy window or the coincidence time window [50, 51]. A simplified decay scheme of ^{176}Lu and the electron energy spectrum corresponding to the most probable transition (β_1) can be seen in figure 3.3.

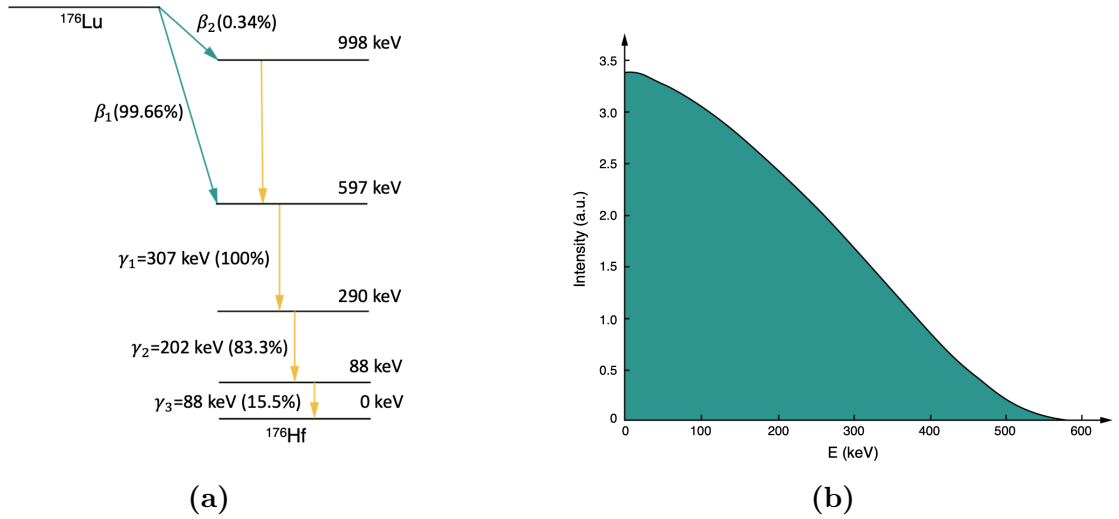

(a) **(b)**

Figure 3.3: ^{176}Lu simplified decay scheme (a) and β-particle energy spectrum corresponding to the β_1 transition (b). Adapted from [50]

3.2.2.2 Photodetectors

PMTs are the most common photodetectors used in PET detectors. These photosensors produce amplified pulses of electrical current in response to the stimulus of the ultraviolet and visible light photons from the scintillating crystals. The signals generated by the photomultipliers are processed using pulse mode, which means that the signals from each interaction are individually processed, to create signals that are able to identify the position in the detector, the deposited energy, and the time of each interaction [28, 46].

Intead of PMTs, solid-state photodetectors can also be used in PET detectors, such as SiPMs, also called solid-state photomultipliers, or multi-pixel photon counters, which are solid-state detectors composed by an array of photodiodes operated in Geiger mode: when a photon is detected, the photodiodes generate a large electric output signal due to internal avalanche multiplication [46, 52].

SiPMs present a good photon detection efficiency, a fast avalanche amplification that allows to obtain very good timing information on the photons arrival time, are easy to use, require a low operation voltage, and provide a high gain, all in a compact size [52, 53].

The energy signals from the detectors are sent to energy discrimination circuits used to reduce misleading events due to scattering interactions in the patient - if the photon energy differs significantly from 511 keV, the interaction is rejected. Nevertheless, some photons escape the patient without being scattered, but then

interact with the detectors by Compton scattering, resulting in an energy deposition smaller than 511 keV, and are still a valid interaction. Therefore, the choice of the energy window can be chosen to encompass only the absorbed photons and reject the maximum of scattered events (with the inconvenience of reducing the number of valid interactions detected), or not reject all Compton scattered events, increasing the sensitivity, but also increasing the number of scattered photons detected [28].

The time signals of the interactions that are not rejected by the energy discrimination circuit are used for coincidence detection and, in some cases, for time-of-flight information [28].

3.2.3 Time of flight PET

As already mentioned, in PET, the positron annihilation is located somewhere along or close to the line that connects the two photon detection positions (LOR) [29]. Time of flight PET (TOF-PET) aims to determine approximately where along the LOR the annihilation event took place by measuring the difference between the times of the interactions of the annihilation photon pair with the detectors [28, 46, 54]. The improvement in the annihilation localization provides more information to the reconstruction algorithm, which, in turn, provides better spatial resolution and reduces the statistical noise for the same number of detected events, when compared to PET with no time of flight information [46, 55].

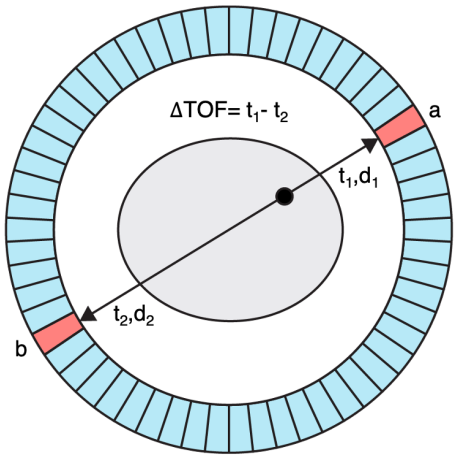

Figure 3.4: TOF Principle [29].

The coincidence time resolution (CTR) of radiation detectors, that expresses the uncertainty in time of a gamma pair detection, is a parameter that influences TOF-PET performance and is mostly influenced by the characteristics of the detectors used, ranging, nowadays, down to hundreds of picoseconds [56, 57, 58]. For any

LOR established between the detectors a and b, the coordinate x, that expresses the distance between the point where the annihilation occurred and the center of the LOR, is equal to $(t_2 - t_1) \times c/2$, with c being the speed of light. Therefore, the measured time difference $(t_2 - t_1)$ correlates with the deduced spatial position by a factor of c/2, and, consequently, the spatial resolution is proportional to the CTR between both detectors [57].

A better perception of the annihilation position along the LOR significantly reduces the contribution of photons that suffer Compton scattering, as well as of other photons that arrive from outside the FOV, allowing the reduction of the background caused by scatter and random coincidences, and the consequent improvement of the signal-to-noise ratio of the obtained images. Besides that, TOF information also allows a considerably reduction in the data processing time [57].

3.2.4 In-beam PET for proton therapy range verification

In online (or in-beam) PET acquisition, performed in the treatment room, with the scanner integrated into the beam delivery system, all positron-emitting species contribute to the obtained activity distribution [26].

On the other hand, in offline acquisitions, performed after the treatment is delivered in a nearby room, only radioisotopes with half-lives comparable to, or longer than the transportation of the patient and setup time, contribute to the image. Therefore, in online range monitoring, the number of physical decays is significantly higher and, consequently, requires shorter times to obtain the images than in the offline approach [12, 26].

In-room PET solves the major limitations of in-beam and offline PET acquisitions. Compared to an in-beam PET system, an in-room full-ring PET scanner improves the sensitivity (greater solid angle) and the quality of the image; compared to offline PET, the in-room acquisition can start shortly after the treatment ($\approx$ 2 minutes) and, therefore, the activity intensity is significantly higher. Nevertheless, the in-room PET system requires the inconvenience of an extended stay of the patient in the treatment room after the irradiation [31].

The most common positron emitters produced as a result of the irradiation of a patient with a proton beam are carbon-11, ^{11}C, oxygen-15, ^{15}O, and carbon-10, ^{10}C, with half-lives of approximately 20 minutes, 2 minutes and 19 seconds, respectively [59].

The delays in acquiring the images in offline PET are enough to disturb the

range monitoring: with a short delay of 10 minutes, a significant fraction of the ^{15}O signal is already lost. PET systems that allow to do image acquisitions to the patient on the treatment couch during treatment or with a minimal delay (<1 minute) after irradiation, and short acquisitions duration (<10 minutes) allow to significantly reduce the biological washout effect and to avoid the displacement of the patient to another room, while collecting a higher statistics PET image [34]. Patient repositioning errors and morphological changes can be additionally minimized, since the image is acquired with the patient in the couch after irradiation, still in the treatment position, according to the treatment planning [12].

Due to the produced positron-emitting species' short half-lives, the low activity density, and the quick washout of a large part of the produced activity, in-beam PET scanners are the preferential solution for range monitoring in proton therapy [59].

The development of a PET system to acquire in-beam images demands a design compatible with the therapeutic proton beam irradiation. From all PET systems developed so far for this purpose, a partial ring PET scanner (with dual-panel) is most frequently proposed, as it is easier to develop and integrate in the proton therapy gantry. This partial-angle coverage results, nevertheless, in limited-angle artifacts in the reconstructed PET image [34].

Therefore, in online acquisitions, PET with TOF information is crucial for proton therapy monitoring, as it allows the reduction of the longitudinal image elongation resulting from the lack of detectors in partial ring scanners, as well as the reduction of the signal-to-noise ratio, and of the data processing time [57].

There is no direct relation between the production of positron-emitting species and dose deposition in proton therapy. Protons lose their energy (deposit dose) by collisional energy losses, and produce positron-emitting species through nuclear reactions, dependent on the proton fluence, the cross-sections of specific reaction channels (that are energy dependent), and the density of target nuclei. These two distinct processes result in a different activity distribution and dose distribution, with barely no activity being observed closely to the Bragg peak, due to the energy thresholds for nuclear reactions to occur (figure 3.5) [12].

Therefore, for proton therapy treatment verification, the PET images acquired must be compared with predicted activity distributions, often calculated by Monte Carlo simulations, that rely on the beam parameters and on the CT images acquired from the patient for treatment planning, and that provide the most accurate

prediction of the activity distribution [12].

The positron emission profile predicted through simulation and the one obtained in the clinical site are compared. If both distributions match well within a small range of uncertainty, the treatment is being correctly delivered; otherwise, differences between the distributions suggest deviations between the delivered and planned treatments, and the treatment plan or the patient setup must be reviewed [60].

In addition, the measured activity distribution in one given fraction may be compared with those from other fractions in order to monitor the consistency of the treatment and resolve if there are relevant changes throughout the treatment [12].

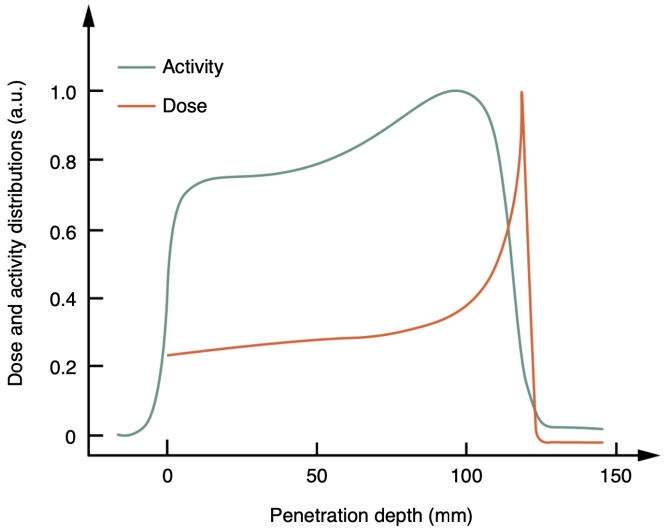

Figure 3.5: Activity and dose distributions obtained from the irradiation of a PMMA phantom with a proton beam. Adapted from [61].

Therefore, proton therapy range verification by means of *in-vivo* PET relies on the accuracy of the activity distributions simulated, that depend on the accuracy of the MC simulation, that depends, in turn, on the accuracy of the cross-sections - measure of the probability for a reaction to occur [22] - data for positron-emitting species production. Different cross-section data sets have been reported by several groups, and diverse experimental channels can be found in the EXFOR (Experimental Nuclear Reaction Data) library [62].

4

Simulation Framework

The approach selected by the TPPT consortium for the simulation of the in-beam TOF-PET prototype developed for range monitoring in proton therapy was to use Geant4 toolkit to develop a framework for MC simulations of the operation of the designed TOF-PET prototype, able to reproduce its detection efficiency.

In this chapter, the simulation framework for the TPPT consortium will be presented.

4.1 Simulation framework for the TPPT consortium

The simulation framework for the TPPT consortium comprises three linked parts developed in C++: simulator, event builder and coincidence sorter (figure 4.1).

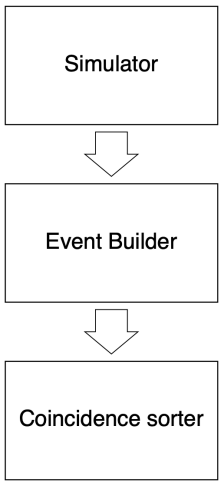

Figure 4.1: Simulation workflow.

The simulator was developed in Geant4. Geant4 produces interactions between the generated particles and the detector (scintillators), but splits the energy depositions in such a way that one interaction can result in several deposition "nodes" that are considerably close in time and space. Those "nodes" would not be individually detected by the real PET scanner, hence the need for event builder, that processes those interactions to represent the realistic depositions that would have been detected by the real PET scanner. After event builder, the coincidence sorter is able to process the deposition events according to the scanner performance settings and collect the number of coincidences resulting from the interactions produced in the simulator and that would have been detected in reality.

Consequently, and as suggested in figure 4.1, the output from the simulator is the input for the event builder, and the output from the event builder is the input for the coincidence sorter.

Nevertheless, although this is the main usage of the simulation framework, the simulator has other options to simulate and investigate different properties other than the number of detected coincidences. In this case, the simulator is used without the need to process the results with event builder and coincidence sorter.

4.1.1 Geant4

Monte Carlo (MC) methods provide solutions to macroscopic systems by simulating their microscopic interactions [63]. They imply the use of random numbers in calculations involved in statistically complex processes that can be described as probabilistic (stochastic) processes, i.e., processes which evolution is determined by random events. MC consists, therefore, in the solution of non-probabilistic problems by probabilistic methods. In computers, this is possible through algorithms of pseudo random number generators which mimic the properties of truly random numbers - if a pseudo random number generator starts from a certain number in the algorithm (called seed), and later on is started from that exact same number, both sequences will be the same, hence the pseudo designation [64].

Geant4 (GEometry ANd Tracking 4) is a general purpose code based on MC simulations developed for particle physics applications [65, 66]. It is widely used in high-energy physics, radiation protection, medical physics and space sciences, and it provides physics models used to simulate the passage of particles through matter [65, 67].

This toolkit allows the definition of a geometrical model, with a variety of

components of different shapes and materials, and it provides an exhaustive set of physics processes that model the behavior of particles [68].

Geant4 simulations are useful to support the design of detectors in their research and development phase (e.g., in medical physics applications, it can be used to accurately reproduce experimental set-ups of, for instance, radiotherapy beams, brachytherapy sources, detectors used for diagnosis, and patient's anatomy [69]), and to understand their response for physics studies. For that, and in order to be possible to propagate individual particles into the detector, it is important to model the behaviors of the interaction of particles with matter, as well as to define the detector's geometry and materials [70].

4.1.1.1 Geant4 architecture

Geant4 provides the abstract interface for different classes, which implementation can either be mandatory or optional, and which purpose is for users to customise the simulation to their particular situation. Three of those classes are mandatory to define: the detector construction, the physics list and the primary generator. Geant4 also provides several optional classes, such as the stepping action [70].

From the G4VUserDetectorConstruction abstract class, the users define all the materials that will be used, the volumes of the detector geometry and their setup, and the detector sensitivities, as well as other properties, such as the detector visualization attributes [70].

A sensitive detector declares a geometric volume sensitive to the passage of particles and is used to simulate the readout of a detector, since several quantities can be collected out of those volumes (e.g., deposited energy and time information) [71]. These sensitive elements are capable of recording information (hits) necessary for the simulation of detector responses [68].

Users must derive their own class from the abstract class G4VUserPhysicsList to define all the particles needed in the simulation and the physics processes (i.e., how the particle interacts with matter, or its decay) involved. Additionally, cut-off values, that consist in range cuts for secondary particles' production (explained with further detail in chapter 6), must also be declared [70, 72]. In conclusion, this class provides the information of when, how and what set of physics is invoked for the simulation in a flexible way [73].

The particle transport in Geant4 simulations starts with the generation of primary particles (for instance, protons or radioactive sources). For that, users have

to derive their own class from G4VUserPrimaryGeneratorAction for generating primary particles and to define, among others, what type of particles will be generated, their kinematics, i.e., energy and direction, and other features, as their charge and polarization [74, 75].

The optional class G4UserSteppingAction provides access to a particle step, which occurs whenever a particle crosses a geometrical volume border or suffers an interaction. This class is used to access several information about a step (e.g., total energy deposited, and information on the particle and on the volume where it stopped) [76].

4.1.2 Simulator

The simulator has two main purposes that can be selected according to what is intended by the user:

1. To simulate the detection of gamma pairs by the detector;
2. To simulate the generation (and consequent detection) of positron-emitting species based on the proton beam configuration.

For the first purpose, the focus is on the transportation of the gammas inside the PET detectors, in order to obtain the hits and coincidence records to provide for the reconstruction group. This purpose is also important to understand the influence of the PET detector components on the number of hits and coincidences detected. For this, it is crucial to have a faithful reproduction of the PET system detector components, which development is presented in chapter 5.

To fulfill this purpose, an approach based in MC methods is used to emit primary particles (such as 511 keV gamma pairs) generated inside the phantom, to track them through the phantom and the PET detector, and to create the resulting deposition events inside the PET detector scintillators.

For the second purpose, the focus is on generating positron-emitting species based on the patient planning treatment, i.e., based on the reproduction of the patient CT and proton beam data, and simulation of their interaction.

Geant4's default positron-emitting species production is, nevertheless, been reported by several groups to not be quite accurate when compared to experimental data. Besides that, LIP's group has tested Geant4's default positron-emitting species production with different physics lists and has concluded that the resulting activity distributions are considerably different. Therefore, it was necessary to compile a

cross-sections versus proton energy data set (presented in chapter 6) to, as a result of proton irradiation, generate positron-emitting species inside a phantom, according to its material composition and to the available cross-sectional information.

In order to organize the developed simulation and to fulfill its purposes, the simulator is organized into four major components:

- Detector - it defines the PET detector geometry, i.e., the scintillators (sensitive volume) and all the other scanner elements;
- Phantom - it defines an object that mimics the human body (or a part of it) or that contains radioactive sources that will be selected to perform the simulation according to its purpose;
- Source - it defines how the chosen primary particles will be emitted;
- Operation mode - Geant4 does not record any data; therefore, to extract data out of the simulation, there are several operation modes that allow to get and organize the information as intended.

The simulator can be configured in a flexible and intuitive manner. Each component is implemented with an abstract interface, to simplify the code customization, modification, the introduction of new features, and the detection of bugs in the code. These characteristics grant the possibility of easily keeping only one version of the code, which guarantees a "low-maintenance" and an intuitive usage of the simulation workflow. This is particularly useful given that it will be handled by multiple users from several groups. The detector components can, for instance, be enabled or disabled in a straightforward way, according to the needs of the simulation, which was particularly useful for the study carried out in chapter 5, dedicated to the analysis of the PET system's detection efficiency. Besides that, it significantly simplifies the process of adding new phantoms, sources or operation modes to the simulator.

4.1.2.1 Detector

The PET system detector, shown in figures 4.2 and 4.3, is composed by scintillator crystals, silicon photomultipliers (SiPMs), printed circuit boards (PCBs), support structures, cooling assemblies, a lower and an upper base, and an enclosure.

As mentioned above, in order to properly simulate the PET system detection performance, it is essential to have a faithful reproduction of the designed prototype. For this, all elements except the scintillators were defined in two approaches, described in further detail in chapter 5: Geometry Description Markup

Language (GDML), a format used to translate Computer-Aided Design (CAD) geometries to Geant4, and G4VSolid, that is based on Geant4 solids, which consist in solids with simple shapes (e.g., rectilinear boxes, spherical and cylindrical sections or shells, and trapezoids).

The detector elements were developed in these two approaches to investigate which was the most adequate to reproduce the prototype, based on a balance between the level of detail and reliability of the detector components, and on the facility of navigating through the geometry, which influences the simulation run time.

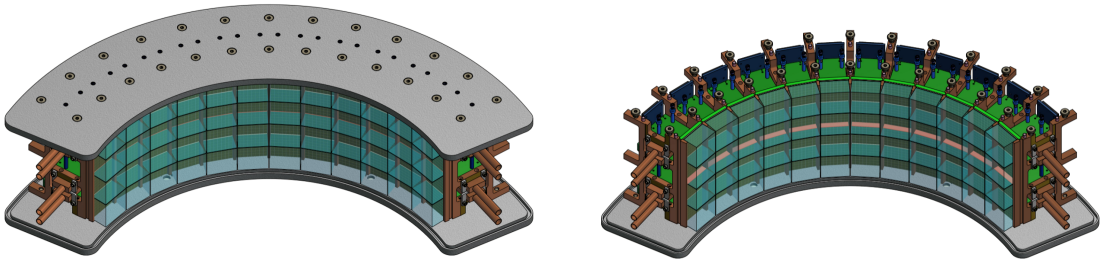

Figure 4.2: PET prototype developed by the TPPT consortium (enclosure not depicted). Detector components presented and described in chapter 5.

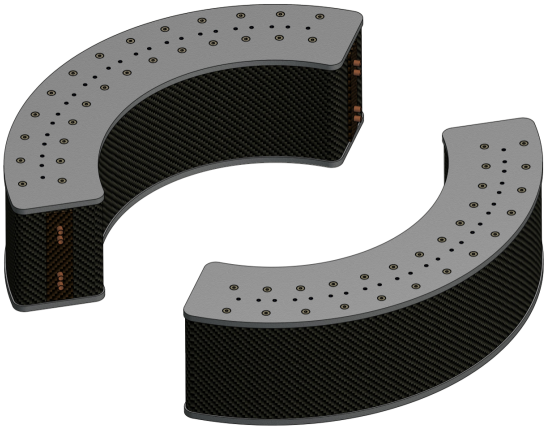

Figure 4.3: PET prototype with enclosure developed by the TPPT consortium.

The PET detector prototype is composed by 6144 scintillators: each detector head has 4 rows and 12 columns of 8 by 8 scintillator arrays. Each scintillator has an associated index, which allows a very fast scoring system due to the fact that the time and energy are recorded independently for each scintillator, through its index.

The scintillating material is made of cerium-doped lutetium yttrium oxyorthosilicate, $Lu_{1.94}Y_{0.06}SiO_5$:Ce, density 7.31 g/cm^3, and each scintillator crystal has 3.005 $\times$ 3.005 $\times$ 15 mm^3 of dimensions and is wrapped on the sides and on the surface

that is facing the phantom with a thin layer of 0.195 mm of teflon (only the face glued to the SiPMs is not wrapped with teflon).

The scintillator arrays are represented by Geant4's G4Box shape (Appendix A), and each assembly of 64 scintillators is placed inside an encapsulation (also G4Box shape) made of teflon, so that there is a layer of teflon in between each crystal, as shown in figures 4.4 and 4.5.

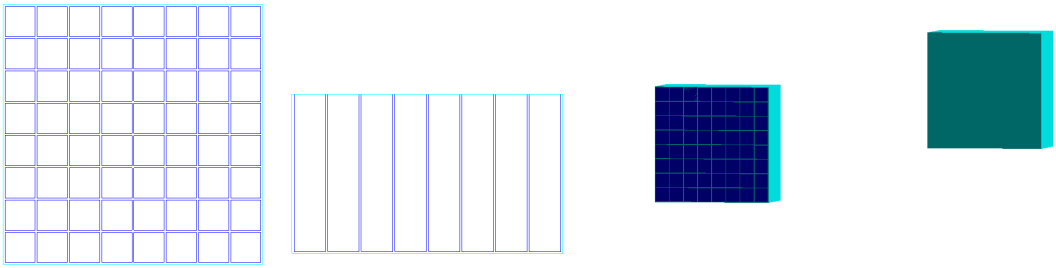

(a) **(b)** **(c)**

Figure 4.4: Scintillator arrays wrapped with teflon: front view (a), top view (b), and two opposite scintillator arrays facing each other (c). The light blue depicts the teflon layer and the dark blue the scintillators.

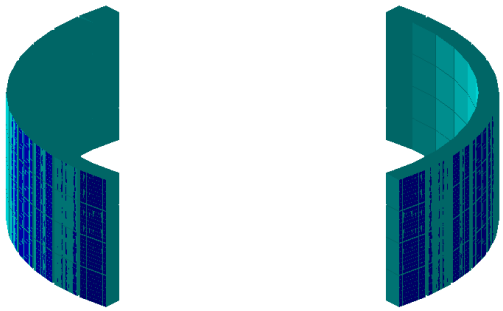

Figure 4.5: Simulation detector: scintillators.

4.1.2.2 Phantom

Several phantoms are available for selection; among the available phantoms, there are a polymethyl methacrylate (PMMA), a Derenzo, and an anthropomorphic phantoms.

The PMMA phantom (chemical formula $(C_5O_2H_8)_n$, density 1.18 g/cm^3), consists on a cylinder of 200 mm length and 200 mm diameter, mimicking a human's head.

The Derenzo phantom is one of the most used phantoms for quality control in nuclear medicine, to determine a system's spatial resolution, and it consists on a PMMA cylinder with a set of water channels (that are filled with positron-emitting radionuclides) separated in a triangular configuration, i.e., it is a phantom with implanted radioactive sources [77].

The anthropomorphic phantom is based on a Digital Imaging and Communications in Medicine (DICOM) file of the patient's CT data, and it is a voxelized phantom obtained by the conversion of the HUs of the CT to density values through a calibration curve. Depending on the obtained density values, a Geant4 material is assigned to each voxel.

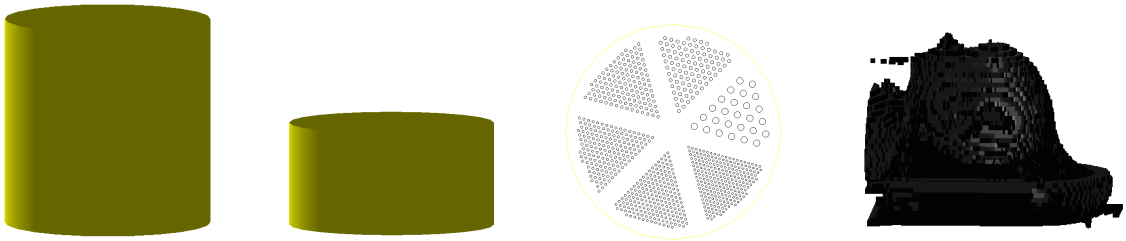

(a) **(b)** **(c)** **(d)**

Figure 4.6: Some available phantoms: PMMA phantom (a); Derenzo phantom (b) and its cross-sectional view (c); anthropomorphic phantom acquired from the CT data of a patient (the couch and the immobilization mask are perceptible) (d).

4.1.2.3 Source

The primary particles are generated according to the selected source, which is defined in the simulator code. Five main sources are defined: a point source, a pencil beam, a material limited source, a natural radioactivity source, and a source from an input file.

The point source involves the emission of primary particles from a stationary point inside the phantom. The point source implies the selection of the primary particle (e.g., gamma pairs of 511 keV, ^{15}O, ^{11}C, or any other positron-emitting species), of a time generator, that defines how the particles are emitted over time (a constant, uniform or exponential emission over time are available for selection), of the direction of emission, and of the coordinates of the point of emission.

The pencil beam implies the selection of the primary particle (e.g., protons) and its respective energy, the time generator, the direction and coordinates of the point of emission, the number of primary particles that compose the beam, and the beam profile (e.g., defined by a Gaussian distribution).

The material limited source limits the primary particles generation to a specific material. It implies the selection of the primary particle (e.g., ^{15}O, ^{11}C, or any other positron-emitting species), the time generator, the coordinates of the origin of a bounding box and its respective dimensions, and the identification of the material. Candidate positions for the generation of the primary particles are successively selected uniformly inside the bounding box: if the material is the identified one, the primary particle is generated in that position; otherwise, the position is rejected. This source was specifically developed for the Derenzo phantom, which water channels are filled with positron-emitting species.

The natural radioactivity source is, in a way, a material limited source, which was developed to understand how the LYSO intrinsic radioactivity would influence the PET system's hits and coincidences detection performance. With this source, a uniform time generator is defined within a selected time window. Then, throughout that time window, scintillators are randomly selected and positions inside those scintillators are also randomly selected to generate electrons (with a specified energy distribution as the one from figure 3.3b and with a random direction). Finally, the product of ^{176}Lu decay, an excited state of ^{176}Hf (energy equal to 597 keV, according to figure 3.3a), is generated and decays to the stable state by emitting gammas.

The source can also be defined by an input file (called "from file source"). This input file - obtained from the "positron-emitting species generator" mode explained below - contains the information on the generated positron-emission species particle type, its energy, the coordinates of the position where it was generated, and the direction and time of emission. This source was created due to the fact that the generation of the positron-emitting species can potentially take hours. If, in addition, the number of coincidences resulting from those positron-emitting species had to be acquired, the simulation run time would even take longer. Therefore, this source allows to subdivide the simulation in two parts to optimize the run time: one to obtain the primary particles, and other to simulate their interaction with the phantom and detector.

4.1.2.4 Operation mode

Several operation modes are available in the simulator:

- "Graphical User Interface (GUI)" mode allows to visualize the defined geometry, and to get information about it (for instance, if there are overlaps in the geometry), as well as about trajectories and hits. It also allows the user to rotate, zoom, and to adjust the visualization of the geometry as preferred.

- "Multiple events" mode allows to mimic the real operation of the PET detector, i.e., it allows to save information the same way as the real PET scanner saves it: the energy deposition on the scintillators. After a certain number of primary particles are emitted in the simulation, there is a record of the scintillator number (given by its index), of the energy deposited, and of the time of interaction. This mode output - that will be the input for the event builder - consists on a record of the scintillator index followed by the time and energy of the deposition "nodes" that occurred inside the corresponding scintillator:

$$\#0$$
$$t_{Node_1} \quad E_{Node_1}$$
$$t_{Node_2} \quad E_{Node_2}$$
$$...$$
$$t_{Node_n} \quad E_{Node_n}$$
$$\#1$$
$$t_{Node_1} \quad E_{Node_1}$$
$$...$$
$$t_{Node_m} \quad E_{Node_m}$$
$$...$$

- "Tracing" mode allows to get information from the defined geometry. In particular, it allows to get information on the volumes' boundaries crossed along the direction of emission specified for the primary particle. This mode implies the use of a specific Geant4's particle: the geantino - a virtual particle that does not interact with materials and that only undertakes transportation processes [78]. In this mode, the coordinates of the position where a different volume is reached are presented.

- "Deposition statistics" mode allows to understand how the energy is deposited in the scintillators. It registers the fraction of a particular type of events (e.g., no interaction with the scintillators or interactions with only one, two, three, four or five or more scintillators), compared to the total number of emitted gammas.

- "Positron-emitting species generation" mode calculates the generation probability of all positron-emitting species for each primary proton, based on the phantom composition and on the production cross-sections (in milibarn) as a

function of the proton energy (in MeV) information, which is provided as an input file such as:

#6 12 C11

E_1 CS_1

E_2 CS_2

...

#8 16 C11

E_3 CS_3

E_4 CS_4

...

where the numbers 6 and 12 and 8 and 16 denote, respectively, the atomic number and the mass number of the atom that originates the positron-emitting species (in this case, carbon-11).

After each step of the proton, and based on relative probabilities, one of the possible reactions resulting from the bombardment of the phantom with a proton beam from that input file is triggered and it is checked if it occurred the generation of positron-emitting species. The data of the generated species (chemical symbol followed by the mass number, energy, position, direction and time of generation) is saved on a file:

#1

C11 0 x_1 y_1 z_1 0 0 1 t_1

O15 0 x_2 y_2 z_2 0 0 1 t_2

...

#2

N13 0 x_3 y_3 z_3 0 0 1 t_3

C11 0 x_4 y_4 z_4 0 0 1 t_4

...

This output file can not only be used as an input file for the primary particle source ("from file source"), to simulate the interaction of the positron-emitting species with the phantom and the detector, as it can also be used to obtain the activity distributions of the generated positron-emitting species.

- "Dose extractor" mode records the total energy deposited per path length as an output file, which information can then be plotted.

4.1.3 Event Builder

As mentioned, the event builder receives as an input the output from the simulator and reads and processes the depositions produced in the simulator phase per simulator, being subdivided into three phases: pre-cluster, cluster, and event building.

To reduce the time it takes to perform the clustering of the data resulting from the simulator output, a pre-cluster phase was developed: for each scintillator, each deposition node is compared to the next one and nodes that are close in time are merged. For this, a maximum time variation is defined (e.g., 0.1 ns). If the time difference between two consecutive nodes is smaller than the defined time variation, both nodes are merged; otherwise, the next node is considered a new cluster and is compared to the one that follows.

When two nodes are merged, the energy is considered to be the sum of the energies of both nodes and the time is considered to be the time weighted by energy (E_{Node} is the energy deposited on a scintillator in one of the nodes of an interaction, in MeV, and t_{Node} the respective time of interaction, in ns):

$$E = E_{Node_m} + E_{Node_n} \tag{4.1}$$

$$t = \frac{t_{Node_m} \times E_{Node_m} + t_{Node_n} \times E_{Node_n}}{E} \tag{4.2}$$

In the cluster phase, all merged nodes resulting from the pre-cluster phase are sorted by time and are merged until there are no more merging attempts per scintillator; while pre-clustering analyzes only two consecutive nodes, clustering is an iterative cycle that merges all deposition nodes until no more merges are possible.

Finally, for the event building phase, the detectors' integration and dead times are taken into consideration. When merging two clusters, if the second cluster is within the integration time (e.g., within 40 ns), the energies are added and the time is considered to be the time of the first cluster. If the cluster arrives in the dead time (e.g., within 100 ns), the deposition is ignored. This has to due with the fact that two interactions have to be separated by a finite amount of time (called the

dead time) in order to produce distinct signals in a radiation detector - if a second interaction occurs during that time interval, the signal is lost [28].

Additionally, the event builder can also introduce a Gaussian blurring to the event times in order to simulate the uncertainty in the detection time of gammas, determined by the coincidence time resolution (CTR).

The energy resulting from the cluster phase is also submitted to a preliminary optional energy filter, with all energy depositions bellow 0.311 MeV and above 0.711 MeV discarded.

The output of this phase consists in the record of all scintillator indexes, followed by all the depositions information resulting from the event building phase:

$$\#0$$

$$t_{Cluster_1} \quad E_{Cluster_1}$$

$$t_{Cluster_2} \quad E_{Cluster_2}$$

$$...$$

$$t_{Cluster_n} \quad E_{Cluster_n}$$

$$\#1$$

$$t_{Cluster_1} \quad E_{Cluster_1}$$

$$...$$

$$t_{Cluster_m} \quad E_{Cluster_m}$$

$$...$$

with time in ns and energy in MeV.

4.1.4 Coincidence sorter

Coincidence sorter receives and reads the depositions information of the event builder output and finds coincidence pairs through previously defined time and energy windows. After discarding depositions outside of the considered energy window, the deposition events are sorted by time, and coincidences are found and saved: only if exactly two detectors show an energy deposition within the same time window (e.g., 4 ns), both scintillator indexes are recorded, as well as the time difference between the depositions in both scintillators, and the time of the first interaction.

As mentioned, in this phase there is a precise energy filter, that only considers coincidences if the energy deposited is close to 0.511 MeV (e.g., 0.511 ± 10% MeV).

Finally, coincidences detected in the same head of the PET detector are rejected, since the scanner is developed to reject those coincidences in reality.

The coincidence sorter output records:

$$\text{Index}_1 \quad \text{Index}_2 \quad \text{t}_1\text{-t}_2 \quad \text{t}_1$$

with $t_1 - t_2$ in ps and t_1 in ms.

5

Development of the PET system simulation model

The simulation of the PET system prototype intends to faithfully reproduce the prototype developed by the TPPT consortium. This faithful reproduction allows to trustfully evaluate the performance of the PET system in what concerns its efficiency in detecting coincidences, which is an important feature for image reconstruction purposes.

All detector elements except the scintillators were defined by two approaches, as mentioned in chapter 4, each with their own advantages and disadvantages: GDML and G4VSolid.

Since it is obtained directly by the prototype's CAD file, the GDML approach contains a highly detailed information on the detector elements, therefore defining a more accurate geometry. Nevertheless, this approach is based on tessellated objects, i.e., generic solids that are defined by a certain number of facets, that can have a triangular or quadrangular shape [78, 79]. Some geometry overlaps can arise in this approach due to these tessellated objects. Besides that, due to the high number of tessellated objects and to the higher level of detail, the simulations can be potentially slower.

On the other hand, the geometry defined with the G4VSolid approach implied some approximations imposed by Geant4's available geometrical shapes. Despite the less accurate geometry due to those approximations, the G4VSolid is a more controllable approach, not only because it is not dependent on the CAD file, i.e., changes in the prototype can be immediately implemented without waiting for the CAD file update, but also because overlaps in the geometry can be easily detected and solved.

5.1 Detector elements developed in G4VSolid approach

All detector elements from figures 4.2 and 4.3 were developed in the G4VSolid approach, and the approximations made to reproduce the PET system detector with this approach will be presented in this section. The elements defined in this approach consisted on the upper and lower bases, the enclosure, the SiPMs, the PCBs, the copper structure, and the cooling assemblies. The higher the atomic number of the detector element materials, and the closer to the scintillators, the better it was tried to reproduce those components.

5.1.1 Upper and lower bases

The upper and lower bases are composed by two adjacent plastic and copper plates, which were reproduced using the G4Tubs geometrical shape (Appendix A). Each base consists in a 120° segment made of 6.35 mm thick acrylonitrile butadiene styrene (ABS) plastic, with chemical formula $(C_8H_8 \cdot C_4H_6 \cdot C_3H_3N)_n$ and density equal to 1.07 g/cm^3, and a thin copper plate of 0.79 mm, to which Geant4's copper material was assigned (density 8.96 g/cm^3) [80, 81].

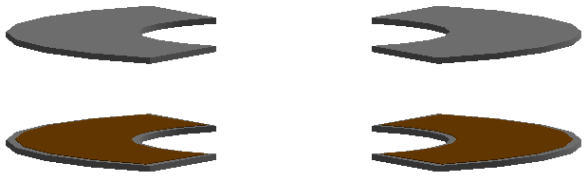

Figure 5.1: Simulation detector: upper and lower bases. In gray, the ABS plastic; in brown, the copper plates.

5.1.2 Enclosure

The enclosure contains a front, back and lateral windows. Each window is composed by 1 mm thick carbon fiber, to which Geant4's carbon material was assigned (density 2.0 g/cm^3) [81]. The G4Tubs shape (Appendix A) was also used to define all of the windows that compose the enclosure.

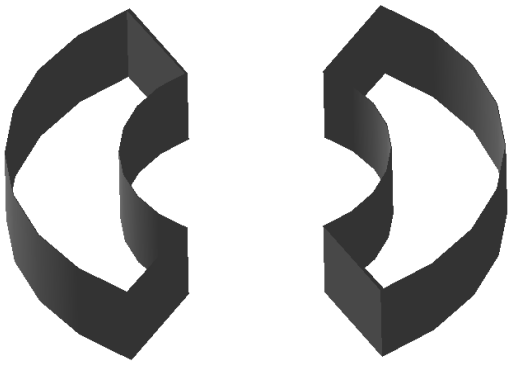

Figure 5.2: Simulation detector: enclosure.

5.1.3 Silicon Photomultipliers

The SiPMs used in the PET system prototype (figure 5.3) were from Hamamatsu, a manufacturer of photonics devices.

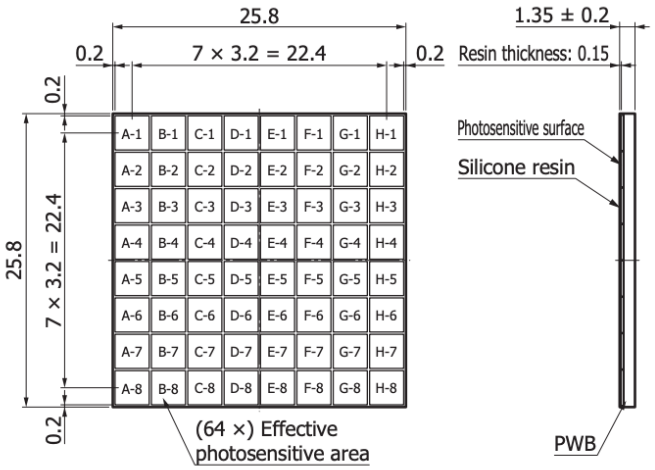

Figure 5.3: Hamamatsu's SiPMs used in the PET system. Top view on the left; side view on the right. Taken from [82].

Each silicon photomultiplier module depicted in figure 5.3 is glued to an 8 by 8 scintillator array in the PET system, and was represented by Geant4's G4Box shape (Appendix A) in the G4VSolid approach.

As for the SiPMs' material, Hamamatsu was contacted concerning the thickness and composition of the photosensitive surface and silicone resin, but only confirmed that the photosensitive layer was a silicon semiconductor of p-type, claiming they could not disclose any more information about the product.

Hence, due to the lack of information on the SiPMs' material, an approximation

on its composition and density had to be done for the detector simulation. For that, and considering that the silicone resin used is unknown, a mixture of the two other components, the photosensitive layer and the printed wire board (PWB) (a more frequent noun to designate PCBs in Japan [83]), was defined to be assigned to the SiPMs.

To define that mixture, first it was necessary to know the volume occupied by each component per module, and then, based on the materials' densities, it was possible to calculate their mass fraction to then define the mixture in Geant4.

The total volume of the SiPM module, the volume of the photosensitive surface, and the volume of PCB were calculated. Based on the literature, the photosensitive surface thickness was considered to be 300 μm and to be made of pure silicon (Si) [84]. The PCB volume was calculated from the difference between the total SiPMs' volume and the volume of the photosensitive surface, since the silicone resin composition used is unknown and its thickness is negligible:

$$V_{SiPM} = 25.8 \times 25.8 \times 1.35 = 0.8986\,cm^3$$

$$V_{Photosensitive\,surface} = 24 \times 24 \times 0.3 = 0.1728\,cm^3$$

$$V_{PCB} = V_{SiPM} - V_{Photosensitive\,surface} = 0.8984\,cm^3$$

Based on the literature [85, 86, 87, 88], the PCB composition is usually composed by a mass fraction of 40% of metals (main component is copper, followed by iron and tin, even though in much smaller concentrations), 30% plastics (usually epoxy) and 30% ceramics (usually fiber glass). Therefore, the PCB composition for the simulation purposes was considered to be the one presented in table 5.1.

PCB composition	
Molecule/element	**Mass fraction (%)**
Epoxy ($C_{21}H_{25}ClO_5$)	30
Fiber glass (SiO_2)	30
Cu	30
Fe	5
Sn	5

Table 5.1: PCB material composition.

Using the relation

$$\rho = \frac{m}{V} \qquad [\mathrm{g/cm^3}] \quad (5.1)$$

and knowing the densities of each element/molecule, as well as the total volume of silicon and PCB, the mass of each element/molecule could be calculated, according to table 5.2.

Molecule/Element	Density (g/cm^3)	Volume (cm^3)	Mass (g)
Si	2.33	0.1728	0.4026
Epoxy	1.1	0.8984	0.9882
Fiber glass	2.65	0.8984	2.3809
Cu	8.96	0.8984	8.0500
Fe	7.874	0.8984	7.0743
Sn	7.31	0.8984	6.5676

Table 5.2: PCB composition: mass of each molecule/element.

The mass of PCB could then be calculated from the mass fraction of each molecule/element (30% of epoxy, 30% of fiber glass, 30% of copper, 5% of iron, and 5% of tin):

$$m_{PCB} =$$
$$0.3 \times 0.9882 + 0.3 \times 2.3809 + 0.3 \times 8.0500 + 0.05 \times 7.0743 + 0.05 \times 6.5676 = 4.1079\, g$$

And also the PCB density:

$$\rho_{PCB} = \frac{4.1079}{0.8984} = 4.57\, g/cm^3$$

Finally, the mass fraction of the SiPM material, as well as its density could be calculated:

$$\%(m/m)_{Si} = \frac{m_{Si}}{m_{Si}+m_{PCB}} \times 100 = \frac{0.4026}{0.4026+4.1079} \times 100 = 8.93\%$$

$$\%(m/m)_{PCB} = \frac{m_{PCB}}{m_{Si}+m_{PCB}} \times 100 = \frac{4.1079}{0.4026+4.1079} \times 100 = 91.07\%$$

$$\rho_{SiPM} = \frac{Si_{fm} \times m_{Si} + PCB_{fm} \times m_{PCB}}{V_{SiPM}} = \frac{0.0893 \times 0.4026 + 0.9107 \times 4.1079}{0.8986} = 4.20\, g/cm^3$$

Figure 5.4: Simulation detector: SiPMs.

5.1.4 Printed Circuit Boards

The PCBs were simplified to Geant4's G4Box (Appendix A) shape, as it can be seen in figure 5.5. The PCB material was defined according to the mass fraction and density calculated for the PCB that composes the SiPMs: mass fraction of 30% of epoxy, 30% of fiber glass, 30% of copper, 5% of iron, 5% of thin, and with a density of 4.57 g/cm^3.

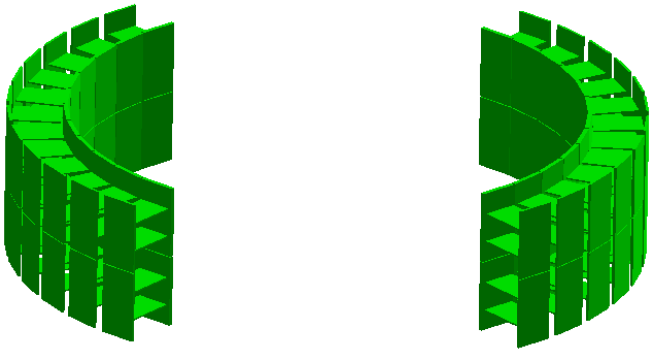

Figure 5.5: Simulation detector: printed circuit boards.

5.1.5 Support structures

The support structures are composed by copper "ribs" that hold up all the prototype components. The ribs are made of copper 110, a copper alloy that contains at least 99.9% copper, and, for that reason, the material used was Geant4's copper material (density 8.96 g/cm^3) [81, 89].

The ribs shape and their positioning between the scintillators and the PCBs in the prototype can be seen in figure 5.6. Due to the complex shape of the ribs and to their disposition on the PET system prototype, several geometric approximations had to be done to place them in the detector without interfering with the rest of the geometry.

More precisely, the columns positioned in between the scintillators and the PCBs were simplified to trapezoidal and rectilinear box shapes, G4Box and G4Trd (Appendix A), respectively, to fit in between those components. The top view of the ribs both from the prototype and from the simulation can be compared in figure 5.7.

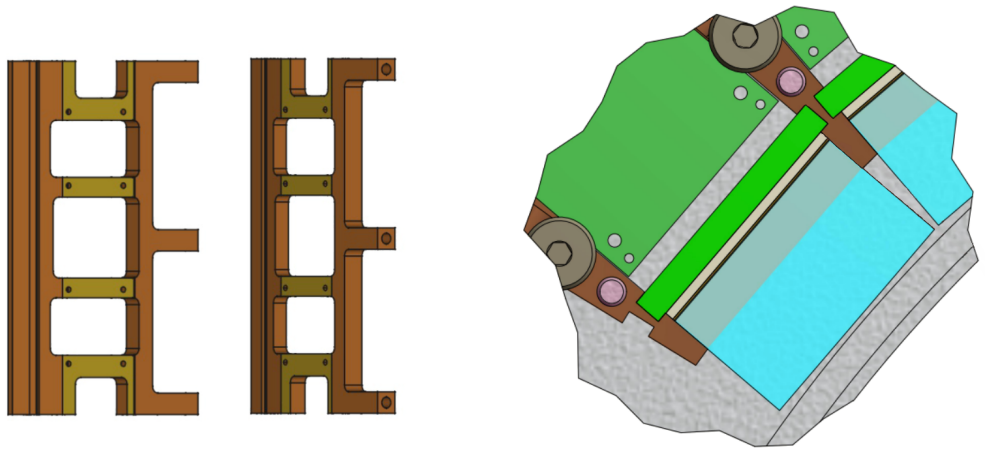

(a) **(b)**

Figure 5.6: PET prototype's support structures in detail. Rib on the left (a); top view detail of the ribs' positioning in between the scintillators (in blue) and the PCBs (in green) on the right (b).

(a) **(b)**

Figure 5.7: Top view of a rib. The geometrical approximations made from the prototype unit (a) to the one developed in the G4VSolid approach (b) are perceptible.

The round edges that are perceptible in figure 5.6a were not represented in the G4VSolid approach, since it is not possible to reproduce them simply with the available geometrical shapes. Therefore, the four horizontal copper columns were simplified to rectilinear shapes, G4Box (Appendix A), as it can be observed in figure 5.8. The holes designed for the screws were not represented as well, due to their negligible size.

The total volume of the prototype's rib was 13.8 cm^3 and the total volume of the rib defined with the G4VSolid approach was also 13.8 cm^3, which means that despite not having the exact same shape, the volume occupied by the support structures is exactly the same both in the PET prototype and in the PET detector developed for

the simulation. The final support structures developed in the G4VSolid approach can be seen in figure 5.9.

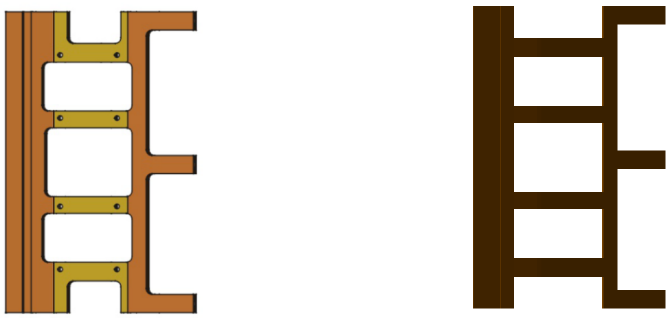

(a) **(b)**

Figure 5.8: Lateral view of the ribs. The geometrical approximations made from the prototype rib (a) to the one developed in the G4VSolid approach (b) are perceptible.

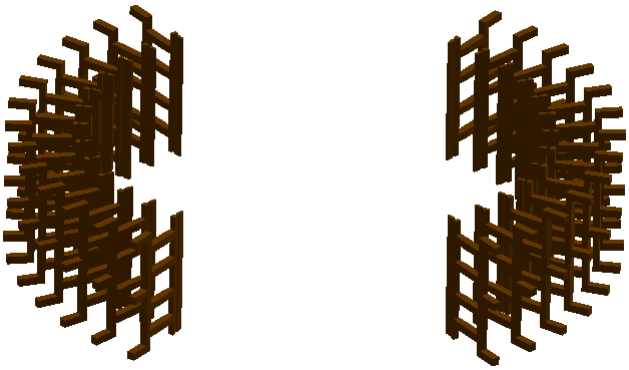

Figure 5.9: Simulation detector: support structures.

5.1.6 Cooling assemblies

The cooling assemblies consist on four copper 110 (Geant4's copper material, density 8.96 g/cm^3) tubes, each with a pipe filled with water (chemical formula H_2O, density 1.0 g/cm^3) inside [81].

According to the prototype, the pipe filled with water should be represented by a bent tube with an elliptical cross-section. In Geant4, this could be approximately obtained by superimposing two G4Torus shapes (Appendix A).

Nevertheless, a more simple solution was to develop an equivalent water volume with the G4Tubs shape (Appendix A), placed inside each copper box, also represented with the G4Tubs shape, as shown in figure 5.10.

Figure 5.10: Simulation detector: cooling assemblies.

5.2 Detector elements reproduced in GDML approach

The GDML approach was, as mentioned, obtained directly from the PET prototype's CAD file. The file (provided by LIP Lisboa's group) with the geometry defined in GDML only contained the lower base, the support structures, the cooling assemblies, the PCBs, and the SiPMs. However, in that version there were some overlaps caused by the cooling assemblies resulting from the GDML to Geant4 conversion method. Therefore, the cooling assemblies were removed from the GDML file, so that there were no overlaps in the geometry.

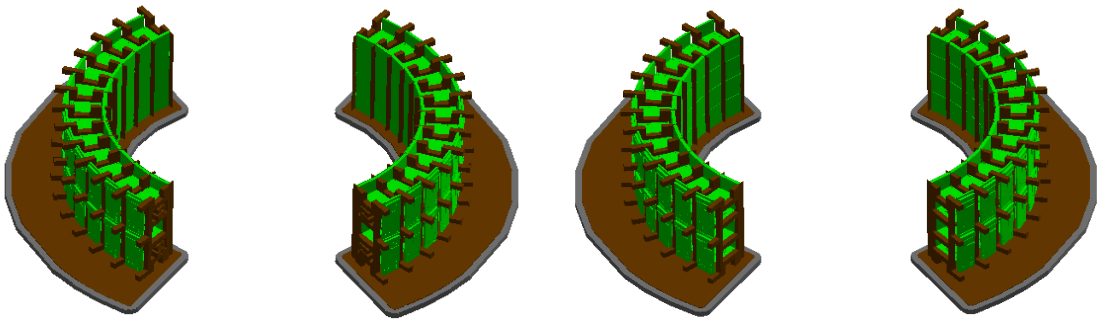

(a) **(b)**

Figure 5.11: Geometry defined in the GDML approach. First version with overlaps caused by the cooling assemblies (a); second version with no overlaps, after the removal of the cooling assemblies (b).

Furthermore, there were no materials assigned to the detector elements in the GDML file, and for that reason, the exact same materials defined in the G4VSolid approach were likewise defined in the GDML file.

5.3 Geometry tests

To make sure the geometry developed for simulation purposes was correctly positioned and its dimensions were in accordance with the PET system prototype developed by the TPPT consortium, several tests were made to check the detector geometry.

For that, the simulator's tracing mode was used to track the geantino particle, shot from different positions and in several directions, to understand if the materials and thicknesses crossed were consisted with the PET system prototype. Tracing mode was used to help checking the dimensions and positioning of all detector elements on the geometry, with particular focus on the scintillators (figures 5.12 and 5.13).

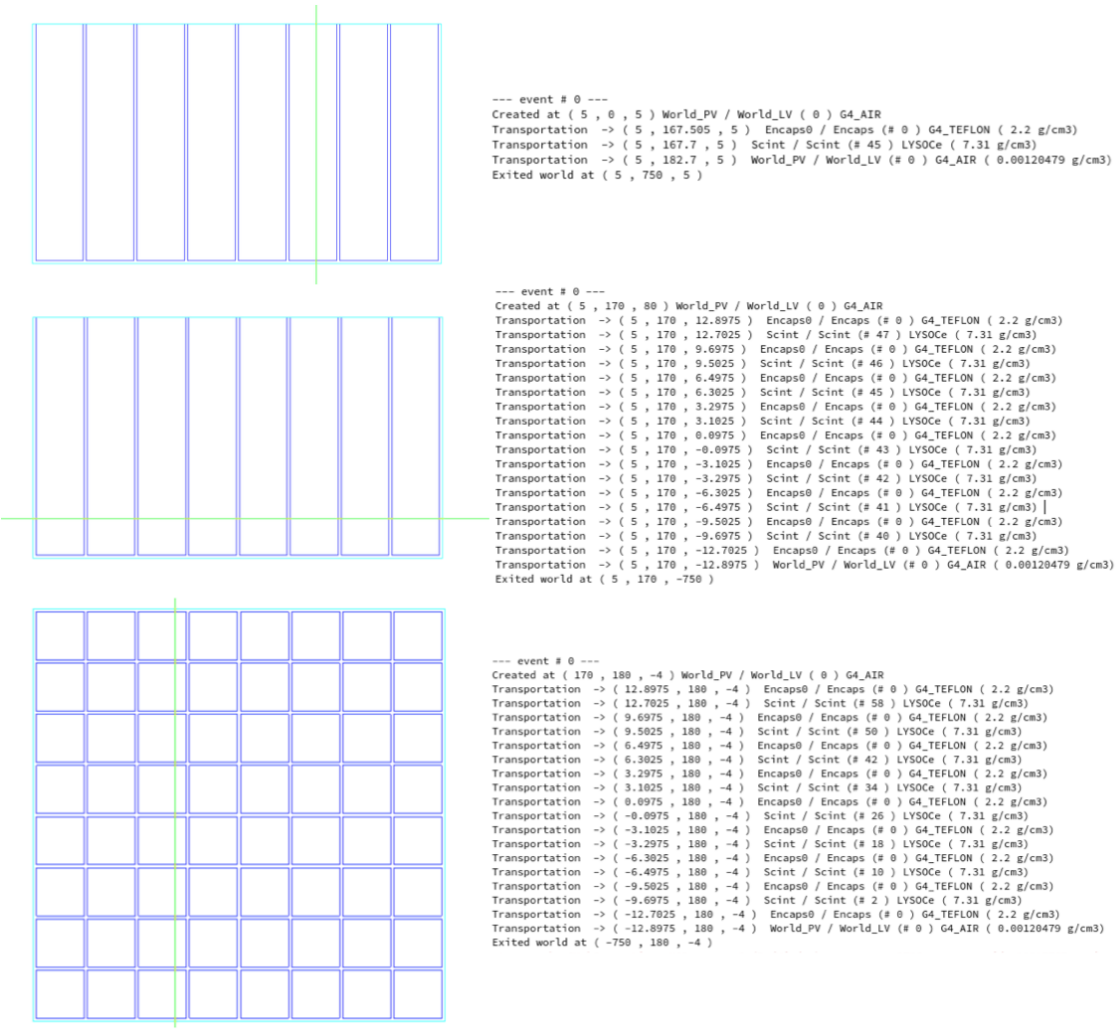

Figure 5.12: Tracing mode report when checking the wrapped scintillators dimensions and positioning. From top to bottom: longitudinal, transverse and vertical emission of the geantino relatively to the scincillators' array.

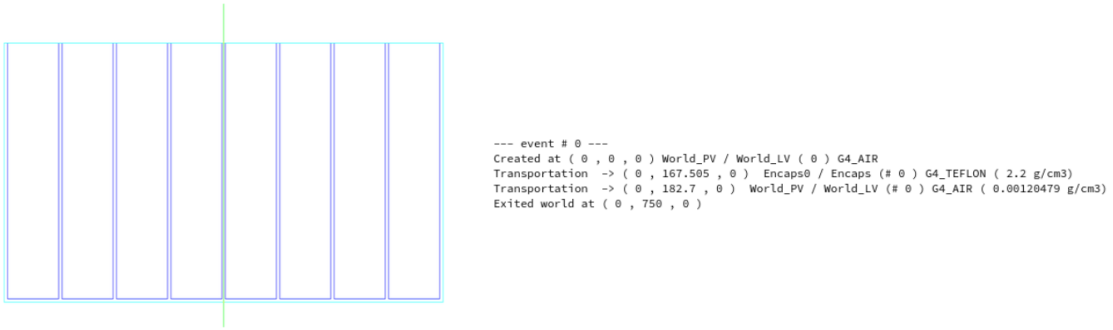

```
--- event # 0 ---
Created at ( 0 , 0 , 0 ) World_PV / World_LV ( 0 ) G4_AIR
Transportation  -> ( 0 , 167.505 , 0 )  Encaps0 / Encaps (# 0 ) G4_TEFLON ( 2.2 g/cm3)
Transportation  -> ( 0 , 182.7 , 0 )  World_PV / World_LV (# 0 ) G4_AIR ( 0.00120479 g/cm3)
Exited world at ( 0 , 750 , 0 )
```

Figure 5.13: Tracing mode report when checking the PET system radius.

After all detector elements were defined in the G4VSolid approach and positioned in the geometry, a final verification was made recurring to Geant4's command *geometry/test/run*, that checks if there are overlapping volumes in the detector (figure 5.14) [79].

```
Checking overlaps for volume Holder_PV (G4Box) ... OK!
Checking overlaps for volume Holder_PV (G4Box) ... OK!
Checking overlaps for volume Holder_PV (G4Box) ... OK!
Checking overlaps for volume Holder_PV (G4Box) ... OK!
Checking overlaps for volume Holder_PV (G4Box) ... OK!
Checking overlaps for volume Holder_PV (G4Box) ... OK!
Checking overlaps for volume CopperPipeHolder_PV (G4Tubs) ... OK!
Checking overlaps for volume WaterPipe_PV (G4Tubs) ... OK!
Checking overlaps for volume CopperPipeHolder_PV (G4Tubs) ... OK!
Checking overlaps for volume WaterPipe_PV (G4Tubs) ... OK!
Checking overlaps for volume CopperPipeHolder_PV (G4Tubs) ... OK!
Checking overlaps for volume WaterPipe_PV (G4Tubs) ... OK!
Checking overlaps for volume CopperPipeHolder_PV (G4Tubs) ... OK!
Checking overlaps for volume WaterPipe_PV (G4Tubs) ... OK!
Checking overlaps for volume CopperPipeHolder_PV (G4Tubs) ... OK!
Checking overlaps for volume WaterPipe_PV (G4Tubs) ... OK!
Checking overlaps for volume CopperPipeHolder_PV (G4Tubs) ... OK!
Checking overlaps for volume WaterPipe_PV (G4Tubs) ... OK!
Checking overlaps for volume CopperPipeHolder_PV (G4Tubs) ... OK!
Checking overlaps for volume WaterPipe_PV (G4Tubs) ... OK!
Checking overlaps for volume CopperPipeHolder_PV (G4Tubs) ... OK!
Checking overlaps for volume WaterPipe_PV (G4Tubs) ... OK!
Geometry overlaps check completed !
```

Figure 5.14: Partial report of Geant4's *geometry/test/run* command. No overlaps were found.

Once the detector elements were verified to be correctly positioned, and since no overlapping volumes were found, the defined detector was ready to be used in the simulations.

5.4 Simulation detector: comparison of geometry definition approaches

As mentioned in the previous sections, the detector geometry (except the scintillators) was developed in two approaches: GDML and G4VSolid.

Due to the approximations made in the G4VSolid approach, and in order to validate it, a comparison between the GDML and G4VSolid approaches was made, by analyzing potential differences in terms of number of coincidences and total energy deposited in the scintillators. However, this comparison was only performed for part of the geometry, due to the detector elements represented in the GDML file.

Additionally, a comparison between the geometry with just the scintillators enabled and the G4VSolid approach with all elements enabled was performed, also with the purpose of comparing the coincidences and the total energy deposited in the scintillators in both situations, and to conclude if the simulations should be run with all geometry elements enabled or if the geometry with only the scintillators enabled is enough.

The comparison between the mentioned scenarios was performed by selecting a point source of 511 keV gamma pairs positioned in the center of the PMMA phantom. The simulation was run for 10 million emission events with three different seeds and the output obtained was analyzed in terms of detected hits, number of coincidences obtained, energy deposition, and simulation run time.

5.4.1 GDML and G4VSolid comparison

The comparison between the GDML and the G4VSolid approaches was performed in the same conditions, i.e., with the same geometry elements enabled for the G4VSolid approach - the GDML file was extracted from the CAD file and the version in figure 5.15a, the one with no overlaps, was the one used for the comparison - and the same materials definition in both.

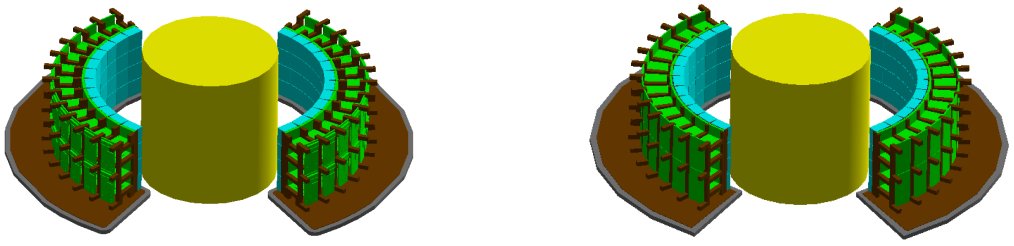

(a) GDML **(b)** G4VSolid

Figure 5.15: Geometry selected for the comparison of the GDML and G4VSolid approaches.

5.4.1.1 Detected hits

The number of detected hits with the GDML and G4VSolid approaches are presented in tables 5.3 and 5.4, respectively.

From the total number of scintillators hit, the single hits (i.e., when one gamma hits one scintillator and the other escapes without being detected) and the multiple hits (i.e., when more than two scintillators are hit within the same time window resulting, for instance, from a simultaneous single hit and coincidence) are discarded to obtain the total number of coincidences.

GDML				
	No. hits	**Single hits**	**Multiple hits**	**No. coincidences**
Seed 1	313333	285850	13757	13726
Seed 2	313197	285586	13818	13793
Seed 3	311711	284391	13673	13647
Sum	938241	855827	41248	41166

Table 5.3: Detected hits with the GDML approach.

G4VSolid				
	No. hits	**Single hits**	**Multiple hits**	**No. coincidences**
Seed 1	312903	285792	13563	13548
Seed 2	312978	285638	13684	13656
Seed 3	312017	284507	13770	13740
Sum	937898	855937	41017	40944

Table 5.4: Detected hits with the G4VSolid approach.

Since the exact same conditions were simulated from seed to seed, the number of hits and coincidences were added to increase, and therefore improve, the output statistics.

From the detected hits, it can be observed a difference in absolute value of 0.04% in the number of hits, of 0.01% in the number of single hits, of 0.56% in the number of multiple hits, and of 0.54% in the number of coincidences between the GDML and the G4VSolid approaches, and, therefore, it can be concluded that there are no significant differences in the number of detected hits.

5.4.1.2 Coincidences

Table 5.5 presents the number of coincidences and respective standard uncertainties (given by $\sqrt{No.Coincidences}$) for both approaches.

	GDML		G4VSolid	
	No. coincidences	σ	**No. coincidences**	σ
Sum	41166	351	40944	350

Table 5.5: Total number of coincidences and respective standard uncertainties for the GDML and G4VSolid approaches.

The difference between the total number of coincidences ($\Delta_{Coincidences}$=41166-40944=222) is within one σ and is equal to 0.5% in absolute value, and, therefore, there is no significant difference between the number of coincidences in both approaches.

Despite no differences were detected in the detected hits and number of coincidences, the spatial distribution of the energy depositions could be different for both approaches, which would produce different image reconstruction results. Hence, the energy deposition per scintillator was plotted for both approaches.

5.4.1.3 Energy deposition

Figure 5.16 depicts the total energy deposition (in MeV) per scintillator for both approaches.

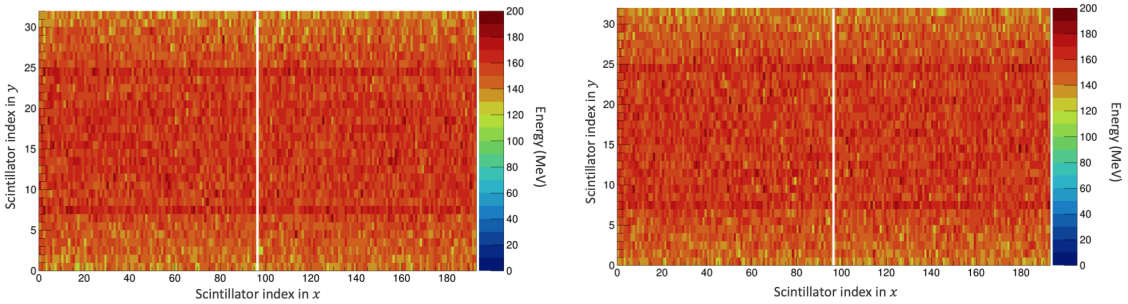

(a) GDML **(b)** G4VSolid

Figure 5.16: Total energy deposited (in MeV) per scintillator in the GDML and G4VSolid approaches.

In these plots, the scintillador index in x is given by the scintillators' position in the column (12 rows of 8 by 8 scintillator arrays makes up a total of 96 columns) and the index in y is given by its position in the line (4 lines of 8 by 8 scintillator arrays makes up a total of 32 lines), as depicted in figure 5.17.

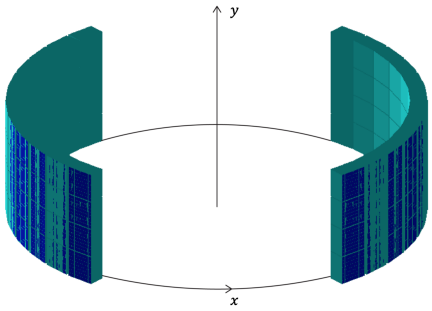

Figure 5.17: Scintillator indexes in x and y.

From figure 5.16, three conclusions can be drawn:

1. There is a symmetry between both PET detector heads;
2. The middle scintillators present a higher energy deposition, which is expected due to the solid angle covered as a consequence of the source being positioned in the center of the PET system - the scintillators nearest to the source will present a higher energy deposition than the ones further apart.;
3. Two rows of scintillators (with y index equal to 8 and 25) present a higher energy deposition than their neighbors.

Due to the symmetry between both PET detector heads, the energy profile (i.e., the histogram projection), representing the total energy deposited (in MeV) per scintillator row, was plotted to better interpret the previous energy distributions. Figure 5.18 depicts the obtained projection.

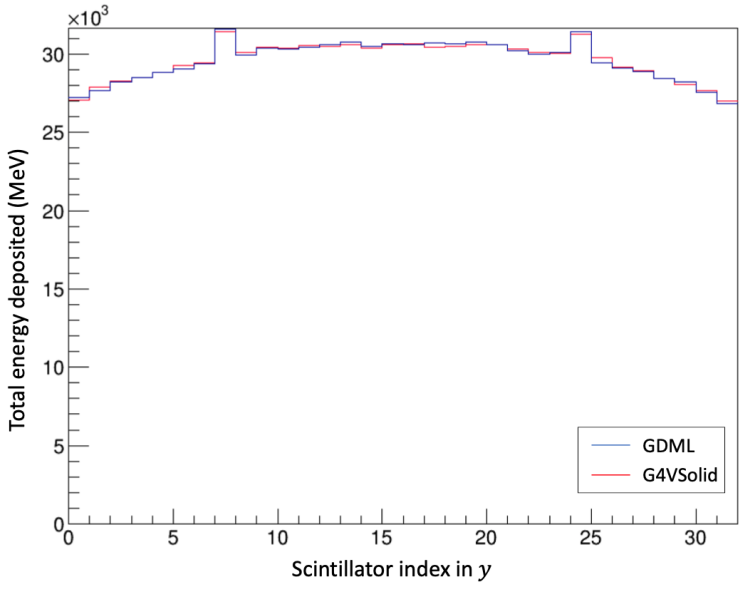

Figure 5.18: Energy profile for the GDML and G4VSolid approaches.

The GDML and G4VSolid approaches present essentially the same energy profile; the slight differences observed are due to statistical fluctuations. Two bins present a higher energy deposition, which is in agreement to the previous plots. This occurrence will be explained in section 5.4.3.

5.4.1.4 Simulation run time

Table 5.6 presents the simulation run time for both approaches.

	GDML	**G4VSolid**
Mean simulation time for 10^7 gamma pairs	22.32 min	18.68 min

Table 5.6: Simulation run time for the GDML and G4VSolid approaches.

Although the simulation run time was expected to be much longer for the GDML approach due to, as already mentioned, the higher level of detail of the geometry and the use of tessellated objects, the GDML approach is actually just about 15% slower than the G4VSolid approach.

5.4.2 Only scintillators enabled and complete system comparison

Once the G4VSolid approach was proven to be essentially the same as the GDML approach in terms of number of detected coincidences, total energy deposited and simulation run time, a comparison between the PET system with just the scintillators enabled and the PET system with all elements defined in the G4VSolid approach enabled was performed, to understand the potential differences in terms of the factors mentioned above. Figure 5.19 shows the geometries compared.

(a) Scintillators **(b)** G4VSolid approach

Figure 5.19: Detector geometries simulated with only the scintillators enabled and with all elements defined in the G4VSolid approach enabled. In the figures, the PMMA phantom with: (a) scintillators, (b) all elements defined with the G4VSolid approach enabled plus the scintillators. Figures not at scale (phantom and scintillators in both geometries are the same).

To clarify the elements enabled for the comparison, figure 5.20 shows the interior of the detector geometry represented in figure 5.19b without the enclosure.

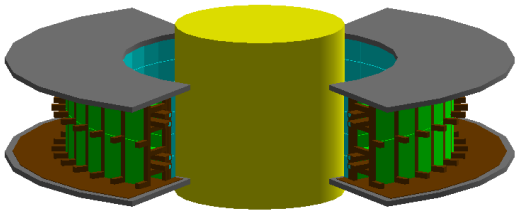

Figure 5.20: Simulated detector geometry without the enclosure.

5.4.2.1 Detected hits

Tables 5.7 and 5.8 present, respectively, the number of detected hits for the geometry with only the scintillators enabled and with all elements defined with the G4VSolid approach enabled.

Once again, from the total number of hits, the single hits and the multiple hits were discarded to obtain the total number of coincidences.

Scintillators				
	No. hits	**Single hits**	**Multiple hits**	**No. coincidences**
Seed 1	314031	286854	13606	13571
Seed 2	313251	285730	13775	13746
Seed 3	311980	284538	13735	13707
Sum	939262	857122	41116	41024

Table 5.7: Detected hits with only the scintillators enabled.

G4VSolid				
	No. hits	**Single hits**	**Multiple hits**	**No. coincidences**
Seed 1	308788	282138	13338	13312
Seed 2	308898	282305	13310	13283
Seed 3	308695	282234	13239	13222
Sum	926381	846677	39887	39817

Table 5.8: Detected hits with all elements defined with the G4VSolid approach enabled.

From the detected hits, it can be observed a small, but systematic decrease of (in absolute value) 1.37% in the number of hits, 1.22% in the number of single

hits, 2.99% in the number of multiple hits, and 2.94% in the number of coincidences between the geometry with only the scintillators enabled and all elements defined with the G4VSolid approach enabled. This systematic decrease will further be explained in subsection 5.4.2.3.

5.4.2.2 Coincidences

Table 5.9 presents the number of coincidences and respective standard uncertainties for both detector geometries simulated.

	Scintillators		**G4VSolid**	
	No. coincidences	σ	**No. coincidences**	σ
Sum	41024	350	39817	345

Table 5.9: Total number of coincidences and respective standard uncertainties for the geometry with only the scintillators enabled and all elements defined with the G4VSolid approach enabled.

The difference between the total number of coincidences ($\Delta_{Coincidences}$=41024-39817=1207) is within four σ and is equal to 2.94% in absolute value. Once again, this difference will be explained in subsection 5.4.2.3.

5.4.2.3 Decrease in the number of detected hits and coincidences

One possible explanation for the systematic decrease in the number of detected hits observed from table 5.7 to table 5.8 and in the total number of coincidences in table 5.9 could be the presence of the plastic front window of the PET enclosure, that could be acting as a barrier: despite being only 1 mm thick, if the gamma ray hits the material obliquely, there is a higher probability of being absorbed by photoelectric effect or suffer Compton scattering and, consequently, reduce the total number of detected hits and coincidences.

If that would be the case, and considering the decrease in absolute value of 1.2% in the number of single hits observed from the geometry with only the scintillators enabled to the geometry with all elements defined with the G4VSolid approach enabled (tables 5.8 and 5.9), that would mean that the introduction of the plastic front window in the geometry would be responsible for a decrease of approximately 1.2% in the number of single hits, as a consequence of the absorption or scatter of the gamma ray by that plastic front window.

Consequently, since one coincidence implies the detection of two gamma rays, and given that the decrease in the detection of one single gamma ray would be of

approximately 1.2%, a proportional double decrease of 2.4% in the number of coincidences would be observed. The probability of both gamma rays of a coincidence being discarded by the window would be, in principle, low, but one of the gamma rays being discarded is what it takes to discard the coincidence, hence the double reduction. Figure 5.21 depicts the effect of the plastic front window in the reduction of single hits and total number of coincidences explained above.

To check if the plastic front window could be the reason for the observed reduction in the total number of detected hits and coincidences, another simulation, this time without the plastic entrance window, was performed (figure 5.22).

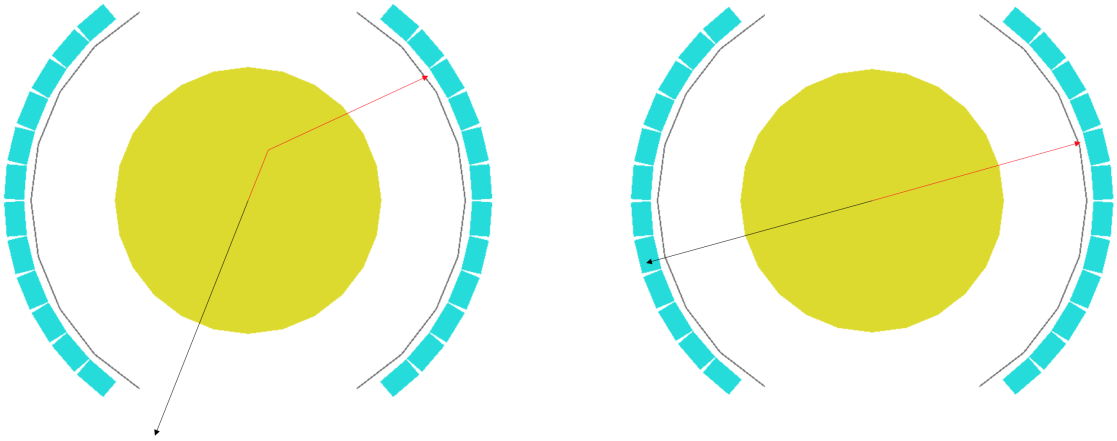

(a) Single hit **(b)** Coincidence

Figure 5.21: Effect of the PET enclosure's plastic entrance window on the reduction of single hits and total number of coincidences. On the left, only one gamma ray is absorbed, discarding what would have been a single hit; on the right, one gamma ray of what would be a coincidence is absorbed, resulting in the discard of that coincidence.

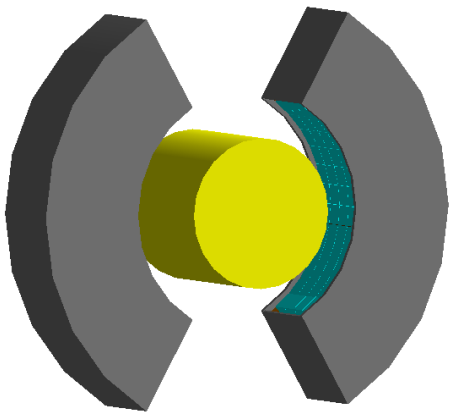

Figure 5.22: Detector geometry without the PET enclosure's plastic entrance window used to simulate the effect of the window in the number of single hits and coincidences.

The results of the simulation with the detector geometry depicted in figure 5.22

are presented in table 5.10.

G4VSolid (no entrance window)				
	No. hits	**Single hits**	**Multiple hits**	**No. coincidences**
Seed 1	312597	285024	13801	13772
Seed 2	312581	285605	13504	13472
Seed 3	313783	286522	13641	13620
Sum	938961	857151	40946	40864

Table 5.10: Detected hits with all elements defined with the G4VSolid approach except for the PET enclosure's plastic entrance window enabled.

From the values presented in tables 5.7 and 5.10 it can be concluded that, in fact, it is the plastic entrance window of the PET enclosure that causes the decrease in the number of single hits and coincidences, since this simulation showed essentially no difference between those numbers (the difference in absolute value is of only 0.03% in the total number of hits, 0.003% in the number of single hits, 0.41% in the number of multiple hits and 0.39% in the total number of coincidences); the slightly variations observed are due to statistical fluctuations.

5.4.2.4 Energy deposition

Figure 5.23 depicts the total energy deposition (in MeV) per scintillator for both PET detector geometries from figure 5.19.

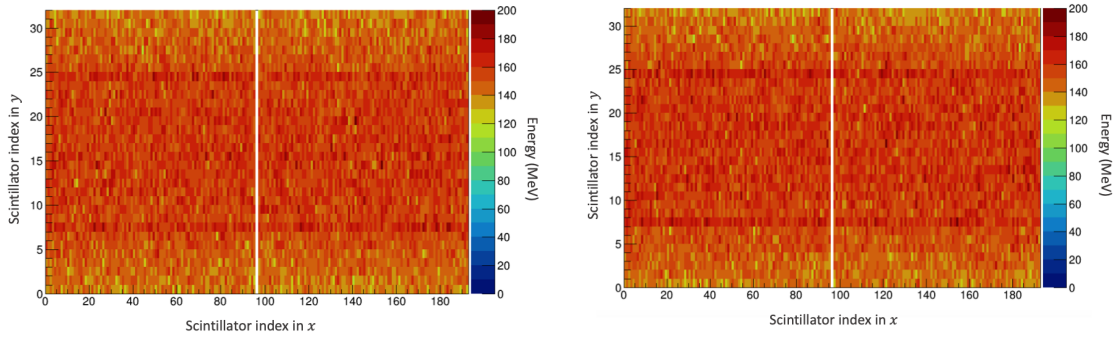

(a) Scintillators **(b)** G4VSolid

Figure 5.23: Total energy deposited (in MeV) per scintillator in the geometry with only the scintillators enabled and all elements defined with the G4VSolid approach enabled.

Similarly to the previous comparison, between the GDML and G4VSolids approaches, from figure 5.23, a symmetry between both PET detector heads, a higher energy deposition in the middle scintillators and two scintillator rows that present

a higher energy deposition than their neighbors can be observed, and the energy profile was plotted, as it can be observed in figure 5.24.

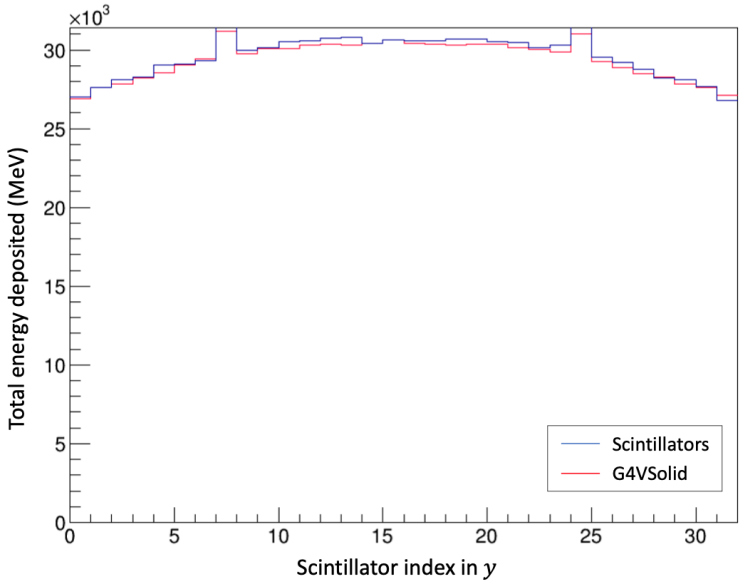

Figure 5.24: Energy profile for the geometry with only the scintillators enabled and all elements defined with the G4VSolid approach enabled.

From the plot of the energy profile obtained, it can be concluded, in accordance to the systematic decrease observed in the number of detected hits, that the energy deposited per scintillator row in the geometry with all elements defined with the G4VSolid approach enabled is slightly bellow the geometry with just the scintillators enabled.

Also similarly to the previous comparison, two bins present a higher energy deposition, which will be, as mentioned, further explained in section 5.4.3.

5.4.2.5 Energy deposition - ribs effect

Another important factor to evaluate in this particular comparison was if the presence of the copper ribs would influence the energy deposition in the scintillators. For that, the total energy deposited per scintillator in relation to their distance from the ribs was plotted (figure 5.26), with 1 being the scintillators immediately near the ribs, and 4 being the inner scintillators, further from the ribs (figure 5.25).

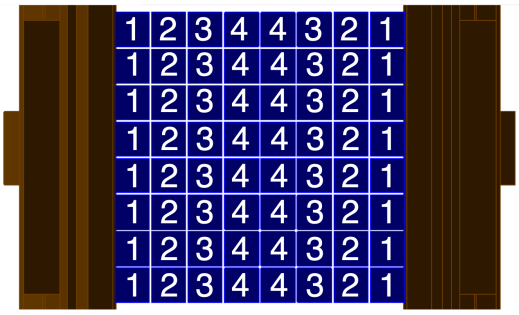

Figure 5.25: Scintillators numbering to investigate the ribs effect in the energy deposition. In brown, a portion of the ribs; in dark blue, an 8 by 8 array of scintillators.

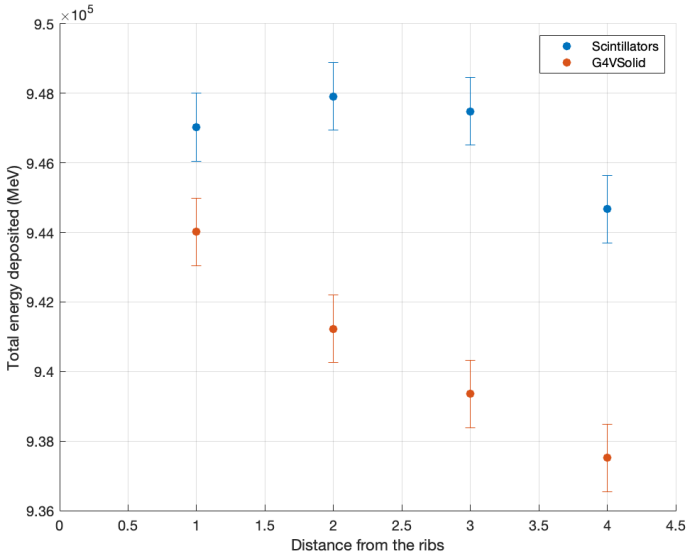

Figure 5.26: Energy deposition in the scintillators nearest and furthest from the copper ribs for the geometry with only the scintillators enabled and all elements defined with the G4VSolid approach enabled.

In the geometry with all elements defined in the G4VSolid approach enabled, a slightly decrease of the energy deposited can be observed as the scintillators are further away from the ribs, which can be explained by the scatter of the gammas in the ribs, that are made of copper, that hit the immediately near scintillators, increasing the energy deposited in relation to the inner ones that do not feel this effect. However, the difference between the most outer and the most inner scintillators is just 0.60% in absolute value, which shows this effect is weak.

In the geometry with just the scintillators enabled, the fluctuations in the energy deposited in the scintillators appear to be statistical.

5.4.2.6 Simulation run time

Table 5.11 presents the simulation run time for both detector geometries simulated.

	Scintillators	**G4VSolid**
Mean simulation time for 10^7 gamma pairs	14.52 min	18.51 min

Table 5.11: Simulation run time for the geometry with only the scintillators enabled and all elements defined with the G4VSolid approach enabled.

The simulation run time was only 28% longer in the case of the geometry with all elements defined with the G4VSolid approach enabled, meaning the simulation run time was not significantly slower compared to the geometry with only the scintillators enabled.

5.4.3 Energy deposition in the scintillators

As already mentioned, figures 5.16, 5.18, 5.23 and 5.24 suggest a higher energy deposition in some scintillator rows when compared to their neighboring scintillators.

One possible explanation could be the presence of the detector elements behind those scintillators, but that possibility was discarded when the same rows presented a higher energy deposition for the geometry with just the scintillators enabled (figure 5.23a).

Understanding what was happening to cause that higher energy deposition was crucial, since it could be generated by a bug in the simulation code. Hence, to try to find out if there was a physics explanation to what was happening, the source position within the PMMA phantom was changed: first, only 20 mm bellow the center of the PET system; then, to the very bottom and top of the PET system.

From the results shown in figure 5.27, it can be concluded that the scintillators that were immediately before or after (according to the source emission position) the gaps between the 8 by 8 arrays were the ones that presented a higher energy deposition than their neighbors.

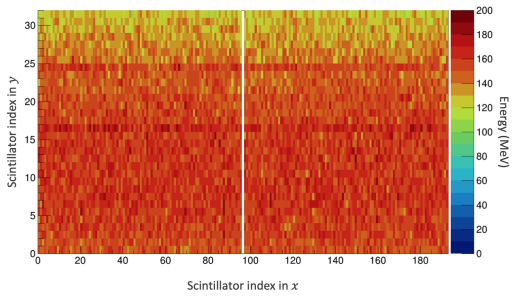

(a) 20 mm bellow the center of the system

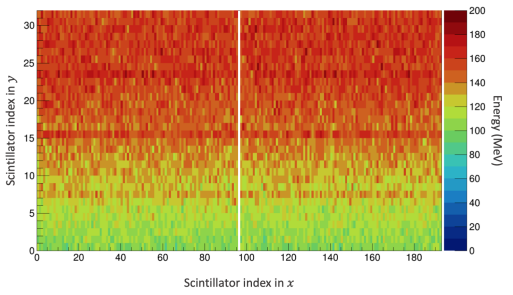

(b) Top of the system

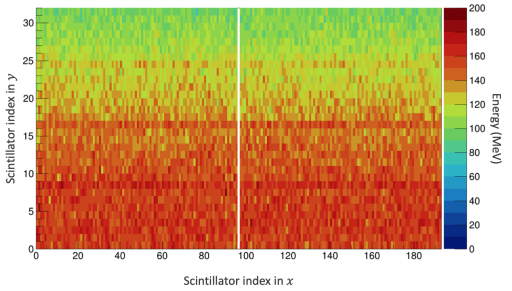

(c) Bottom of the system

Figure 5.27: Energy deposition distributions after changing the source emission position.

For that reason, it could be concluded that there was a reasonable explanation for that higher energy deposition, and it was not a bug that was causing it: such scintillators are more exposed to the gamma rays, as depicted in figure 5.28, presenting, consequently, a higher energy deposition than the ones that are not next to the gaps between rows, according to the direction of the gammas emitted.

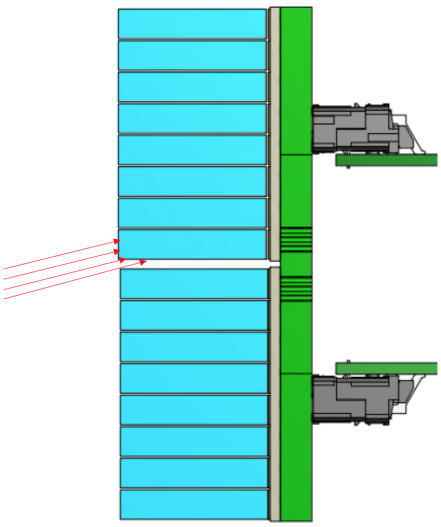

Figure 5.28: Illustration of the gamma rays incidence on the scintillators in between rows (lateral view).

5.4.4 Intermediate conclusions

Concerning the comparison between the GDML and G4VSolid approaches, the results in terms of detected hits, number of coincidences, energy deposition, and simulation run time were essentially the same, meaning the approximations made in the G4VSolid approach were viable.

It is important to mention, though, that the fact that the simulated geometries compared did not represent the totality of the PET detector elements, and the fact that the GDML file did not contain the information on the materials that will be used in the real prototype are inconveniences. For a more reliable comparison, it would be important that the GDML file contained the definition of the complete PET system, as well as of the respective compositions, in order to validate the fully PET detector developed in the G4VSolid approach and respective approximations.

However, given that the support structures were the detector element most subject to geometrical approximations in the G4VSolid approach, and for that reason, the components of major concern, the comparison with the GDML approach is already enough to approve, considering the obtained results, the geometry developed with Geant4's solids.

In what concerns the comparison between the geometry with only the scintillators enabled and the complete system developed in the G4VSolid approach, the only noticeable effect arises in the number of detected hits and coincidences, due to the entrance window of the PET system enclosure.

As a consequence of the two performed comparisons, it makes sense that the final decision is to use the complete system developed in the G4VSolid approach (i.e., with all elements enabled) in the simulation framework to perform simulations involving the PET system prototype.

6

Simulation Customization

6.1 Production cuts

Production cuts (or cut-off values) are range thresholds specified for secondary particles (gammas, electrons and positrons). These range thresholds establish that secondary particles are not produced if they are unable to travel at least the range defined by the cut-off value. The range thresholds are converted to energy thresholds and, if the particle is not produced, its kinetic energy is deposited locally [90, 91]. These production cut-off values are particle dependent (e.g., the range of a 10 keV photon in silicon is different from the range of a 10 keV electron in silicon), and material dependent (e.g., the range of a 10 keV photon in silicon is different from the range of a 10 keV photon in aluminum) [92].

The thresholds set for secondary gammas are applied to *bremsstrahlung* and Compton scattering processes; for secondary electrons are applied in ionization, pair production, photoelectric effect and Compton scattering; for secondary positrons are only applied to pair production, hence, are not relevant for the TPPT simulations' purposes [90].

In MC simulations there must be a compromise between the accuracy of the simulation (processes of interest cannot be discarded due to the cut-offs) and the simulation performance in terms of time, because in most cases, the optimization of one of these parameters influences negatively the other [92].

In order to optimize the run time of the simulation developed for the TPPT consortium, several cut-off values were assigned to two regions: one region containing all the scintillators and respective teflon encapsulation, and another region containing the phantom. The approach adopted to obtain the optimal cut-off values was to start with very small cut-off values assigned to both regions, and then to increase them and to compare the simulation run time and the energy deposition in

the scintillators. The energy deposition was analyzed with the simulator's deposition statistics operation mode, described in chapter 4.

First, all cut-off values were set to 1 μm, both for the scintillator and phantom regions, for secondary gammas, electrons and positrons. The number of gammas (from a total of 10 million of gammas generated) calculated from the deposition statistics mode can be seen in table 6.1, that presents the number of gammas that do not interact with any scintillator, and that interact with only one, two, three, four, or five or more scintillators, as well as the respective standard uncertainties (σ), given by the square root of the number of gammas, and the simulation run time.

Cut-off	**1 μm**	
	No. γ	σ
None	8469500	2910
Single	1169200	1081
Two	314700	561
Three	42300	206
Four	4000	63
Five+	300	17
Time	1880.78 s	

Table 6.1: Deposition statistics for all cut-off values set to 1 μm for both regions.

Then, keeping the cut-off values equal to 1 μm for the phantom region, the cut-off values for the scintillator region were increased: first to 0.1 mm, and then to 1.5 mm (10% of the scintillator crystals' width). The results are presented in table 6.2.

Cut-off	**0.1 mm**		**1.5 mm**	
	No. γ	σ	**No. γ**	σ
None	8470600	2910	8468500	2910
Single	1168600	1081	1297400	1139
Two	314200	561	207100	455
Three	42300	206	25100	158
Four	4000	63	1800	42
Five+	300	17	100	10
Time	1681.93 s		1647.01 s	

Table 6.2: Deposition statistics for all cut-off values set to 0.1 mm and 1.5 mm for the scintillator region. Phantom region with all cut-offs set to 1 μm.

Comparing the results from tables 6.1 and 6.2, when the scintillator cut-off values were set to 0.1 mm, there were no significant differences in the number of photons interacting with the scintillators, and there was a reduction of approximately 200 seconds in the simulation run time.

However, when the scintillator cut-off values were set to 1.5 mm, significant differences could be observed in the number of photons interacting with a single, two, three, four, or five or more scintillators. This is most probably due to the characteristic X-rays from the lutetium-176 present in the LYSO crystals that are not produced once the secondary gammas cut-off is set to 1.5 mm. To understand if this was the reason, the cut-off was set to 0.1 mm for the gammas and 1 m for the electrons and positrons. The results are presented in table 6.3.

Cut-off	**0.1 mm γ and 1 m e^-/e^+**	
	No. γ	σ
None	8471100	2911
Single	1168600	1081
Two	314000	560
Three	42000	205
Four	4000	63
Five+	300	17
Time	1656.11 s	

Table 6.3: Deposition statistics for the cut-off values set to 0.1 mm for photons and 1 m for electrons and positrons for the scintillator region. Phantom region with all cut-offs set to 1 μm.

The results presented in table 6.3 suggest that the significant differences obtained for the cut-offs for the scintillator region set to 1.5 mm are indeed due to lutetium-176 characteristic X-rays. Calculating the energy corresponding to the set range with Geant4, a range of 0.1 mm in LYSO corresponds to a gamma energy of approximately 15 keV, and a range of 1.5 mm to approximately 85 keV. These results are consistent with the k-edge energy for lutetium, which is equal to approximately 63 keV [93]: with a range cut of 1.5 mm, the characteristic X-rays are not produced anymore, hence the significant differences observed from setting the production cuts from 0.1 mm to 1.5 mm.

Considering that the simulation run time was the same for the cut-off values set to 0.1 mm and 1.5 mm for the scintillator region, meaning that no further optimization would be achieved from increasing the 0.1 mm cut-off, it could be concluded that the optimal cut-off values for gammas, electrons and positrons for

the scintillator region should be set to 0.1 mm.

Keeping the scintillator cut-off values equal to 0.1 mm, the phantom cut-off values were set to 0.1 mm, 1.5 mm, 10 mm, and to an extreme value of 1 m, to understand if differences in the energy deposited would be observed. The results are presented in table 6.4.

Cut-off	**0.1 mm**		**1.5 mm**		**10 mm**		**1 m**	
	No. γ	σ	**No.** γ	σ	**No.** γ	σ	**No.** γ	σ
None	8469700	2910	8470100	2910	8469700	2910	8472500	2911
Single	1169500	1081	1169200	1081	1169500	1081	1167000	1080
Two	314300	561	314300	561	314300	561	314000	560
Three	42200	205	42100	205	42200	205	42200	205
Four	4000	63	4000	63	4000	63	4000	63
Five+	300	17	300	17	300	17	300	17
Time	605.49 s		616.72 s		620.33 s		629.52 s	

Table 6.4: Deposition statistics for all cut-off values set to 0.1 mm, 1.5 mm and 10 mm for the phantom region. Scintillators' region with all cut-offs set to 1 mm.

No significant differences were observed in the deposition statistics when comparing the results presented in table 6.4 to the results presented in table 6.1. Besides, there is a reduction in the simulation run time for larger cut-offs of approximately 1076 seconds (Δt=1681.93-605.49), i.e., approximately 18 minutes.

No further optimization could be achieved from setting the phantom cut-off values to higher values: no significant differences in the deposition statistics from setting the phantom cut-offs from 0.1 mm to 1 m, and no improvement on the simulation run time were observed.

Therefore, the compromise between the simulation accuracy and performance in terms of run time is obtained by setting the cut-off values for gammas, electrons and positrons in both regions (scintillators and phantom) to 0.1 mm.

6.2 Production of positron-emitting species

As mentioned, proton therapy range verification is performed by comparing the measured activity distribution of positron-emitting species induced by the irradiation of a patient with a proton beam with the activity distribution predicted by simulations based on the treatment plan [94]. In addition, PET images may be compared between different irradiation fractions in order to provide feedback on the course of the treatment [12].

The accuracy of the predicted distributions depends on the accuracy of the computational models implemented in MC codes that describe the interactions of protons with matter and the consequent production of positron-emitting species and other secondary particles [94].

The predicted proton-induced activity depends, in particular, on the proton fluence and energy distribution in a certain volume (i.e., voxel), which, in turn, depends on the tissue density, on the material composition, and on the nuclear reaction cross-sections. Therefore, the accuracy of the simulated distributions strongly depends on the accuracy of the cross-sectional data for positron-emitting production available, and implementing accurate cross-sectional data to simulate activity distributions suitable for proton therapy range verification is crucial [62].

The internal models used by MC codes that produce positron-emitting yields have been proved to be significantly different from the ones obtained using experimental cross-sectional data. Because of this, the use of cross-sectional data validated experimentally is currently recommended, instead of the nuclear internal models implemented in MC codes [94]. There is not, nonetheless, any well-established theoretical models to predict these nuclear reactions, and, therefore, experimental data is usually employed to predict these distributions. Yet, the experimental data currently available is also insufficient to validate these interaction models [62, 94]. Experimental and theoretical cross-sectional values are available, for instance, in the Experimental Nuclear Reaction Data (EXFOR) library and on the ICRU report 63, respectively; there are, nonetheless, significant differences between the several data sets available [62].

Thus, in order to obtain experimental cross-sectional data to be used in the TPPT consortium's simulation, a data set with the cross-sectional information (cross-sections in milibarn versus the energy of the protons in MeV) had to be created. For that, a Heidelberg Ion-Beam Therapy Center (HIT) group (Germany) was contacted, considering an experimental work reported on a 2013 article [95].

The article presents an experimental strategy carried out by the HIT group to optimize their MC modelling of positron-emitting species production induced by the irradiation with protons, motivated by: the clinical implementation of a treatment verification system based on offline PET/CT imaging; the uncertainties arising from the use of different MC codes; the lack of information on reliable cross-sections data for the relevant proton therapy energy range - although numerous experimental cross-sections data are available in the literature, the several data sets differ in such a way that result into significant uncertainties in the prediction of the positron-emitting species yield [95].

Furthermore, besides being affected by the cross-sectional data implemented, the predicted activity distributions are also affected by the time structure of the proton irradiation technique and by the imaging acquisition, that depends on the PET detector geometry (for instance, if it is a partial ring or a full ring scanner), hence the importance of verifying experimentally the simulated positron-emitting yields before any clinical application [95].

As a consequence, the HIT group performed an experimental approach by tuning the MC modelling to the facility-specific (i.e.,considering the irradiation and imaging techniques performed in the HIT) β^+ activity contributions of individual radionuclides. The experimental study implied the irradiation of five phantoms of different materials of known chemical composition with a monoenergetic proton pencil beam at various energies and the consequent acquisition of the induced β^+ activity with a commercial full-ring PET/CT scanner. The phantom materials were chosen given preference to simple elemental compositions, to be possible to directly observe the corresponding production channel; in phantoms with a more complex composition (which activity is the sum of the several radionuclide contributions), the activity contribution of the different radionuclides was separated in the image reconstruction phase, by considering the respective decay times [95].

Once the relevant material properties are known, it is possible to tune the cross-sectional data in a way that the resulting positron emitter yield corresponds to the activity observed experimentally. This tuning was done by the group the following way: the simulated activity depth distributions for a single radionuclide were compared to the measured activity distributions of each individual radionuclide (which is possible through the analysis of the reconstructed PET images over time), and the observed differences were iteratively minimized by adjusting the cross-section data set, re-simulating the experiment, and comparing to the measurement all over again [95].

The HIT group sent their cross-sections information on the condition of not disclosing it, since the TPPT's simulation framework will be open source (available on Github), limiting its use for internal testing purposes only. Hence, the cross-sections information to be used for the TPPT simulation was extracted directly from the tuned cross-sections data reported in the mentioned article, and the resulting activity profiles were compared with the activity profiles obtained from the data sent privately by the group for validation purposes.

According to the chemical composition of human tissue, and considering that the PET image acquisition is offline in the HIT facility, the HIT group studied six cross-section channels fundamental for their proton treatment verification system, which information was provided in the shared file: ^{12}C(p,pn)^{11}C, ^{16}O(p,3p3n)^{11}C, ^{16}O(p,pn)^{15}O, ^{16}O(p,2p2n)^{13}N, ^{40}Ca(p,2pn)^{38}K, and ^{31}P(p,pn)^{30}P, with half-lives of 1222.8 s for ^{11}C, 122.4 s for ^{15}O, 597.6 s for ^{13}N, 456.0 s for ^{38}K and 150.0 s for ^{30}P.

6.2.1 Data extraction

To extract the data of the tuned cross-sections from the article, an online tool called WebPlotDigitizer was used. This tool allows an automatic or manual extraction of the data, but since the tuned graphs depicted in the article were sometimes hidden behind other graphs, a manual extraction was preferred.

For the manual extraction, it is only necessary to select two points on each axis and to indicate their coordinates; and then it is possible to mark the points in the graphs to obtain their respective coordinates (figure 6.1).

Each graph in the article contains more than one plot: the tuned experimental values - the ones used to extract the data for the TPPT simulation - are labelled in red. These values are compared to a compilation by Parodi *et al.* [96] (in blue) and theoretical values from ICRU or values from Sisterson *et al.* [97] (in yellow), and to experimental data from Iljinov *et al.* [98] (in green). The red plot was used to extract the data for all production channels cross-sections, except for the ^{40}Ca(p,2pn)^{38}K production channel, obtained from the blue plot, the only available.

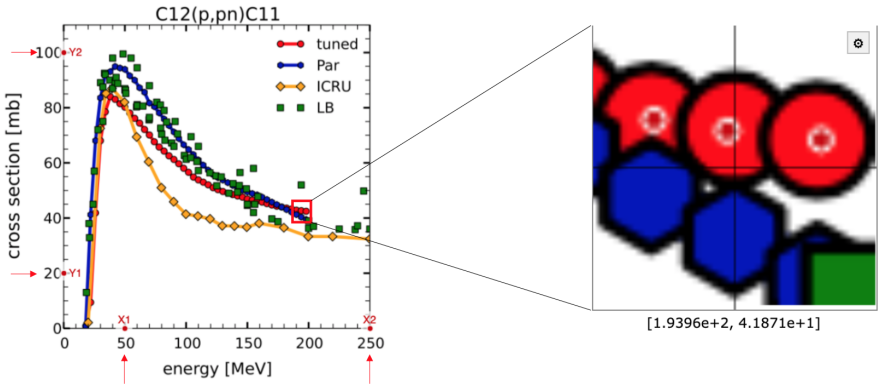

Figure 6.1: WebPlotDigitizer manual data extraction.

As shown in figure 6.1 for the $^{12}C(p,pn)^{11}C$ reaction channel, the WebPlotDigitizer was used to extract the cross-sections data from all other channel reactions, except for the $^{31}P(p,pn)^{30}P$ one: despite the information about this reaction being present in the file provided by the HIT group, there was no information about it on the article.

The only difficulty in the data extraction with WebPlotDigitizer occurred for the $^{16}O(p,2p2n)^{13}N$ reaction channel. As it can be seen in figure 6.2, it comes to a point where the graph plot lines are indistinguishable (they almost overlap) and, because of that, only the points that were undoubtedly perceived were signalled.

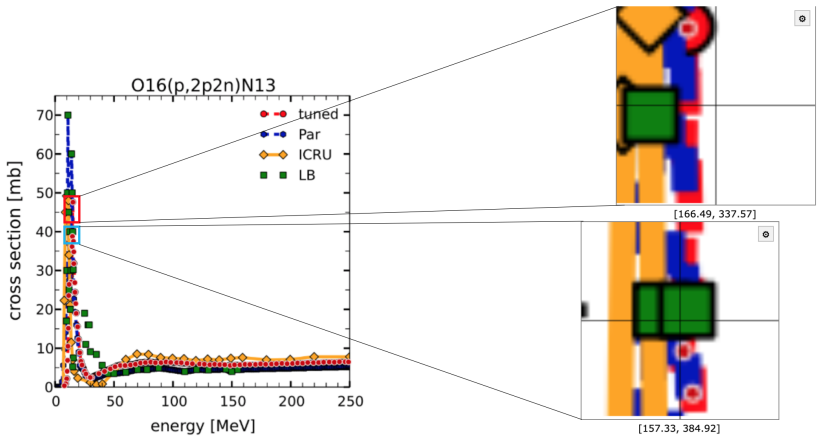

Figure 6.2: Points uncertainty in the WebPlotDigitizer data extraction for the $^{16}O(p,2p2n)^{13}N$ reaction channel.

Additionally, the shape of the blue plot, that presents two peaks, could be suggestive of the existence of a second peak, predicted near the region signalled in figure 6.3, but considering there was not enough visibility to mark more points, it was assumed that there was only one peak.

Even though the extraction of the $^{16}O(p,2p2n)^{13}N$ reaction channel was not straightforward, the activity profiles resulting from the cross-sectional data extracted for the TPPT and provided by the HIT group file were later compared, to conclude if the data extraction was reliable or not.

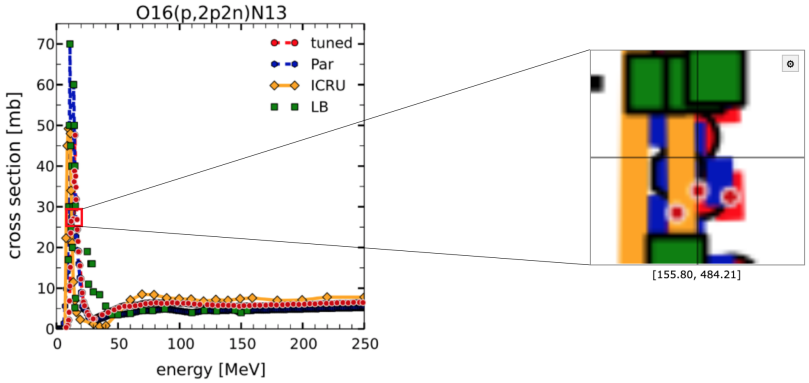

Figure 6.3: Peak uncertainty in the WebPlotDigitizer data extraction for the $^{16}O(p,2p2n)^{13}N$ reaction channel.

Figure 6.4 shows the graphs of the five reaction channels reported in the article.

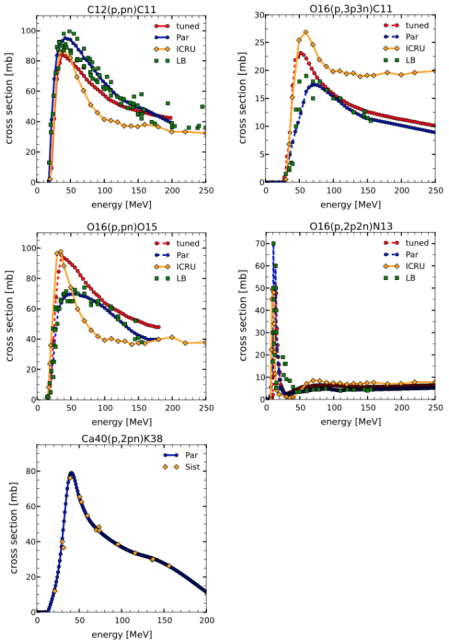

Figure 6.4: Comparison of the graphs acquired by the HIT group in their article (on the left) and the graphs plotted with the information extracted from the same article using the online tool WebPlotDigitizer (on the right).

As already mentioned, the $^{31}P(p,pn)^{30}P$ reaction channel information was not presented in the article. To extract the data for this reaction channel, the EXFOR

database was consulted to find all the cross-sections data for a target of ^{31}P hit with protons.

Two data sets that resulted in the production of ^{30}P were found. The reactions found were both for ^{31}P(p,x)^{30}P ("x" stands for process unspecified), instead of ^{31}P(p,pn)^{30}P, which is even better for this purpose, because it comprises all reactions that lead to the production of ^{30}P as a consequence of a ^{31}P target being hit with a proton.

One of the data sets contained the coordinates of 11 points, and the other of only 1 (figure 6.5), so, for obvious reasons, the one with 11 points was chosen (table 6.5) to plot the cross-sectional data for the ^{31}P(p,pn)^{30}P reaction channel.

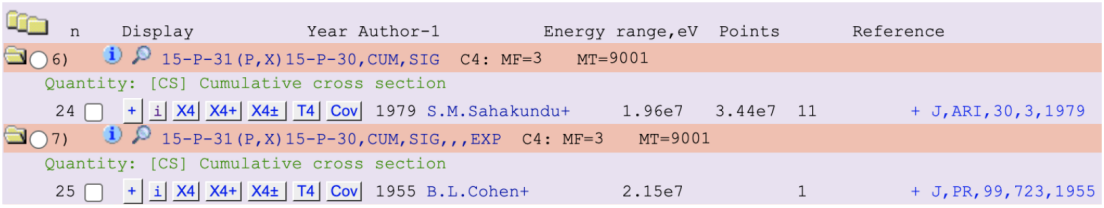

Figure 6.5: Result of the EXFOR search for the ^{31}P(p,x)^{30}P reaction channel.

Energy (MeV)	Cross-section (mb)
19.6	10.5
20.3	50.0
20.9	70.0
22.0	80.0
23.0	180.0
23.6	200.0
25.0	240.0
30.0	141.0
30.5	132.0
34.0	51.0
34.4	46.0

Table 6.5: Cross-sections data for the ^{31}P(p,pn)^{30}P production channel obtained from the EXFOR library [99].

Finally, the data for the six cross-sections channels contained in the file provided by the HIT group was gathered, and the obtained plots are depicted in figure 6.6.

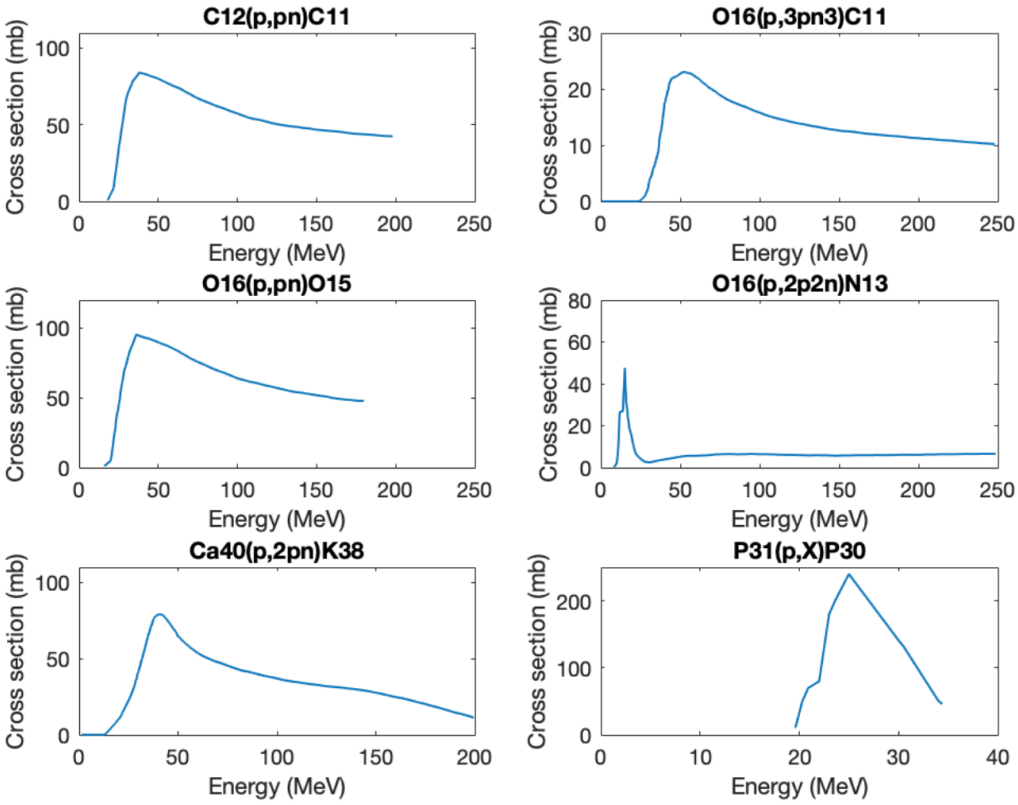

Figure 6.6: Plots of the cross-sections versus the proton energy for the six channel reactions provided by the HIT group.

For the last reaction channel, ^{31}P(p,pn)^{30}P, the proton energy range is relatively small (from about 20 MeV to 34 MeV) when compared to the energy range information available for the other reactions.

As mentioned, though, a comparison of the activity profiles resulting from the data set provided by the HIT group and from the data set extracted for the TPPT consortium will allow to take conclusions regarding the reliability of the data gathered.

The information available for the ^{31}P(p,pn)^{30}P production channel is, nonetheless, insufficient, since the proton beams that will be used for the TPPT consortium's purposes will have energies considerably higher than 34 Mev (>100 MeV). Therefore, the strategy adopted to use this particular cross-sectional data set is to consider the cross-sections equal to 0 mb bellow the proton energy of 19.6 MeV, and to consider a plateau (cross-sections equal to 46 mb) above the proton energy of 34.4 MeV.

6.2.2 Activity profiles comparison

The HIT group compared the measured activity depth profiles along the beam direction to the simulated ones. For that, the group compared the activity on start - the activity distribution after the phantom irradiation time plus a delay time between the end of the irradiation and the start of the PET measurement (A_0) - and the mean activity - the average activity during the period the scanner is measuring (<A>) [95].

Similarly, the corresponding activity on start and mean activity quantities simulated with the data set extracted for the TPPT consortium were plotted, using the same time parameters as in the article, and compared to the activity profiles presented in the article.

Hence, once all cross-sections information was gathered, the activity profiles resulting from the data extracted for the TPPT and from the file provided by the HIT group were plotted, in order to conclude if the information gathered for the TPPT consortium was reliable or not.

The result of the MC simulation consists on a spatial distribution of positron-emitter production yields per beam particle, separately for individual radionuclides, and the resulting activity distribution is calculated considering the total number of beam particles, the time structure of the irradiation and the time of the PET acquisition [95].

For the activity profile plots, it was simulated a proton beam of 10^5 protons of energy 125.67 MeV (one of the energies used in the HIT experiment) impinging on phantoms. Several phantoms (with the same dimensions, $9 \times 9 \times 30$ cm^3) of different material compositions were used in the simulation, to verify the activity profiles for all the production channels:

- A PMMA phantom - due to the material composition, the positron-emitting species produced are the ones resulting from the ^{12}C(p,pn)^{11}C, ^{16}O(p,3p3n)^{11}C, ^{16}O(p,pn)^{15}O and ^{16}O(p,2p2n)^{13}N production channels;
- A calcium phantom - the positron-emitting species produced are the ones resulting from the ^{40}Ca(p,2pn)^{38}K production channel;
- A phosphorus phantom - the positron-emitting species produced are the ones resulting from the ^{31}P(p,pn)^{30}P production channel.

Figures 6.7, 6.8 and 6.9 depict the activity profiles obtained for the PMMA, calcium, and phosphorus phantoms, respectively. It is important to mention that the activity units are expressed in arbitrary units, since not all conditions of the experimental setup used by the HIT group were known (in particular, there was no data on the width and the divergence of the pencil beam used, and also no data on the activity averaging region), and therefore, the comparison of absolute activity values is not possible.

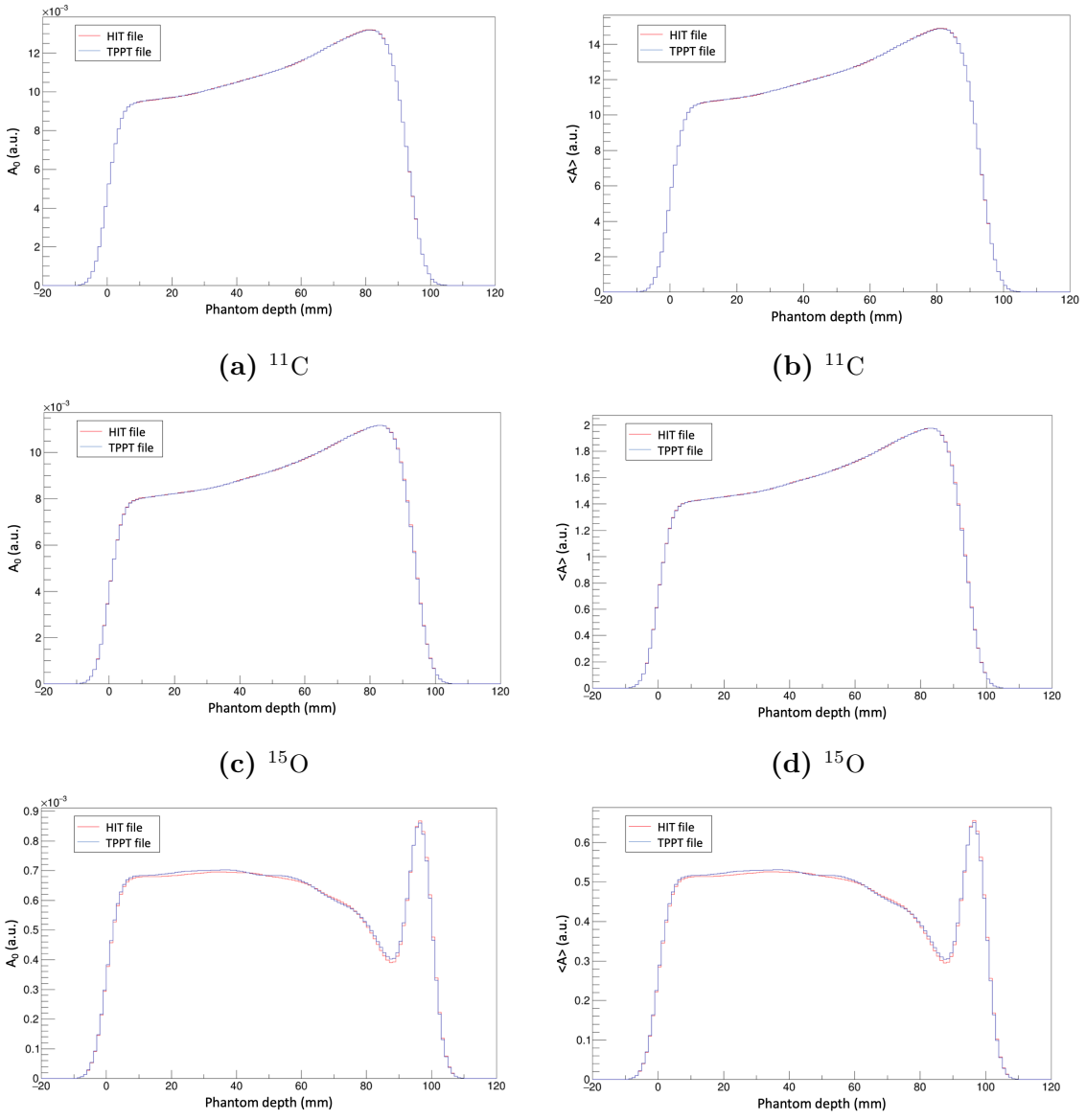

(a) ^{11}C **(b)** ^{11}C

(c) ^{15}O **(d)** ^{15}O

(e) ^{13}N **(f)** ^{13}N

Figure 6.7: Activity profiles for the PMMA phantom. Activities on start on the left, mean activities on the right.

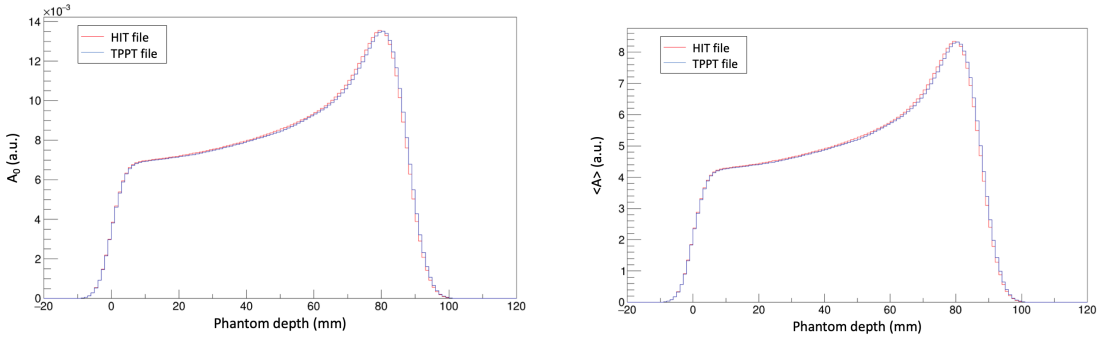

(a) ^{38}K **(b)** ^{38}K

Figure 6.8: Activity profiles for the calcium phantom. Activities on start on the left, mean activities on the right.

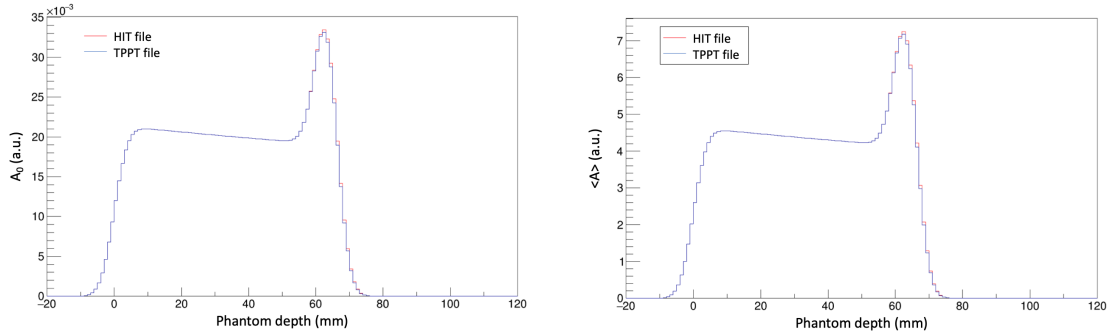

(a) ^{30}P **(b)** ^{30}P

Figure 6.9: Activity profiles for the phosphorus phantom. Activities on start on the left, mean activities on the right.

As it can be concluded from the previous graphs, both the activity profiles for the activity on start and for the mean activity are very similar for the three phantoms. The activity resulting from the ^{13}N radionuclide is the one that shows a bigger difference on the activity profiles, which was expected, due to the difficulties faced extracting the data for that reaction channel, but despite that, they are still very similar. Also, the activity resulting from the ^{30}P radionuclide, which cross-sectional information was taken from the EXFOR database, presents an activity profile that is essentially the same as the one obtained by the file provided by the HIT group, confirming the cross-sectional information is reliable.

To conclude, there was a good match between the activity profiles obtained both from the file provided by the HIT group and from the file created for the TPPT consortium, and, therefore, the file created was ready to be used in the simulation framework.

7

Conclusions

The TPPT consortium is developing a TOF-PET system prototype for proton therapy range verification that, for being an in-beam system, presents the advantages of reducing the severity of the biological washout effect, of avoiding the patient displacement, and of acquiring a higher statistics PET image. A framework for Monte Carlo simulations of the operation of the designed TOF-PET prototype was developed in Geant4.

In this Master's project, the PET detector prototype geometry and materials were defined in Geant4. The geometry was defined using Geant4's solids (G4VSolid approach) and the detector components' dimensions and positioning were verified and compared with the prototype design.

The detector defined in the G4VSolid approach was then compared in terms of detection efficiency with the detector defined by another group in a GDML (Geometry Description Markup Language) approach, used to translate Computer-Aided Design (CAD) geometries to Geant4. The GDML approach defined only a part of the PET system, and the complete detector was never fully developed in this approach. Besides that, this approach did not contain any information on the detector materials. Nevertheless, by comparing the same detector geometries with both definitions, the effect of the detector components on the detection efficiency was small, no matter the chosen approach.

Furthermore, for the G4VSolid approach, the effect of the complete PET detector components on the detection efficiency was analyzed. The only noticeable difference arises from the PET enclosure, that causes a decrease of approximately 3% in the total number of detected coincidences.

With this work, the simulation's optimal production cut values were also determined. The cut-off values for secondary gammas, electrons ans positrons should be set to 0.1 mm for both the scintillators' and phantom regions, as these are the

optimal parameters to speed up the simulation run time without compromising its accuracy.

Finally, it was also possible to extract data on the cross-sectional information (cross-sections versus proton energy) for the production of proton-induced positron-emitting species. Given that the simulation developed for the TPPT consortium is an open source code, these data was extracted from a published work by the Heidelberg Ion-Beam Therapy Center (HIT), in Germany, and from the EXFOR (Experimental Nuclear Reaction Data) library. The differences between the activity distributions resulting from the extracted data and from the data provided privately by the HIT group were negligible, hence validating the extracted data. For that reason, the data set is currently used in the simulation.

Future Work

The TOF-PET system prototype designed by the TPPT consortium is an in-beam system, contrary to the offline PET system that exists in the Heidelberg Ion-Beam Therapy Center. Therefore, one important continuation for this project would be to acquire information on other positron-emitting species produced as a result of the patient's irradiation, and which activity would be acquired during an in-beam acquisition, other than the ones presented in chapter 6. Among these positron-emitting species are the ones that present faster decay times, such as nitrogen-12 (^{12}N, $t_{1/2} \approx 12.51$ ms), calcium-39 (^{39}Ca, $t_{1/2} \approx 859.6$ ms), chlorine-34 (^{34}Cl, $t_{1/2} \approx 1.53$ s), carbon-10 (^{10}C, $t_{1/2} \approx 19$ s), fluorine-17 (^{17}F, $t_{1/2} \approx 64.49$ s) and oxygen-14 (^{14}O, $t_{1/2} \approx 70$ s).

This could be achieved by conducting an experimental investigation with different homogeneous phantoms and by obtaining the cross-sections in an iterative way, in a process similar to the one carried out in the Heidelberg Ion-Beam Therapy Center.

Ideally, this experimental investigation should also be conducted on the production of positron-emitting species already acquired in this work, due to the influence of the PET detection performance and of the irradiation scheme on the obtained cross-sectional data.

Finally, another important improvement would be the speed-up of the simulation run time. Despite the currently relatively short run times, once the experiments with the anthropomorphic phantom and with the therapeutic proton beam start, the simulation run times are expected to be considerably longer. The shortening of this parameter is crucial to allow the use of the developed prototype on a daily basis in the clinical context.

Reference List and Bibliography

[1] G. M. Copper and R. E. Hausman, *The Cell: a Molecular Approach*. Washington, D.C.: Sinauer Associates, Inc., 4^{th} ed., 2006.

[2] S. Wu, W. Zhu, P. Thompson, and Y. A. Hannun, "Evaluating intrinsic and non-intrinsic cancer risk factors," *Nature Communications*, vol. 9(1), pp. 3490–, 2018.

[3] H. Sung, J. Ferlay, R. L. Siegel, M. Laversanne, I. Soerjomataram, A. Jemal, and F. Bray, "Global Cancer Statistics 2020: GLOBOCAN Estimates of Incidence and Mortality Worldwide for 36 Cancers in 185 Countries," *CA: A Cancer Journal for Clinicians*, vol. 71(3), pp. 209–249, 2021.

[4] L. A. Emens and G. Middleton, "The interplay of immunotherapy and chemotherapy: harnessing potential synergies," *Cancer Immunology Research*, vol. 3(5), pp. 436–443, 2015.

[5] J. Jin, "Radiation Therapy," *JAMA*, vol. 310(24), p. 2691, 2013.

[6] E. Evans and J. Staffurth, "Principles of cancer treatment by radiotherapy," *Surgery (Oxford)*, vol. 36(3), pp. 111–116, 2018.

[7] E. Podgorsak, *Radiation oncology physics: a handbook for teachers and students*. Vienna, Austria: International Atomic Energy Agency, 2^{th} ed., 2005.

[8] J. R. Hubenak, Q. Zhang, C. D. Branch, and S. J. Kronowitz, "Mechanisms of injury to normal tissue after radiotherapy: a review," *Plastic and Reconstructive Surgery*, vol. 133(1), pp. 49e–56e, 2014.

[9] A. C. Begg, F. A. Stewart, and C. Vens, "Strategies to improve radiotherapy with targeted drugs," *Nature Reviews Cancer*, vol. 11(4), pp. 239–253, 2011.

[10] S. Gwynne and J. Staffurth, "Cancer treatment - principles of cancer treatment by radiotherapy," *Surgery (Oxford)*, vol. 30(4), pp. 191–193, 2012.

[11] D. E. Gerber and T. A. Chan, "Recent Advances in Radiation Therapy," *American Family Physician*, vol. 78(11), pp. 1254–1262, 2008.

[12] X. Zhu and G. El Fakhri, "Proton therapy verification with PET imaging," *Theranostics*, vol. 3(10), pp. 731–740, 2013.

[13] R. Mohan and D. Grosshans, "Proton therapy - Present and future," *Advanced Drug Delivery Reviews*, vol. 109, pp. 26–44, 2017.

[14] `https://www.ptcog.ch`. Accessed: 2022-07-18.

[15] T. I. Yock and N. J. Tarbell, "Technology insight: Proton beam radiotherapy for treatment in pediatric brain tumors," *Nature Clinical Practice Oncology*, vol. 1(2), pp. 97–103, 2004.

[16] D. Jette and W. Chen, "Creating a spread-out Bragg peak in proton beams," *Physics in Medicine and Biology*, vol. 56(11), pp. N131–8, 2011.

[17] H. Paganetti, "Range uncertainties in proton therapy and the role of Monte Carlo simulations," *Physics in Medicine and Biology*, vol. 57(11), pp. R99–117, 2012.

[18] H. Paganetti and G. El Fakhri, "Monitoring proton therapy with PET," *The British Journal of Radiology*, vol. 88(1051), pp. 88–90, 2015.

[19] P. Cambraia Lopes, J. Bauer, A. Salomon, I. Rinaldi, V. Tabacchini, T. Tessonnier, P. Crespo, K. Parodi, and D. R. Schaart, "First in situ TOF-PET study using digital photon counters for proton range verification," *Physics in Medicine and Biology*, vol. 61(16), pp. 6203–30, 2016.

[20] `https://geant4.web.cern.ch/node/1`. Accessed: 2021-10-19.

[21] `https://utaustinportugal.org/wp-content/uploads/2020/09/TOF-PET-.pdf`. Accessed: 2021-10-11.

[22] W. R. Leo, *Techniques for Nuclear and Particle Physics Experiments: A How to Approach*. Berlin: Springer-Verlag, 2^{nd} ed., 1994.

[23] W. D. Newhauser and R. Zhang, "The physics of proton therapy," *Physics in Medicine and Biology*, vol. 60(8), pp. R155–R209, 2015.

[24] C. Leroy and P. G. Rancoita, *Principles of Radiation Interaction in Matter and Detection*. Singapore: World Scientific Publishing Co. Pte. Ltd., 2^{nd} ed., 2009.

[25] G. F. Knoll, *Radiation Detection and Measurement*. New York: John-Wiley & Sons, Inc., 3^{rd} ed., 2000.

[26] A. C. Knopf and A. Lomax, "In vivo proton range verification: a review," *Physics in Medicine & Biology*, vol. 58(15), pp. R131–60, 2013.

[27] S. R. Cherry, J. A. Sorenson, and M. E. Phelps, *Physics in Nuclear Medicine*. Philadelphia: Elsevier Saunders, 4^{th} ed., 2012.

[28] J. T. Bushberg, J. A. Seibert, E. M. L. Jr, and J. M. Boone, *The Essential Physics of Medical Imaging*. Philadelphia: Lippincott Williams & Wilkins, 3^{rd} ed., 2012.

[29] M. A. Flower, *Webb's Physics of Medical Imaging*. Boca Raton, Florida: Taylor & Francis Group, 2^{nd} ed., 2012.

[30] G. B. Saha, *Fundamentals of Nuclear Pharmacy*. Cleveland: Springer, 5^{th} ed., 2004.

[31] X. Zhu, S. España, J. Daartz, N. Liebsch, J. Ouyang, H. Paganetti, T. R. Bortfeld, and G. E. Fakhri, "Monitoring proton radiation therapy with in-room PET imaging," *Physics in Medicine & Biology*, vol. 56(13), pp. 4041–4057, 2011.

[32] S. E. McGowan, N. G. Burnet, and A. J. Lomax, "Treatment planning optimisation in proton therapy," *British Journal of Radiology*, vol. 86(1021), pp. 1–12, 2013.

[33] G. Pausch, J. Berthold, W. Enghardt, K. Römer, A. Straessner, A. Wagner, T. Werner, and T. Kögler, "Detection systems for range monitoring in proton therapy: Needs and challenges," *Nuclear Instruments and Methods in Physics Research Section A: Accelerators, Spectrometers, Detectors and Associated Equipment*, vol. 954, pp. 1612–1627, 2020.

[34] S. Krishnamoorthy, B.-K. K. Teo, W. Zou, J. McDonough, J. S. Karp, and S. Surti, "A Proof-of-Concept Study of an In-Situ Partial-Ring Time-of-Flight PET Scanner for Proton Beam Verification," *IEEE Transactions on Radiation and Plasma Medical Sciences*, vol. 5(5), pp. 694 – 702, 2021.

[35] H. J. Choi, J. W. Jang, W.-G. Shin, H. Park, S. Incerti, and C. H. Min, "Development of integrated prompt gamma imaging and positron emission tomography system for in vivo 3-D dose verification: a Monte Carlo study," *Physics in Medicine & Biology*, vol. 65(10), pp. 1–15, 2020.

[36] K. Parodi and J. C. Polf, "In vivo range verification in particle therapy," *Medical Physics*, vol. 45(11), pp. e1036–e1050, 2018.

[37] A. Morozov, H. Simões, and P. Crespo, "Distal edge determination precision for a multi-slat prompt-gamma camera: A comprehensive simulation and optimization of the detection system," *Physica Medica*, vol. 84, pp. 85–100, 2021.

[38] K. Parodi, H. Paganetti, H. A. Shih, S. Michaud, J. S. Loeffler, T. F. DeLaney, N. J. Liebsch, J. E. Munzenrider, A. J. Fischman, A. Knopf, and T. Bortfeld, "Patient study of in vivo verification of beam delivery and range, using positron emission tomography and computed tomography imaging after proton therapy," *International Journal of Radiation Oncology - Biology - Physics*, vol. 68(3), pp. 920–934, 2007.

[39] A. Knopf, K. Parodi, T. Bortfeld, H. A. Shih, and H. Paganetti, "Systematic analysis of biological and physical limitations of proton beam range verification with offline PET/CT scans," *Physics in Medicine & Biology*, vol. 54(14), p. 4477–4495, 2009.

[40] J. J. Vaquero and P. Kinahan, "Positron Emission Tomography: Current Challenges and Opportunities for Technological Advances in Clinical and Preclinical Imaging Systems," *Annual Review of Biomedical Engineering*, vol. 17, pp. 385–414, 2015.

[41] A. C. Knopf, K. Parodi, H. Paganetti, and T. Bortfeld, "In Vivo Imaging - Proton beam range verification with PET/CT." `https://www.ptcog.ch/archive/conference_p&t&v/PTCOG47/presentations/5_Meeting_Friday/PTCOG47_Talk_A_KNOPF.pdf`, 2008. Accessed: 2021-11-08.

[42] D. Bailey, J. Humm, A. Todd-Pokropek, and A. van Aswegen, *Nuclear Medicine Physics: a handbook for teachers and students*. Vienna, Austria: International Atomic Energy Agency, 2014.

[43] D. R. Dance, S. Christofides, A. D. A. Maidment, I. D. Mclean, and K. H. Ng, *Diagnostic radiology physics: a handbook for teachers and students*. Vienna, Austria: International Atomic Energy Agency, 1^{st} ed., 2014.

[44] K. P. Schaäfers, "The promise of nuclear medicine technology: Status and future perspective of high-resolution whole-body PET," *Physica Medica*, vol. 24(2), pp. 57–62, 2008.

[45] H. Peng and C. S. Levin, "Study of PET intrinsic spatial resolution and contrast recovery improvement for PET/MRI systems," *Physics in Medicine & Biology*, vol. 57(9), p. N101–N115, 2012.

[46] T. K. Lewellen, "The Challenge of Detector Designs for PET," *Nuclear Medicine and Molecular Imaging*, vol. 195(2), pp. 301–309, 2010.

[47] T.A.Laplace, B.L.Goldblum, J.A.Brown, and J.J.Manfredi, "Scintillator light yield measurements with waveform digitizers," *Nuclear Instruments and Methods in Physics Research Section A: Accelerators, Spectrometers, Detectors and Associated Equipment*, vol. 959, p. 163485, 2020.

[48] J. L. Humm, A. Rosenfeld, and A. D. Guerra, "From PET detectors to PET scanners," *European Journal of Nuclear Medicine and Molecular Imaging*, vol. 30(11), pp. 1574–1597, 2003.

[49] P. Mengucci, G. André, E. Auffray, G. Barucca, C. Cecchi, R. Chipaux, A. Cousson, F. Davì, N. Di Vara, D. Rinaldi, and E. Santecchia, "Structural, mechanical and light yield characterisation of heat treated LYSO:Ce single crystals for medical imaging applications," *Nuclear Instruments and Methods in Physics Research Section A Accelerators Spectrometers Detectors and Associated Equipment*, vol. 785, pp. 110–116, 2015.

[50] H. Alva-Sánchez, A. Zepeda-Barrios, V. D. Díaz-Martínez, T. Murrieta-Rodríguez, A. Martínez-Dávalos, and M. Rodríguez-Villafuerte, "Understanding the intrinsic radioactivity energy spectrum from 176Lu in LYSO/LSO scintillation crystals," *Scientific Reports*, vol. 8(1), p. 17310–, 2018.

[51] F. E. E.-M. y Terán, A. S. Ortega-Galindo, T. Murrieta-Rodríguez, M. Rodríguez-Villafuerte, A. Martínez-Dávalos, and H. Alva-Sánchez, "Coincidence energy spectra due to the intrinsic radioactivity of LYSO scintillation crystals," *EJNMMI Physics*, vol. 7(1):21, 2020.

[52] S. Gundacker and A. Heering, "The silicon photomultiplier: fundamentals and applications of a modern solid-state photon detector," *Physics in Medicine & Biology*, vol. 65(17), p. 17TR01, 2020.

[53] S. España, G. Tapias, L. M. Fraile, J. L. Herraiz, E. Vicente, J. Udias, M. Desco, and J. J. Vaquero, "Performance Evaluation of SiPM Detectors for PET Imaging in the Presence of Magnetic Fields," in *IEEE Nuclear Science Symposium and Medical Imaging conference*, (Dresden, Germany), p. 3591–3595, IEEE, October 2008.

[54] S. Vandenberghe, E. Mikhaylova, E. D'Hoe, P. Mollet, and J. S. Karp, "Recent developments in time-of-flight PET," *EJNMMI Physics*, vol. 3(1), p. 3, 2016.

[55] W. W. Moses, "Recent Advances and Future Advances in Time-of-Flight PET," *Nuclear Instruments and Methods in Physics Research Section A: Accelerators, Spectrometers, Detectors and Associated Equipment*, vol. 580(2), pp. 919–924, 2007.

[56] J. W. Cates and C. S. Levin, "Advances in coincidence time resolution for PET," *Physics in Medicine & Biology*, vol. 61(6), pp. 2255–2264, 2016.

[57] P. Crespo, G. Shakirin, F. Fiedler, W. Enghardt, and A. Wagner, "Direct time-of-flight for quantitative, real-time in-beam PET: a concept and feasibility study," *Physics in Medicine & Biology*, vol. 52(23), pp. 6795–6811, 2007.

[58] M. S. Brown, S. Gundacker, A. Taylor, C. Tummeltshammer, E. Auffray, P. Lecoq, I. Papakonstantinou, and B. Merk, "Influence of Depth of Interaction upon the Performance of Scintillator Detectors," *PLoS ONE*, vol. 9(5), pp. e98177–, 2014.

[59] W. Enghardt, P. Crespo, F. Fiedler, R. Hinz, K. Parodi, J. Pawelke, and F. Pönisch, "Charged hadron tumour therapy monitoring by means of PET," *Nuclear Instruments and Methods in Physics Research Section A: Accelerators, Spectrometers, Detectors and Associated Equipment*, vol. 525, pp. 284–288, 2004.

[60] T. Hofmann, A. Fochi, K. Parodi, and M. Pinto, "Prediction of positron emitter distributions for range monitoring in carbon ion therapy: an analytical approach," *Physics in Medicine & Biology*, vol. 64(10), pp. 105022–, 2019.

[61] K. Parodi, F. Ponisch, and W. Enghardt, "Experimental study on the feasibility of in-beam PET for accurate monitoring of proton therapy," *IEEE Transactions on Nuclear Science*, vol. 52(3), p. 778–786, 2005.

[62] S. España, X. Zhu, J. Daartz, G. E. Fakhri, T. Bortfeld, and H. Paganetti, "Reliability of proton-nuclear interaction cross section data to predict proton-induced PET images in proton therapy," *Physics in Medicine & Biology*, vol. 56(9), p. 2687–2698, 2011.

[63] A. F. Bielajew, *Fundamentals of the Monte Carlo method for neutral and charged particle transport*. Ann Arbor, Michigan: The University of Michigan, 2001.

[64] P. L. Bonate, "A brief introduction to Monte Carlo simulation," *Clinical Pharmacokinetics*, vol. 40(1), pp. 15–22, 2001.

[65] J. F. Carrier, L. Archambault, L. Beaulieu, and R. Roy, "Validation of GEANT4, an object-oriented Monte Carlo toolkit, for simulations in medical physics," *Medical Physics*, vol. 31(3), pp. 484–492, 2004.

[66] D. W. O. Rogers, "Fifty years of Monte Carlo simulations for medical physics," *Physics in Medicine & Biology*, vol. 51(13), p. R287–R301, 2006.

[67] J. Allison, K. Amako, J. Apostolakis, H. Araujo, P. Arce Dubois, M. Asai, G. Barrand, R. Capra, S. Chauvie, R. Chytracek, G. Cirrone, G. Cooperman, G. Cosmo, G. Cuttone, G. Daquino, M. Donszelmann, M. Dressel, G. Folger, F. Foppiano, J. Generowicz, V. Grichine, S. Guatelli, P. Gumplinger, A. Heikkinen, I. Hrivnacova, A. Howard, S. Incerti, V. Ivanchenko, T. Johnson, F. Jones, T. Koi, R. Kokoulin, M. Kossov, H. Kurashige, V. Lara, S. Larsson, F. Lei, O. Link, F. Longo, M. Maire, A. Mantero, B. Mascialino, I. McLaren, P. Mendez Lorenzo, K. Minamimoto, K. Murakami, P. Nieminen, L. Pandola, S. Parlati, L. Peralta, J. Perl, A. Pfeiffer, M. Pia, A. Ribon, P. Rodrigues, G. Russo, S. Sadilov, G. Santin, T. Sasaki, D. Smith, N. Starkov, S. Tanaka, E. Tcherniaev, B. Tome, A. Trindade, P. Truscott, L. Urban, M. Verderi, A. Walkden, J. Wellisch, D. Williams, D. Wright, and H. Yoshida, "Geant4 developments and applications," *IEEE Transactions on Nuclear Science*, vol. 53(1), pp. 270–278, 2006.

[68] S. Agostinelli, J. Allison, K. Amako, J. Apostolakis, H. Araujo, P. Arce, M. Asai, D. Axen, S. Banerjee, G. Barrand, F. Behner, L. Bellagamba, J. Boudreau, L. Broglia, A. Brunengo, H. Burkhardt, S. Chauvie, J. Chuma, R. Chytracek, G. Cooperman, G. Cosmo, P. Degtyarenko, A. Dell'Acqua, G. Depaola, D. Dietrich, R. Enami, A. Feliciello, C. Ferguson, H. Fesefeldt, G. Folger, F. Foppiano, A. Forti, S. Garelli, S. Giani, R. Giannitrapani, D. Gibin, J. J. Gómez Cadenas, I. González, G. Gracia Abril, G. Greeniaus, W. Greiner, V. Grichine, A. Grossheim, S. Guatelli, P. Gumplinger, R. Hamatsu, K. Hashimoto, H. Hasui, A. Heikkinen, A. Howard, V. Ivanchenko, A. Johnson, F. W. Jones, J. Kallenbach, N. Kanaya, M. Kawabata, Y. Kawabata, M. Kawaguti, S. Kelner, P. Kent, A. Kimura, T. Kodama, R. Kokoulin, M. Kossov, H. Kurashige, E. Lamanna, T. Lampén, V. Lara, V. Lefebure, F. Lei, M. Liendl, W. Lockman, F. Longo, S. Magni, M. Maire, E. Medernach, K. Minamimoto, P. Mora de Freitas, Y. Morita, K. Murakami, M. Nagamatu, R. Nartallo, P. Nieminen, T. Nishimura, K. Ohtsubo, M. Okamura, S. O'Neale, Y. Oohata, K. Paech, J. Perl, A. Pfeiffer, M. G. Pia, F. Ranjard, A. Rybin, S. Sadilov, E. Di Salvo, G. Santin, T. Sasaki, N. Savvas, Y. Sawada, S. Scherer,

S. Sei, V. Sirotenko, D. Smith, N. Starkov, H. Stoecker, J. Sulkimo, M. Takahata, S. Tanaka, E. Tcherniaev, E. Safai Tehrani, M. Tropeano, P. Truscott, H. Uno, L. Urban, P. Urban, M. Verderi, A. Walkden, W. Wander, H. Weber, J. P. Wellisch, T. Wenaus, D. C. Williams, D. Wright, T. Yamada, H. Yoshida, and D. Zschiesche, "Geant4 — A simulation toolkit," *Nuclear Instruments and Methods in Physics Research Section A: Accelerators, Spectrometers, Detectors and Associated Equipment*, vol. 506(3), pp. 250–303, 2003.

[69] L. Archambault, L. Beaulieu, J. Carrier, F. Castrovillari, S. Chauvie, F. Foppiano, G. Ghiso, S. Guatelli, S. Incerti, E. Lamanna, S. Larsson, M. Lopes, L. Peralta, M. Pia, P. Rodrigues, V. Tremblay, and A. Trindade, "Overview of geant4 applications in medical physics," in *2003 IEEE Nuclear Science Symposium. Conference Record (IEEE Cat. No.03CH37515)*, vol. 3, pp. 1743–1745, 2003.

[70] "Introduction to Geant4." `https://cds.cern.ch/record/491492/files/p107.pdf`. Accessed: 2022-08-15.

[71] "Detector Simulation - Sensitive Detectors and Hits User Actions." `https://indico.cern.ch/event/294651/sessions/55918/attachments/552022/760640/UserActions.pdf`. Accessed: 2022-08-28.

[72] "Physics in Geant4: Particles, processes and cuts." `https://agenda.infn.it/event/11278/sessions/1288/attachments/5725/6381/particles-processes-cuts.pdf`. Accessed: 2022-08-16.

[73] "Physics-II: Particles and Processes in Geant4." `https://indico.cern.ch/event/789510/contributions/3279415/attachments/1817621/2971421/ParticleProcesses.pdf`. Accessed: 2022-08-16.

[74] "Introductory course on Geant4: Primary generator." `https://indico.lip.pt/event/681/contributions/2094/attachments/1901/2533/PrimaryGenerator_Geant4_Braga2020.pdf`. Accessed: 2022-08-16.

[75] "Detector Simulation - Primary particles." `https://indico.cern.ch/event/472305/contributions/1982326/attachments/1224119/1791098/3a_PrimaryParticles.pdf`. Accessed: 2022-08-16.

[76] "Optional Classes - 1^{st} LIP Introductory Course on GEANT4." `https://indico.lip.pt/event/681/contributions/2098/attachments/1903/2532/OptionalClasses.pdf`. Accessed: 2022-09-14.

[77] B. L. Cox, S. A. Graves, M. Farhoud, T. E. Barnhart, J. J. Jeffery, K. W. Eliceiri, and R. J. Nickles, "Development of a novel linearly-filled Derenzo microPET phantom," *American Journal of Nuclear Medicine and Molecular Imaging*, vol. 6(3), p. 199–204, 2016.

[78] "Book For Application Developers, Release 10.3 - Geant4 Collaboration." https://indico.cern.ch/event/647154/contributions/2714212/attachments/1529029/2397032/BookForApplicationDevelopers.pdf. Accessed: 2022-08-16.

[79] "Geant4 Geometry." http://geant4.in2p3.fr/IMG/pdf_Lecture-Geometry.pdf. Accessed: 2022-08-28.

[80] "ABS Material." https://www.rankred.com/what-is-abs-material-properties/. Accessed: 2022-09-01.

[81] "Geant4 Materials Database." https://geant4-userdoc.web.cern.ch/UsersGuides/ForApplicationDeveloper/html/Appendix/materialNames.html. Accessed: 2022-08-31.

[82] "Datasheet MPPC (Multi-Pixel Photon Counter) S14160/S14161 series." https://www.hamamatsu.com/resources/pdf/ssd/s14160_s14161_series_kapd1064e.pdf. Accessed: 2022-01-04.

[83] https://absolutepcbassembly.com/pwb-vs-pcb/. Accessed: 2022-08-08.

[84] G. Barbarino, R. Asmundis, G. De Rosa, C. Mollo, S. Russo, and D. Vivolo, "High gain hybrid photomultipliers based on solid state p-n junctions in geiger mode and their use in astroparticle physics," *Physics Procedia*, vol. 37, pp. 703–708, 2012.

[85] J. Guo, J. Guo, and Z. Xu, "Recycling of non-metallic fractions from waste printed circuit boards: A review," *Journal of Hazardous Materials*, vol. 168, p. 567–590, 2009.

[86] W. He, G. Li, X. Ma, H. Wang, J. Huang, M. Xu, and C. Huang, "Weee recovery strategies and the weee treatment status in china," *Journal of Hazardous Materials*, vol. 136(3), p. 502–512, 2006.

[87] H. Duan, K. Hou, J. Li, and X. Zhu, "Examining the technology acceptance for dismantling of waste printed circuit boards in light of recycling and environmental concerns," *Journal of Hazardous Materials*, vol. 92(3), p. 392–399, 2011.

[88] H. Cui and C. Anderson, "Hydrometallurgical treatment of waste printed circuit boards: Bromine leaching," *Metals*, vol. 10(4), p. 462–480, 2020.

[89] https://cometmetals.com/copper/alloy-110-copper/. Accessed: 2022-01-04.

[90] "Tracking." https://idpasc.lip.pt/uploads/talk/file/398/Tracking.pdf. Accessed: 2022-09-06.

[91] "Range Cuts." https://geant4-userdoc.web.cern.ch/UsersGuides/ForApplicationDeveloper/html/GettingStarted/particleDef.html#howtospecparti-rangecuts. Accessed: 2022-09-14.

[92] "Physics in Geant4: Particles, processes, cuts and models." https://agenda.infn.it/event/11278/sessions/1288/attachments/5725/6381/particles-processes-cuts.pdf. Accessed: 2022-09-06.

[93] "X-Ray Transition Energies Database." https://physics.nist.gov/cgi-bin/XrayTrans/search.pl?element=Lu&trans=All&lower=&upper=&units=eV. Accessed: 2022-09-18.

[94] E. Seravalli, C. Robert, J. Bauer, F. Stichelbaut, C. Kurz, J. Smeets, C. Van Ngoc Ty, D. R. Schaart, I. Buvat, K. Parodi, and F. Verhaegen, "Monte Carlo calculations of positron emitter yields in proton radiotherapy," *Physics in Medicine & Biology*, vol. 57(6), p. 1659–1673, 2012.

[95] J. Bauer, D. Unholtz, C. Kurz, and K. Parodi, "An experimental approach to improve the monte carlo modelling of offline PET/CT-imaging of positron emitters induced by scanned proton beams," *Physics in Medicine & Biology*, vol. 58(15), pp. 5193–5213, 2013.

[96] K. Parodi, H. Paganetti, E. Cascio, J. B. Flanz, A. A. Bonab, N. M. Alpert, K. Lohmann, and T. Bortfeld, "PET/CT imaging for treatment verification after proton therapy: A study with plastic phantoms and metallic implants," *Medical Physics*, vol. 34(2), pp. 419–435, 2007.

[97] J. Sisterson, A. Koehler, and R. Eilbert, "^{40}Ca(p, 2pn)^{38}K total nuclear cross section," *Physical Review*, vol. 18(1), p. 582–583, 1978.

[98] I. A, S. V, S. M, S. N, and U. L, *Production of Radionuclides at Intermediate Energies*. Berlin: Springer, v.13 ed., 1991.

[99] "EXFOR's ^{31}P(p,x)^{30}P cross-section data set." https://www-nds.iaea.org/exfor/servlet/X4sGetSubent?reqx=509&subID=100181004&plus=2. Accessed: 2022-08-24.

Appendix

A

Geant4 Solids

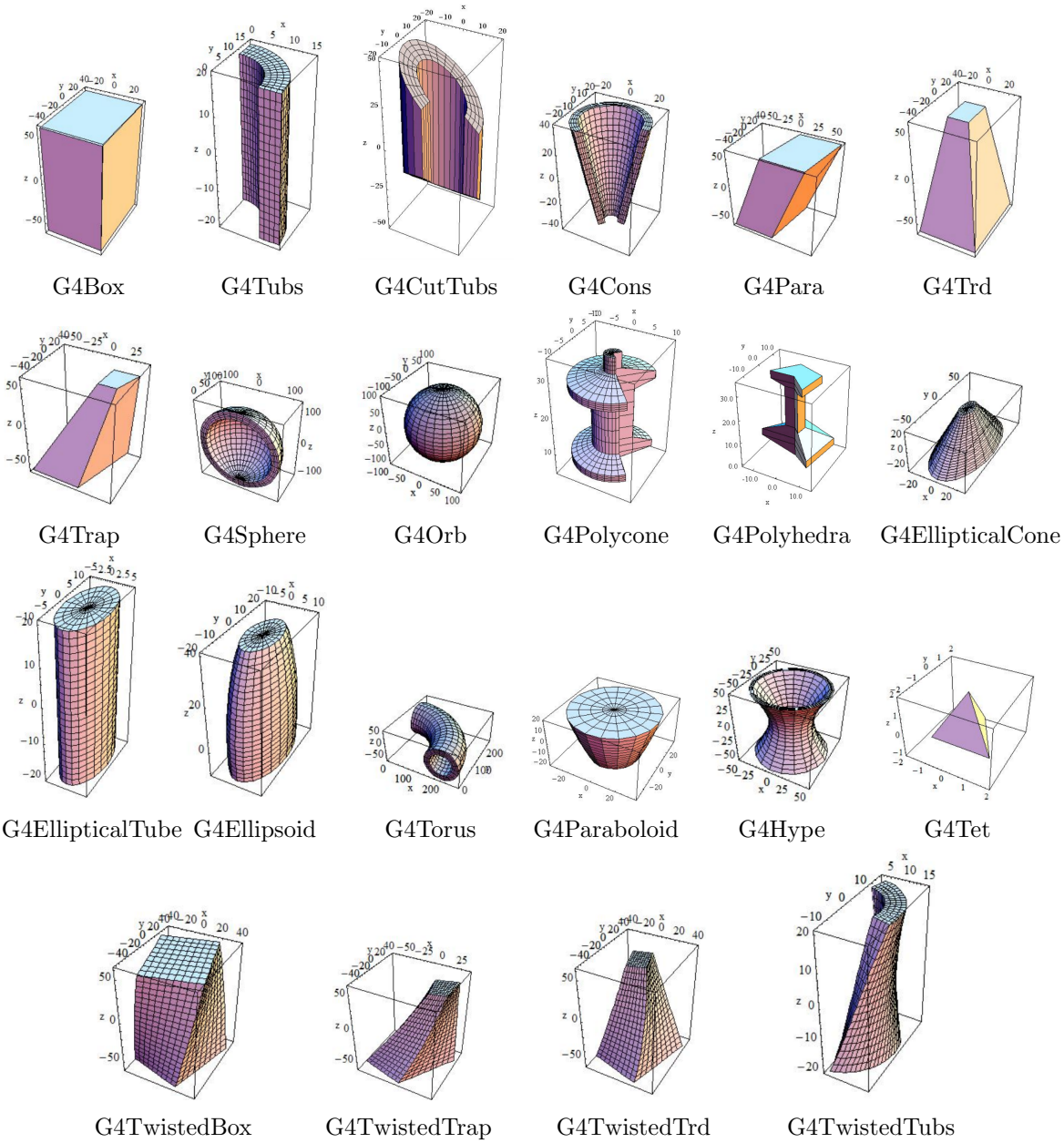

Figure A.1: Main Geant4 solids. Adapted from [78].